

**ION COLLIMATION AND IN-CHANNEL POTENTIAL SHAPING
USING IN-CHANNEL ELECTRODES FOR HALL EFFECT
THRUSTERS**

A Dissertation
Presented to
The Academic Faculty

By

Kunning Gabriel Xu

In Partial Fulfillment
Of the Requirements for the Degree
Doctor of Philosophy in
School of Aerospace Engineering

Georgia Institute of Technology

August, 2012

Copyright © 2012 by Kunning G. Xu

**ION COLLIMATION AND IN-CHANNEL POTENTIAL SHAPING
USING IN-CHANNEL ELECTRODES FOR HALL EFFECT
THRUSTERS**

Approved by:

Dr. Mitchell Walker, Advisor
Associate Professor
School of Aerospace Engineering
Georgia Institute of Technology

Dr. Jerry Seitzman
Professor
School of Aerospace Engineering
Georgia Institute of Technology

Dr. Jeff Jagoda
Professor
School of Aerospace Engineering
Georgia Institute of Technology

Dr. Peter Peterson
Aerojet Corporation

Dr. Suresh Menon
Professor
School of Aerospace Engineering
Georgia Institute of Technology

Date Approved: June 25, 2012

Dedicated to my parents

“The nitrogen in our DNA, the calcium in our teeth, the iron in our blood, the carbon in our apple pies were made in the interiors of collapsing stars. We are made of star stuff.”

“Somewhere, something incredible is waiting to be known.”

Carl Sagan

ACKNOWLEDGEMENTS

I would like to thank the many people who have been a part of my life these last six year and have in their own ways helped me get to here. I would like to first thank Dr. Mitchell Walker for his support and guidance in my research. I would like to thank Dr. Jeff Jagoda for letting me just walk in his door and giving me advice, free of charge, over the many years. I would also like to thank the AMPAC Corporation for funding this work and my education.

I would like to thank the financial staff of the aerospace department for helping me with the many hurdles of purchasing, travel, and money. I would like to extend a thank you to the AE machine shop. They persevered through the muck of machining BN and graphite to allow me to conduct my experiments.

I would like to acknowledge and thank the graduate students, undergraduate students, and other staff at HPEPL for their help, friendship, and support. Logan, it has been a good ride, thank you for being a friend and sounding board, I will see you on the other side, so says Der Kommissar. Natalie, I have enjoyed our repartee.

I would like to express my heartfelt thanks and appreciation for my fiancée. You have put up with my odd work hours on evening and weekends for months at a time. Thank you for your understanding and love.

Finally, I would like to thank my parents, whose support has carried me throughout my life. Without your guidance, I would not be the person I am today.

TABLE OF CONTENTS

ACKNOWLEDGEMENTS.....	iv
LIST OF FIGURES	viii
NOMENCLATURE	xiv
SUMMARY	xvii
CHAPTER 1 INTRODUCTION.....	1
1.1 Electric Propulsion Overview.....	1
1.2 Hall Effect Thruster Overview.....	5
1.3 Problem Statement.....	11
1.4 High Thrust-to-Power Operation.....	12
1.5 Research Contribution	16
1.6 Organization.....	17
CHAPTER 2 BACKGROUND	19
2.1 In-Channel Electrodes.....	19
2.2 Secondary Electron Emission.....	23
2.3 Cusp Magnetic Fields	25
2.4 Internal Plasma Potential Structure.....	27
CHAPTER 3 FACILITIES AND DIAGNOSTICS.....	31
3.1 Vacuum Chambers.....	31
3.2 T-220HT Hall Effect Thruster	34
3.3 Diagnostics.....	35
3.3.1 Motion Systems	35
3.3.2 Thrust Stand.....	36
3.3.3 Faraday Probe	36
3.3.2.1 Theory of Operation.....	36
3.3.2.2 Error	39
3.3.2.3 Setup and Design	47
3.3.4 Retarding Potential Analyzer.....	48
3.3.4.1 Theory of Operation.....	49
3.3.4.2 Error	51
3.3.4.3 Setup and Design	52

3.3.5	HARP	53
3.3.6	Floating Emissive Probe	56
3.3.6.1	Theory of Operation.....	56
3.3.6.2	Error	59
3.3.6.3	Setup and Design	60
3.4	Summary	62
CHAPTER 4 INITIAL DESIGN: STAINLESS STEEL SURFACE ELECTRODES ...		63
4.1	Magnetic Field Design.....	63
4.1.1	Magnetic Field Design Characteristics	64
4.1.2	Final Magnetic Field Design.....	67
4.2	Electrodes.....	69
4.2.1	Electrode Placement.....	71
4.3	Thermalized Plasma Potential.....	73
4.4	Ionization and Recombination	74
4.4.1	Ionization	74
4.4.2	Electron-Ion Recombination.....	80
4.4.3	Wall Losses.....	81
4.5	Experimental Results	87
4.5.1	Steel Electrode Performance.....	89
4.6	Results and Discussion	93
4.7	Summary.....	97
CHAPTER 5 FINAL DESIGN: EMBEDDED ELECTRODE ON KRYPTON.....		99
5.1	Electrode Redesign	99
5.2	Material Changes: Graphite versus BN	102
5.2.1	Performance	102
5.2.2	Faraday Probe	105
5.2.3	RPA.....	109
5.2.4	Internal Plasma Potential	111
5.3	EEHET on Krypton.....	113
5.3.1	Performance	114
5.3.2	Faraday Probe	117
5.4	Summary.....	125
CHAPTER 6 EEHET ON XENON.....		127
6.1	Low Current Xenon Operation	127
6.1.1	Performance	127
6.1.2	Faraday Probe	131
6.1.3	RPA.....	138
6.1.4	Far-Field Plasma Potential.....	142
6.1.5	Internal Plasma Potential	143
6.2	High Current Operation	146
6.2.1	Performance	146
6.2.2	Faraday Probe	149
6.2.3	RPA.....	152

6.2.4	Far-Field Plasma Potential	155
6.3	Summary	156
CHAPTER 7 DISCUSSION OF ELECTRODE EFFECTS.....		158
7.1	Increased Ionization	158
7.2	Thruster Acceleration Region	163
7.3	Electron Temperature.....	166
7.4	Behavioral Differences with Electrodes	167
7.5	Near-Wall Sheath Behavior	169
7.6	Performance Improvements	172
7.7	High Current Discussion.....	174
7.8	Summary	174
CHAPTER 8 CONCLUDING REMARKS.....		176
8.1	Electrode Behavior and Effects	176
8.2	Increase in Thrust-to-Power Ratio	177
8.3	Future Work	178
8.3.1	Magnetic Field Considerations	178
8.3.2	Electrode Placement.....	179
8.3.3	Plasma Sheath	179
APPENDIX.....		181
BIBLIOGRAPHY.....		185

LIST OF FIGURES

Figure 1. Payload fraction as a function of specific impulse for the SSME and NSTAR ion engine. The EP system is capable of higher payload fractions and longer missions.....	4
Figure 2. Electron gyrating around a magnetic field line. Magnetic fields bend charge particle motion into a tight spin, the radius of which depends on particle mass, velocity, and magnetic field. Electrons being much lighter than ions are easily trapped.....	6
Figure 3. Hall effect motion of a charged particle. Electric field aligned vertically and magnetic field out of the plane of the page. Similar to spin about a magnetic field, the Hall effect motion is affected by the particle mass, thus electrons are greatly affected while ions are not.	7
Figure 4. 2-D Hall effect thruster schematic. The thruster has an annular construction and is ideally axisymmetric.	9
Figure 5. Thrust-to-power for various HETs compiled by Hofer.[20] T/P ratio increases as discharge voltage decreases until insufficient ion density causes T/P ratio to drop.	16
Figure 6. NASA-457M Hall thruster. The annular anode covers the rear plane and extends along the channel walls. Propellant injection occurs at holes along the inner and outer walls of the annular anode.[30].....	22
Figure 7. Magnetic field topography of the NASA-173Mv1. The field follows standard magnetic field design principles and generates predominantly radial fields in the channel. Similar fields are used for the NASA-173Mv2 and the 457M.[20].....	22
Figure 8. SEE curve fits for boron nitride and stainless steel from data in Table 1 for a range of electron temperatures. HETs typically operate in the 20 eV+ range.....	24
Figure 9. Ion engine cusp field schematic from [33]. The magnetic field lines indicate vector directions, while the contours show the magnitude of the field.	25
Figure 10. Cylindrical HET schematic from PPPL [41] (left) and MIT [43] (right). Both thruster utilize cusp-shaped magnetic fields along the walls due to the lack of a center magnetic pole.	26
Figure 11. Example of the plasma potential profile along the discharge channel centerline. A significant portion of the potential drop and acceleration occurs outside the thruster.	28
Figure 12. Axial electric and radial magnetic field profiles for HETs. The two fields peak near the same location.....	29
Figure 13. VTF-1 Schematic.....	32
Figure 14. VTF-1 picture showing the blue diffusions pumps below.	32
Figure 15. VTF-2 schematic.	33
Figure 16. VTF-2 picture.	34
Figure 17. Example Faraday probe measurements of ion current density for varying background pressures.[58].....	38

Figure 18. Measurement geometry for the Faraday probe. The angles and distances are shown for the correction for the two point sources. Figure is borrowed from Brown and Gallimore.[62].....	42
Figure 19. The backpressure variation of ion current density shows a linear trend. Extrapolation to zero pressure (space conditions) allows better approximation of true current density. Measurements are take 1 meter from thruster exit plane in the plume.....	45
Figure 20. The measured chamber current profiles at 0 sccm are very similar to the computed densities for space conditions.....	46
Figure 21. Beam current for the chamber and space conditions. The chamber condition exhibits slightly higher total beam current, largely due to CEX collisions creating extra ions from chamber neutrals.....	46
Figure 22. The plume divergence half angle for space and chamber conditions. The two have very similar plume angles, with slight differences at high voltage.....	46
Figure 23. HPEPL Faraday probe diagram and picture.....	48
Figure 24. Faraday probe electric schematic.....	48
Figure 25. Example RPA ion energy measurement. The most probably energy is taken as the energy of the ion beam, and the HWHM characterizes the uncertainty.....	51
Figure 26. HPEPL four grid RPA diagram and picture.....	53
Figure 27. RPA electric schematic.....	53
Figure 28. Example HARP position and measured probe potential. The potential is nearly flat for the short time it is at the target location, and has a very steep rise and fall when the probe enters and leaves the discharge channel.....	55
Figure 29. Example HARP probe position and discharge current oscillations. The insertion of the probe causes small increase in discharge oscillation as measured at the discharge power supply line.....	55
Figure 30. The HARP (right) and the modified T-220HT HET (left) in VTF-2 prior to testing. The miniature emissive probe is mounted on the HARP arm.....	56
Figure 31. Ideal emissive probe thermionic emission curve. The measured potential plateaus once sufficient electron emission is reached. At this point the probe is at the plasma potential.....	58
Figure 32. Miniature emissive probe schematic.....	61
Figure 33. Miniature emissive probe.....	61
Figure 34. The redesigned magnetic field for this dissertation. The field meets the historical metrics of good B field design, and incorporates cusp-shaped fields covering the electrodes.....	69
Figure 35. Centerline radial magnetic field for original T-220HT and redesigned field from simulations. The redesigned centerline radial strength matches closely to the original field, thus the electron motion should be similar.....	69
Figure 36. The stainless steel outer (left), and inner electrodes (right). The electrodes are made from strips of steel and curved to the proper diameter. Steel threaded rods are welded for electrical connections.....	70
Figure 37. T-220HT with stainless steel electrodes. Grooves are made in the channel material for the threaded rods to allow the electrodes to side as close to the surface as possible.....	71

Figure 38. Electrical schematic for the thruster showing connection to anode power line. The electrodes are connected to be based on the anode voltage.	71
Figure 39. Simulation of channel centerline electric potential for the full sized electrode (0.4 in) and two half sized electrodes (0.2 in) at the top and bottom of the same area.	73
Figure 40. Xenon ionization rate constant from Goebel[33] for 5 - 100 eV. There is little ionization below the xenon first ionization energy of 12 eV.....	75
Figure 41. The calculated electron density as a function of the discharge voltage for a constant 50 A current, and beam efficiency of 1. The maximum change in density is 3.16 times from low to high voltage.	78
Figure 42. Electron density for the range of beam efficiencies at constant 300 V and 50 A discharge. There is a maximum of 3.16 times increase in electron density from perfect to low beam efficiency.....	78
Figure 43. T-220HT with stainless steel electrodes running on krypton.	89
Figure 44. Stainless steel electrode performance at 9 A on krypton with 0-30 V electrodes. Electrodes cause increase in thrust, but decrease in T/P ratio.	90
Figure 45. Stainless steel electrode performance at 9 A on krypton with 0-30 V electrodes. Electrodes cause increase in I_{sp} and efficiency.	91
Figure 46. Stainless steel electrode performance at 20 A on krypton with 0 V and 10 V electrodes. The performance improvements are higher at 20 A than 9 A.	92
Figure 47. Electrode current at 9 A on krypton for thick electrodes with 0-30 V electrodes. The decreasing electrode current with increasing discharge voltage suggests anode absorbing increasing electron current.	97
Figure 48. T-220HT with embedded electrodes.	100
Figure 49. Embedded electrodes position in the discharge channel of the T-220HT. The steel clips around the edges were initially used to hold the rings in place.	101
Figure 50. EEHET post test. The white block on the right of the thruster (left side of picture) is a protective cover for the outer electrode wires.....	101
Figure 51. Thrust for BN and Floating electrode conditions on krypton at 9 A. The two cases have nearly identical thrust.....	103
Figure 52. T/P ratio for BN and Floating electrode conditions on krypton at 9 A. The BN case exhibits slightly higher T/P ratio at a few locations due to differences in mass flow. The differences can be attributed to uncertainty in the measurements and changing environment conditions between tests.....	103
Figure 53. Specific impulse for BN and Floating electrode conditions on krypton at 9 A.	104
Figure 54. Anode efficiency for BN and Floating electrode conditions on krypton at 9 A.	104
Figure 55. Plume probe setup.	105
Figure 56. One meter thrust plume sweep for Faraday probe and RPA.	106
Figure 57. Ion current density for BN and Floating cases at 150 – 300 V_d and 9 A. Except at low voltages, the two cases have very similar ion density profiles.	107
Figure 58. Integrated ion beam current for BN and Floating electrode at 9 A on krypton.	108
Figure 59. Plume divergence half angle for BN and Floating electrode cases on krypton.	108

Figure 60. RPA ion energy distribution functions for BN and Floating electrode on channel centerline. There is very little difference in the energy of the ions with the presence of graphite.	109
Figure 61. Most probable ion energy for BN and Floating electrode at 9 A on xenon. The BN case has slightly increased energy, but well within the uncertainty.	110
Figure 62. Propellant efficiency for BN and Floating electrode at 9 A on xenon. The Floating case has lower propellant efficiency even though the beam current was higher.	111
Figure 63. Total mass flow rate for BN and Floating electrode at 9 A on xenon. The Floating case required more propellant flow in order to maintain the same current, thus a lower propellant efficiency.	111
Figure 64. Mapped area of the discharge channel. Radial points are 4, 8, 10, 12, 13, and 13.5 mm on either side of centerline.	112
Figure 65. In-channel plasma potential contours for krypton at 150 V and 9 A for the BN (left) and Floating (right) cases. The two cases have nearly identical potential contours, with the Floating cases having slightly higher at any given location.	113
Figure 66. Electrode current for krypton at 9 A discharge current at 10 and 30 V _e . The 30 V _e case saw a large jump in the electrode current, pulling almost all discharge current from the anode.	114
Figure 67. Thrust for EEHET on krypton at 9 A. Also shown in green is data from the stainless steel electrodes.	116
Figure 68. <i>T/P</i> ratio for EEHET at 9 A.	116
Figure 69. Specific impulse on krypton at 9 A.	117
Figure 70. Efficiency on krypton at 9 A.	117
Figure 71. Ion current density profile for Floating electrodes on krypton at 9 A.	118
Figure 72. Ion current density profile for 150 V _d on krypton.	120
Figure 73. Ion current density profile for 200 V _d on krypton.	120
Figure 74. Ion current density profile for 250 V _d on krypton.	121
Figure 75. Ion current density profile for 300 V _d on krypton.	121
Figure 76. Ion beam current for total 9 A discharge current on krypton.	122
Figure 77. EEHET total mass flow rate for test cases on krypton.	123
Figure 78. Propellant efficiency, defined as ion beam current/total flow rate, for the three electrode cases on krypton. The electrodes increase the propellant efficiency for most discharge voltages.	124
Figure 79. Plume divergence half angle at 9 A discharge current. The electrodes do cause a small decrease in plume angle, especially at low voltages.	125
Figure 80. EEHET thrust on xenon at 9 A for the three electrode conditions. Both electrode conditions improve the thrust.	128
Figure 81. EEHET <i>T/P</i> ratio on xenon at 9 A for the three electrode conditions. The <i>T/P</i> only increases at 10 V _e . The decrease at the higher electrode potential is due to the high current collection offsetting the thrust gains.	129
Figure 82. EEHET specific impulse on xenon at 9 A for the three electrode conditions.	129
Figure 83. EEHET anode efficiency on xenon at 9 A for the three electrode conditions. Similar to <i>T/P</i> , efficiency incorporates total power, thus the high electrode current at 30 V _e causes a drop in efficiency.	130

Figure 84. Electrode current at 9 A for 10 V _e and 30 V _e electrode bias. Similar to the krypton tests, the electrodes draw in almost all of the current at 30 V _e	131
Figure 85. Faraday data for 9 A xenon with floating electrodes.	132
Figure 86. Ion current density profile for discharge voltages of 150, 200, 250, and 300 V for electrode bias configurations floating, 10 V _e , and 30 V _e	133
Figure 87. Close up ion current density profiles, from 60 to 100 degrees of chamber centerline.....	134
Figure 88. Current fraction (ion current density normalized by the Floating current density) showing Floating normalized (black), 10 V _e /Floating (blue) and 30 V _e /Floating (red).	135
Figure 89. Plume divergence half angle. The error bars are large, but are from systematic errors, thus the results still indicate a net decrease in the plume angle at low voltages.	137
Figure 90. Ion beam current from Faraday measurements shown increased ion beam with biased electrodes.	137
Figure 91. Ion energy distribution function on thruster centerline for floating electrodes at 9 ± 0.1 A.	138
Figure 93. Most probable ion energy for Floating, 10 V _e , and 30 V _e at 9 A. The small change in ion energy at 10 V _e and large change at 30 V _e is present at all voltages tested.	140
Figure 92. Ion energy distribution function at 175 V discharge at various angular positions.	140
Figure 94. Most probable ion energy for the ion energy distribution function at each measured angle on xenon at 175, 250, and 300 V _d from Floating to 30 V _e . The trend occurs for all discharge voltages.	141
Figure 95. Plume plasma potential throughout the plume for the Floating case.	143
Figure 96. Plume plasma potential for Floating, 10 V _e , and 30 V _e at 0 and 30 degrees.	143
Figure 97. In-channel plasma potential map for 150 V anode discharge with Floating, 10, and 30 V _e electrode conditions.	144
Figure 98. 30 V _e xenon potential contours with overlaid static magnetic field.....	145
Figure 99. Thrust on xenon at 20 A for various electrode conditions.	147
Figure 100. T/P ratio on xenon at 20 A for various electrode conditions.....	147
Figure 101. Specific impulse on xenon at 20 A.....	148
Figure 102. Anode efficiency on xenon at 20 A.....	148
Figure 103. 20 A electrode current.	149
Figure 104. Ion current density profile for floating election on xenon at 20 A with the 300 V, 9 A data for comparison.....	150
Figure 105. Ion current density for xenon at 20 A across all three electrode conditions (Floating - 30 V _e).	151
Figure 106. Plume divergence half angle for xenon at 20 A.	152
Figure 107. Normalized ion energy distribution function for xenon at 20 A with Floating electrodes at thruster centerline.	152
Figure 108. Ion energy distributions for the conditions tested at 20 A showing the three electrode conditions: Floating, 10 V _e , and 30 V _e	154
Figure 109. Most probable ion energy for xenon at 20 A. The data is less clear for the 20 A case. There is no definite jump in ion energy as was seen at 9 A.....	155

Figure 110. Change in most probable ion energy with the electrodes.....	155
Figure 111. Plume plasma potential for Floating, 10 V_e , and 30 V_e at 0 and 30 degrees.	156
Figure 112. Propellant efficiency defined as beam current/total mass flow rate.....	159
Figure 113. Total mass flow rate including cathode flow. There is an overall decrease in mass flow rate with increased electrode bias.....	160
Figure 114. Change in propellant efficiency comparing 25 V discharge increase from floating to 10 and 30 V_e electrode increase.	162
Figure 115. Centerline plasma potential for Floating, 10, and 30 V_e on xenon at 150 V_d	164
Figure 116. Centerline electric field for Floating, 10, and 30 V_e	164
Figure 117. Electron temperature in the discharge channel for Floating, 10, and 30 V_e .167	
Figure 118. Electrode current at 9 A for 10 V_e and 30 V_e electrode bias. Similar to the krypton tests, the electrodes draw in almost all of the current at 30 V_e	168
Figure 119. Electrode current for increasing cusp-magnet currents for 9 A on xenon at 175 V_d , 10 V_e . Higher magnetic current results in stronger cusp fields, which reduces electron flux to the electrodes.....	171

NOMENCLATURE

A_c	=	Faraday collector area, discharge channel exit area
$A_{effective}$	=	Effective faraday collection area
\vec{B}, B	=	Magnetic field vector and magnitude
D_r	=	Channel diameter ratio, outer/inner diameter
d	=	Diameter of filament wire
\vec{E}, E	=	Electric field vector and magnitude
e	=	Electron charge
g_0	=	Gravitational acceleration
h_c	=	Faraday probe collector and shield height
I_{axial}	=	Axial portion of ion beam
I_b, I_{beam}	=	Ion beam current
I_c	=	Collector current
I_D	=	Discharge current
I_E	=	Electrode current
I_e	=	Electron current
I_S	=	Sheath current
I_{SP}	=	Specific impulse
$J_{e, i}$	=	Electron and ion current density
k_A	=	Angle correction factor for Faraday probe
k_B	=	Boltzmann's constant
k_D	=	Distance correction factor for Faraday probe
k_G	=	Gap correction factor for Faraday probe
k_r	=	Electron-ion recombination constant
L_C	=	Channel length from anode to exit plane
M	=	Ion mass
m	=	Particle mass
m_i, m_e, m_n	=	Ion, electron, and neutral particle mass
$m_{initial}$	=	Initial spacecraft mass
m_{final}	=	Final spacecraft mass
$m_{propellant}$	=	Spacecraft propellant mass
$m_{structure}$	=	Spacecraft structural mass
$m_{payload}$	=	Spacecraft payload mass
\dot{m}	=	Mass flow rate
\dot{m}_i	=	Ion mass flow rate
\dot{m}_{tot}	=	Total mass flow rate
n	=	Number density
n_e	=	Electron number density
n_i	=	Ion number density
n_j	=	Number density of j^{th} species
n_n	=	Neutral number density
P_E	=	Electrode power
P_{jet}	=	Jet power
P_{in}	=	Input power
P_{tot}	=	Total power

q	=	Particle charge
q_i	=	Ion charge
q_j	=	Charge of j^{th} species
R	=	Distance of Faraday probe to thruster
R_C	=	Radius of Faraday collector
R_{CL}	=	Mean radius of channel centerline
$R_{L,R}$	=	Distance of Faraday probe to left and right channel in 2D plane
R_S	=	Radius of Faraday shield
r_g	=	Larmor or gyration radius
T	=	Thrust, temperature
T_e	=	Electron temperature
T_n	=	Neutral temperature
V_D, V_d	=	Discharge voltage
V_p	=	Plasma potential
$V_{p, raw}$	=	Raw measure plasma potential
V_f	=	Floating potential
V_a	=	Acceleration voltage
V_E, V_e	=	Electrode voltage
V_{grid}	=	Ion repulsion grid voltage
v_{crit}	=	Critical velocity
v_D	=	Drift velocity
v_e	=	Exit velocity, electron velocity
v_i	=	Ion velocity
v_n	=	Neutral velocity
$\langle v_i \rangle$	=	Averaged ion velocity
Δv	=	Velocity change
v_{\perp}	=	Particle velocity perpendicular to field
Z_i	=	Charge state

α	=	Electron-ion recombination constant
$\alpha_{L,R}$	=	Left and Right Faraday probe incidence angles
Γ	=	Gamma function
γ	=	Secondary electron emission ratio
ϵ_0	=	Permittivity of free space
η	=	Anode efficiency with electrode power included
η_A	=	Anode efficiency
η_b	=	Beam efficiency
η_p	=	Propellant efficiency
λ	=	Beam divergence angle
λ_D	=	Debye length
λ_i	=	Ionization mean free path
$\ln \lambda$	=	Coulomb number
$\mu_e, \mu_{e\perp}$	=	Electron mobility, mobility perpendicular to field
σ_i	=	Collision cross-section
ν_{ei}	=	Electron-ion collisions frequency

ν_{en}	=	Electron-neutral collisions frequency
ν_m	=	Momentum-transferring collision frequency
ϕ_p	=	Plasma potential
ϕ_{th}	=	Thermalized potential
ω_c, ω_e	=	Gyro frequency, electron gyro frequency
Ω_e	=	Electron Hall parameter
Φ	=	Potential

SUMMARY

This work focuses on improving the thrust-to-power ratio of Hall effect thrusters using in-channel electrodes to reduce ion-wall neutralization and focus the ion beam. A higher thrust-to-power ratio would give Hall thrusters increased thrust with the limited power available on spacecraft. A T-220HT Hall thruster is modified in this work to include a pair of ring electrodes within inside the discharge channel. The electrodes are biased above anode potential to repel ions from the walls and toward the channel centerline. Theoretical analysis of ion loss factors indicate that ion-wall neutralizations remove almost 13% of the total ions produced. Reduced wall losses could significantly improve the thruster performance without increased discharge power or propellant consumption.

The thruster performance, plume ion characteristics, and internal plasma contours are experimentally measured. The plume and internal plasma measurements are important to determine the cause of the performance changes. The thruster is tested in three conditions: no electrode bias, low bias (10 V), and high bias (30 V). The performance measurements show the electrodes do indeed improve the thrust and thrust-to-power ratio, the latter only at the low bias level. Adding bias increases the ion density and decreases the plume angle compared to the no bias case. The plume measurements indicate that the performance improvements at low bias are due to increased ion number density as opposed to increased ion energy. The increased ion density is attributed to

reduced wall losses, not increased ionization. The in-channel measurements support this due to little change in the acceleration potential or the electron temperature.

At the high bias level, a drop in thrust-to-power ratio is seen, even though a larger increase in thrust is observed. This is due to increased power draw by the electrodes. Plume measurements reveal the increased thrust is due to ion acceleration. The internal measurements show increased acceleration potential and electron energy which can lead to increased ionization. At the high bias condition, the electrodes become the dominant positive terminal in the thruster circuit. This causes the increased ion acceleration and the creation of domed potential contours that conform to the near-wall cusp-magnetic fields. The domed contours produce focused electric fields, which cause the decreased wall losses and plume angle.

CHAPTER 1

INTRODUCTION

1.1 Electric Propulsion Overview

The idea of using charged particles for spacecraft propulsion was first proposed by Konstantin Eduardovitch Tsiolkovsky, the originator of the rocket equation, in a publication in 1911. The theoretical idea was further expanded upon by his contemporaries such as Goddard, Oberth, and von Braun. Experimental research on electric propulsion did not start in the U.S. until 1958 when the U.S. Army approved the first research contract for ion engines for use as a space propulsion system.[1] Today, electric propulsion (EP) research is performed in multiple countries, and EP devices have seen continued use onboard satellites and deep space probes.

Space propulsion has two primary purposes, delivery of payload, and maintenance of payload orbit. Delivery typically relates to propulsion burns to place satellites and spacecrafts into their target orbits. This may be a geosynchronous orbit for Earth observation, or escape trajectory for planetary probes. Maintenance is the process of holding a steady orbit for the duration of the mission. Due to factors such as Earth's oblateness, Jupiter's gravitational pull, and solar winds, orbits decay over time and propulsion systems must be used periodically to reset the orbit. Historically, chemical rockets have performed both tasks with success, albeit at low efficiency. This can be seen from the Tsiolkovsky rocket equation as shown in Equation 1-1. The equation relates the orbital energy required for a given orbital maneuver, Δv , to the performance of the

propulsion system given as specific impulse, I_{SP} , and the mass ratio of the vehicle with and without propellant.

$$\Delta v = I_{SP} g_0 \ln \left(\frac{m_{initial}}{m_{final}} \right)$$

Equation 1-1

Specific impulse, shown in Equation 1-2 is a measure of the efficiency of rocket engines. It represents the impulse with respect to the amount of propellant used. If the amount of propellant is given in mass, the I_{SP} has units of velocity. More commonly the amount of propellant is given in terms of Earth weight, and an Earth gravity term is added which results in units of time. In the later form, the I_{SP} tells the duration an engine can produce 1 N of thrust with 1 kg of propellant. Higher I_{SP} means a more efficient engine.

$$I_{SP} = \frac{T}{\dot{m} g_0}$$

Equation 1-2

The rocket equation can be rewritten for the vehicle initial mass as shown in Equation 1-3. The initial mass is composed of the propellant mass and the final mass, which is the structure plus payload. The final mass is a constant, thus the only variable in the vehicle mass is propellant. Equation 1-4 shows the breakdown of the masses.

$$m_{initial} = m_{final} e^{\Delta v / I_{SP} g_0}$$

Equation 1-3

$$\begin{aligned} m_{initial} &= m_{final} + m_{propellant} \\ &= m_{propellant} + m_{structure} + m_{payload} \end{aligned}$$

Equation 1-4

From Equation 1-3, it is clear that for a given payload (m_{final}) and required mission velocity change (Δv), the performance of the propulsion system determines the initial mass, thus the amount of propellant necessary to perform the mission. The performance of a chemical rocket is limited by the energy available within the chemical bonds of the propellant that is consumed during combustion. This limits the specific impulse to a few hundred seconds. The space shuttle main engine (SSME), the most efficient chemical rocket engine to date, has an I_{SP} of 452 seconds. For large Δv missions, this means a final to initial mass ratio ($m_{final}/m_{initial}$), or the payload fraction, of 0.1 or smaller. This means over 90% of the total mass of the rocket is fuel. This leaves less than 10% for useful payload.

In comparison, the energy for acceleration in an EP system is independent from the propellant chemistry. Generally the acceleration energy comes in the form of an electric field that can be increased with the use of additional electrical power from the spacecraft. This allows for much higher specific impulses, in the thousands of seconds. This greatly increases the payload fraction for a given Δv . Figure 1 show the payload fraction plotted against the required Δv for the SSME and the NSTAR xenon ion engine used on the Dawn mission in 2007. As the graph shows, the percent of the total vehicle that can be used for payload with chemical systems decrease very quickly, which makes some missions impossible with a single chemical engine. EP systems on the other hand have larger payload fractions for a give Δv and have a much larger range of possible Δv 's, which make them attractive for a variety of missions.

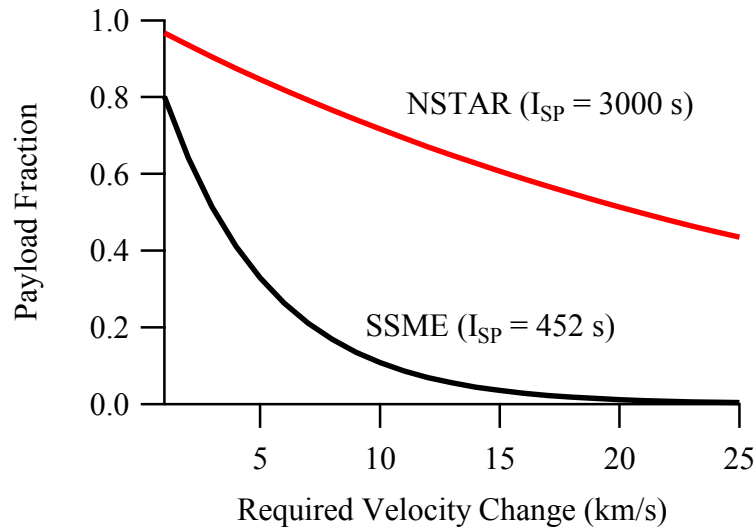


Figure 1. Payload fraction as a function of specific impulse for the SSME and NSTAR ion engine. The EP system is capable of higher payload fractions and longer missions.

Although EP systems have a very high specific impulse, the particles that are ejected to produce thrust are very light and the propellant flow rate is low, on the order of milligrams per second, consequently the thrust is very low. This means EP propelled spacecrafts require long burn times to reach high velocities. This subsequently causes long trip times for interplanetary missions. Typical thrust is in the 10 mN to 1 N range. For example, the NSTAR ion engine produced 90 mN of thrust. Currently, EP sees use as orbit maintenance engines for satellites where their combination of high I_{SP} and low thrust allow for long operational lifetimes and precise control, and as main propulsion for deep space probes where time to destination is not as critical as payload. Studies have been conducted to determine the effectiveness of EP systems to perform time sensitive and high Δv maneuvers such as orbit raising and plane changes for Earth orbiting satellites.[2-8] The goal of these studies is to determine the feasibility of EP to supplement the existing primary chemical propulsion system and eventually replace chemical as the sole satellite propulsion system. The use of EP to supplement an existing

chemical engine for orbit raising and station keeping has been shown to increase available on-orbit payload mass by 15-40 percent for a 15 year lifetime satellite.[8] The complete replacement of the chemical system with EP would further increase the available payload mass. **Studies have shown that EP systems are capable of performing these high Δv maneuvers; however an increase in the thrust-to-power ratio is needed and make them much more desirable as primary propulsion systems. Hall effect thrusters are one of the prime candidates for this role.**

1.2 Hall Effect Thruster Overview

Hall effect thrusters (HET) are one of the best candidates for primary satellite propulsion. They provide a combination of medium thrust levels (0.2 – 1 N) and I_{SP} that offers better performance for many near Earth missions over ion engines.[3, 8] They have been used on Russian satellites for the last 30 years, on the European Space Agency's SMART-1 mission, and recently on U.S. satellites such as Space System/Loral's MBSAT in 2004 and 2009.[9]

HETs are electrostatic EP devices that use an electric field to accelerate ions and produce thrust. HETs generate ions through collisional ionization where energetic electrons collide with neutral atoms and eject a valence electron, creating an ion and two electrons. In order to increase ionization ability, HETs trap electrons in a high density electron cloud. The electron cloud is created through perpendicular electric and magnetic fields that trap electrons by the Hall effect. The Hall effect describes the motion of a charged particle in the presence of crossed electric and magnetic fields. In the presence of a magnetic field, the path of a charged particle is curved by proximity to the field lines. The electron then spins or gyrates around the magnetic field line as seen in Figure 3.

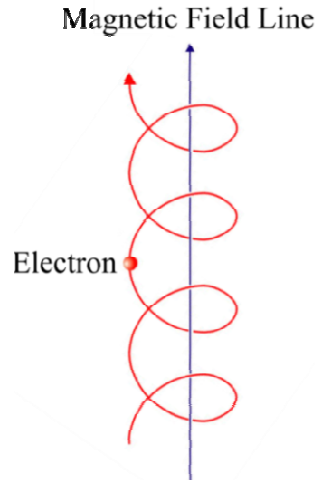


Figure 2. Electron gyrating around a magnetic field line. Magnetic fields bend charge particle motion into a tight spin, the radius of which depends on particle mass, velocity, and magnetic field. Electrons being much lighter than ions are easily trapped.

The radius of spin, or gyration, depends on the strength of the magnetic field and the mass and velocity of the particle. This is defined in terms of a Larmor radius or gyroradius, which is shown in Equation 1-5. The equation shows that the Larmor radius is determined by the particle mass (m), particle velocity perpendicular to the field (v_{\perp}), particle charge (q), and the strength of the magnetic field (B).

$$r_g = \frac{mv_{\perp}}{|q|B}$$

Equation 1-5

If the field is strong enough, the particles become trapped and spin around the field lines, a phenomenon called magnetization. In EP, typically only electrons are magnetized due to the magnetic field strength and the low mass of electrons. Due to this, electron transport perpendicular to magnetic field lines is retarded, but transport along field lines is largely unimpeded. Ions have much larger masses than electrons, order of 10^5 times for xenon and krypton. The larger mass means ions have a much larger

gyroradius, larger than the characteristic length of the device, and can be assumed to be unaffected by the magnetic fields.

If an electric field is applied perpendicular to the magnetic field, the electrons develop a drift velocity, v_D , perpendicular to both fields as defined by Equation 1-6.

$$\vec{v}_D = \frac{\vec{E} \times \vec{B}}{B^2}$$

Equation 1-6

This velocity causes a movement of the electrons across the magnetic field as shown in Figure 3. For this reason the Hall effect is also referred to as the $E \times B$ drift. The HET is an annular device with radial magnetic fields and axial electric fields. This configuration results in a circular drift around the annular discharge channel. The electrons drifting around the annular channel generate an electron current called the Hall current.

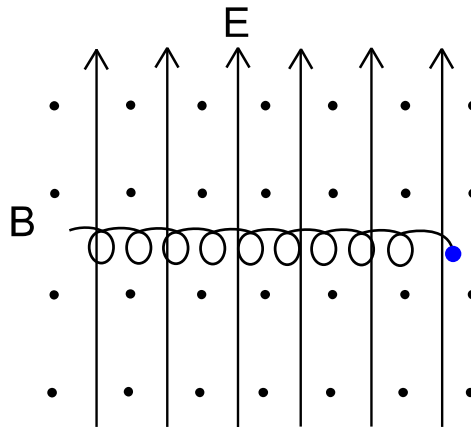


Figure 3. Hall effect motion of a charged particle. Electric field aligned vertically and magnetic field out of the plane of the page. Similar to spin about a magnetic field, the Hall effect motion is affected by the particle mass, thus electrons are greatly affected while ions are not.

The annular construction of the HET allows the Hall current to spin around the annulus without interference. The channel is either ceramic or metallic. The different channel materials lead to the two different types of HETs: the Stationary Plasma

Thrusters (SPT) with insulating ceramic channels [10-13] and the Thruster with Anode Layer (TAL) with metallic channels.[14-16] The two variants have similar physics, but different geometry and plasma behavior due to their different channel material. The SPT is longer axially and ion acceleration occurs over a longer distance, typically tens of millimeters, near and outside the channel exit. The TAL is much shorter and the acceleration occurs in a thin layer, on the order of the electron gyroradius, at the anode. In addition to the different lengths of the channel and acceleration region, the SPT has much lower electron temperature due to the high secondary electron emission (SEE) of insulating walls which causes cold electrons to be emitted and reduce the temperature. SEE is discussed further in Section 2.2.

An axial electric field is generated between the positive anode and negative cathode. The anode sits at the back of the channel and acts as both the positive electrode and the propellant distributor. A cathode mounted externally on the thruster acts as the negative electrode and provides electrons for the Hall current and neutralization of exhaust ions. Magnetic fields are generated by electromagnets that surround the discharge channel. The magnetic field is shaped by ferromagnetic materials to form a predominately radial field within the channel with maximum strength near the channel exit. This setup causes the Hall current to exist near the channel exit.

Figure 4 shows a schematic of a typical HET.

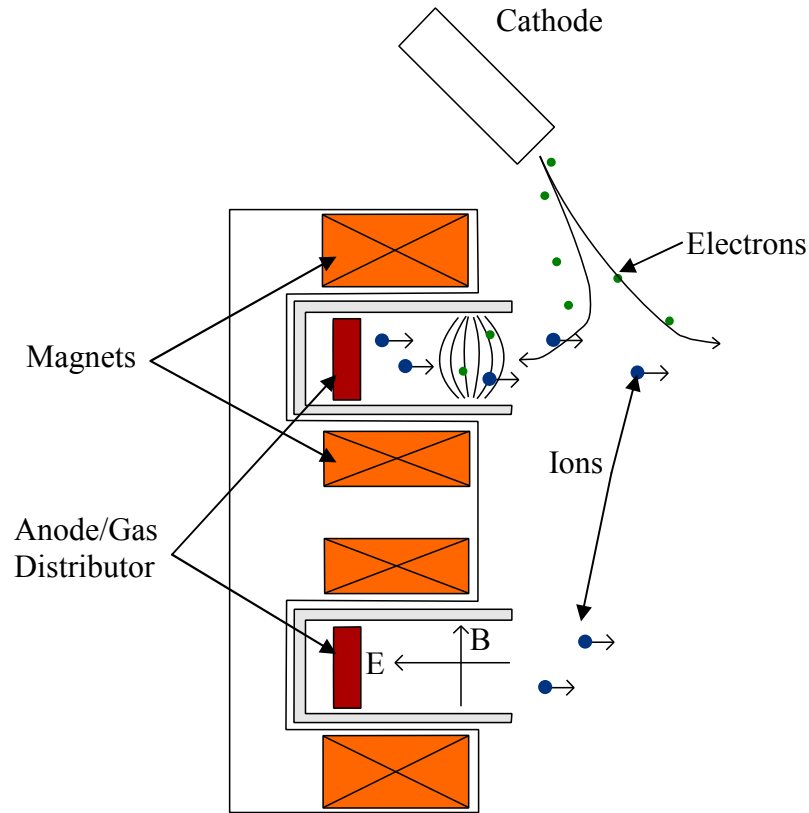


Figure 4. 2-D Hall effect thruster schematic. The thruster has an annular construction and is ideally axisymmetric.

Propellant atoms expelled from the anode are ionized by electron bombardment from the electron cloud as they proceed toward the exit. The electric field between the anode and cathode accelerates the ions out of the thruster. The thrust is the reaction to the ion acceleration that acts on the thruster through the magnetic field surfaces. Further downstream, free electrons emitted by the cathode recombine with and neutralize the ejected ions, preventing a charge build up on the thruster. A charge build up would decrease the electrical field within the thruster and thus reduce ion motions until no particles are emitted; this is called the space-charge limitation. The plasma of a HET is quasi-neutral throughout, thus avoiding the space-charge limitation and allows for high current and thrust densities.

The current in HETs is comprised of multiple parts. The current measured at the power lines and by the discharge power supply is the discharge current. This is the total electron current the anode collects. The discharge current is comprised of two components, the ion current, and leakage current. The ion current is equal to the ions leaving the thruster. What is actually collected by the anode are the valence electrons that are removed during the ionization process. This makes up a majority of the discharge current. The second component of the discharge current is the leakage current. This is comprised of electrons emitted from the cathode that cross the magnetic field lines to reach the anode. The leakage current must be reemitted by the cathode, thus is a power and efficiency loss term. A high ratio of ion to discharge current is desirable.

Flight versions of HETs are typically operated at their maximum efficiency point to reduce the size and mass of the Power Processing Unit (PPU). Efficiency is defined as the jet power, P_{jet} given in Equation 1-7, divided by the supplied electrical power, P_{in} , as seen in Equation 1-8. Here v_e is the exit velocity of propellant, \dot{m} is the mass flow rate, T is thrust which equals $\dot{m}v_e$, and V_D and I_D are the discharge voltage and current respectively. Equation 1-8 gives the anode efficiency, which only includes the discharge, or anode power. The power used to operate the magnets is not included as that varies greatly between different designs, so η_A is a better metric to compare different thrusters.

$$P_{jet} = \frac{1}{2}T v_e = \frac{1}{2} \frac{T^2}{\dot{m}}$$

Equation 1-7

$$n_A = \frac{P_{jet}}{P_{in}} = \frac{1/2 T^2}{\dot{m}V_D I_D}$$

Equation 1-8

1.3 Problem Statement

The two primary maneuvers required for satellites are orbit changes, and station-keeping. Orbit changes encompass orbit raising, where the altitude of the spacecraft is increased or decreased, and plane changes, where the angle of the orbit relative to the axis of the Earth is changed. These are typically large Δv maneuvers over a short period of time. Station-keeping on the other hand, require very small Δv in many firings over the lifetime of the satellite, typically 15+ years for modern satellites. The term station-keeping means maintaining the orbit of the spacecraft by using momentum control or small propulsive bursts to offset the effects of atmospheric and solar drag, tidal forces, gravitational forces from stellar bodies, etc. Historically, chemical engines are the system of choice for both types of maneuvers. Chemical engines are available in a large range of thrust levels. The rocket motors used for orbit changes, also known as apogee motors, typically operate with hundreds of Newtons of thrust. The Space Shuttle Orbital Maneuvering System has a thrust of 27 kN per engine. Chemical engines can also be designed to produce less than one Newton of thrust. However, chemical engines are limited in their specific impulse. Typical on-orbit engines operate in the 200-350 second range.

HETs typically operate with less than 1 N of thrust, but over 1000 seconds of specific impulse. The high I_{sp} of HETs allows for smaller fuel tanks and thus more room for payloads. Their low thrust however makes them a weak candidate for orbit changing maneuvers. Whereas a typical chemical system can propel a satellite from low Earth orbit

to geosynchronous orbit in days, an electric system would take weeks or months. For commercial satellites, for which a travel time of months may mean millions of dollars of lost revenue, and military satellites that require fast orbit changes to respond to developing situations, a quick transit time is a necessity.

In order to make HETs more desirable for use as primary propulsion systems on satellites, an increase in the thrust per unit power is required. Increased thrust is easy to accomplish since it is simply the product of mass flow rate and exit velocity. It requires either higher exit velocity (discharge voltage) or higher discharge current (mass flow rate). However satellites are both power limited and propellant limited, and operating at high thrust requires the thruster to become extremely inefficient, measured by the thrust-to-power ratio. **Thus, there is a need to increase the thrust-to-power ratio in HETs to enable a larger range of missions.**

1.4 High Thrust-to-Power Operation

HETs are generally optimized for high efficiency and I_{SP} . This requires operating at a high voltage, typically 300 V and above.[16-19] Equation 1-9 through 1-11 show the equations for thrust, I_{SP} , and efficiency. Thrust is the product of the mass flow rate and exit velocity of the particles. The exit velocity can be obtained by equating the kinetic energy equation $\frac{1}{2}mv_e^2$, with electrical potential energy, eV_D . I_{SP} is the thrust divided by mass flow rate and gravity. Finally anode efficiency is the jet or thrust power, P_{jet} , divided by the input electrical power, P_{in} . The voltage term disappears from the efficiency, however, if we consider a power limited system, which all spacecrafts are, then at constant power, a higher voltage results in a lower current, which increases the efficiency. Thus all three variables have a V_D dependence. This means the thruster

performance will increase with increasing discharge voltage, but not linearly. The discharge voltage is equated to the acceleration voltage applied between the anode and cathode. This V_D dependence is generally true, though reaches an asymptote at high voltages.

$$T = \dot{m}v_e = \dot{m} \sqrt{\frac{2eV_D}{m}}$$

Equation 1-9

$$I_{SP} = \frac{T}{\dot{m}g_0} = \frac{\sqrt{\frac{2eV_D}{m}}}{g_0}$$

Equation 1-10

$$\eta_A = \frac{P_{jet}}{P_{in}} = \frac{1/2 T^2}{\dot{m}V_D I_D} = \frac{\dot{m} \frac{2eV_D}{m}}{V_D I_D} = \frac{2\dot{m}e}{mI_D}$$

Equation 1-11

As voltage increases, the thrust increases, however the power required increases faster than thrust, thus there is an overall decrease in the thrust-to-power (T/P) ratio. High T/P ratio operation generally occurs at low voltages, which can be seen through a more detailed analysis of the equations. The thrust from an HET is due to the ejection of ions only, thus the thrust equation is rewritten to only account for ion mass flow and average ion velocity as in Equation 1-12. Equation 1-13 reduces the ion mass flow rate into a combination of the ion mass, ion beam current, and ion charge.

$$T = \dot{m}_i \langle v_i \rangle = \dot{m}_i \sqrt{\frac{2eV_D}{m_i}}$$

Equation 1-12

$$\dot{m}_i = \frac{m_i I_b}{e}$$

Equation 1-13

Combining Equation 1-12 and 1-13 results in a new thrust equation that shows the dependence on voltage and current (Equation 1-14).

$$T = I_b \sqrt{\frac{2m_i V_D}{e}}$$

Equation 1-14

The total discharge current is a combination of ion beam current and electron current as seen in Equation 1-15. For an efficient HET, the electron current is a small fraction of the total current, so for this first-order analysis, the discharge current and beam current are assumed equal. The electron beam current is added in later to show its effect.

$$I_b = I_D - I_e \approx I_D$$

Equation 1-15

Thrust divided by the input electrical power, which is equal to the product of the discharge voltage and current, gives the T/P ratio.

$$\frac{T}{P_{in}} = \frac{I_b \sqrt{\frac{2m_i V_D}{e}}}{V_D I_D} = \sqrt{\frac{2m_i}{e V_D}} \propto \frac{1}{\sqrt{V_D}}$$

Equation 1-16

Equation 1-16 shows the inverse dependence of the T/P ratio on discharge voltage for a constant power situation. There is an absence of discharge current from the equation, which says T/P ratio should be independent of current. In practice however, increasing current also increases the T/P ratio. This is due to ion beam current increasing faster than the electron beam current. Thus, as discharge current increases, the ratio $I_b/(I_b+I_e)$ increases, and the T/P ratio goes up as shown in Equation 1-17.

$$\frac{T}{P_{in}} = \frac{I_b \sqrt{\frac{2m_i V_D}{e}}}{V_D (I_b + I_e)} \propto \frac{I_b}{I_b + I_e} \frac{1}{\sqrt{V_D}}$$

Equation 1-17

There is a realistic lower limit on discharge voltage where the T/P ratio drops off sharply. Figure 5 shows this trend for a variety of thruster data and calculated T/P ratio compiled by Hofer.[20] This sudden drop at low voltages is caused by decreased ionization efficiency as voltage decreases. The ionization process in HETs is purely collisional, thus dependent on the electron energy, which is in turn dependent on the discharge voltage. A higher voltage provides greater electrical energy which results in more energetic electrons. As discharge voltage decreases, the average electron energy decreases, and thus the ability of the HET to ionize propellant decreases. Since the electrons have a Maxwellian like energy distribution, some of the electrons at the high tail end of the distribution will still have enough energy to cause ionization, but those are a small fraction of the total. The end result is decreased ionization ability and thus decreased number of ions at lower voltages. At the low voltage limit, the reduction in the number of ions available for acceleration will surpass the inverse discharge voltage dependence and cause the T/P ratio of drop. Another cause of ion number reduction is ion neutralization, specifically ion-wall neutralizations. When ions strike a surface, there is a chance of the ions being neutralized, the chance increases as ion energy decreases. **The challenge of high T/P ratio operation is operating at low voltage, while still maintaining adequate ion number density. This is the problem this work seeks improve T/P ratio by reducing ion-wall neutralizations.**

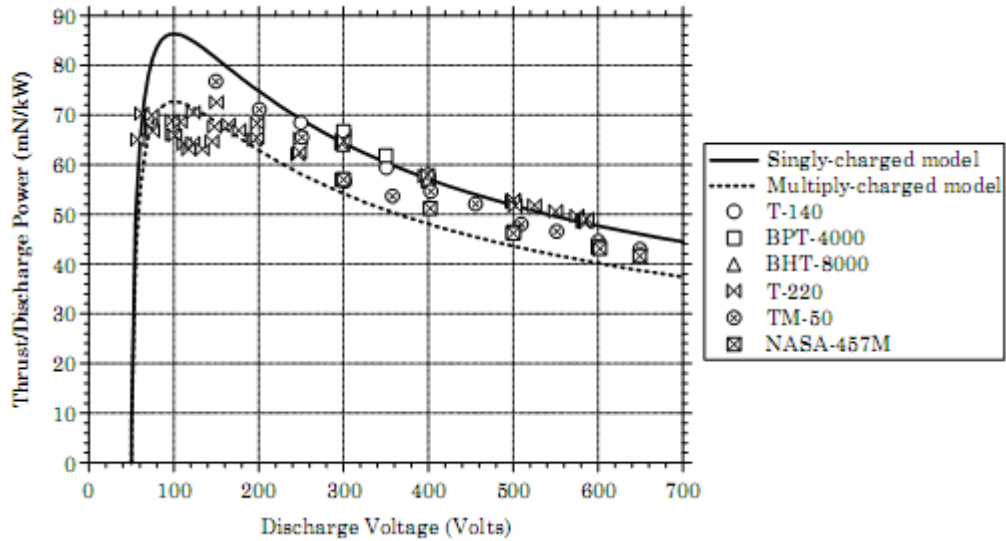


Figure 5. Thrust-to-power for various HETs compiled by Hofer.[20] T/P ratio increases as discharge voltage decreases until insufficient ion density causes T/P ratio to drop.

1.5 Research Contribution

The research presented in this thesis involves the use of in-channel electrodes to increase the T/P ratio of HETs by reducing ion-wall neutralization and focusing the ion beam. The T/P ratio increase is accomplished with the use of secondary electrodes along the channel wall biased above anode potential and shielded by cusp magnetic fields. The goal is a reduction in the ion-wall neutralization and beam divergence through shaping the in-channel, or internal potential contours to generate focusing electric fields. The addition of shielded secondary electrodes biased above anode potential is new in HET design. The magnetic field designed for this work also presents a new field topology not previously used in HETs. This work shows that the addition of biased electrodes with near-wall cusp magnetic fields can cause significant changes in the in-channel potential contours and lead to increases in overall performance.

1.6 Organization

The organization of this dissertation can be split into three parts: background information (Chapters 2 and 3), magnetic field design and performance of the initial stainless-steel electrodes (Chapter 4), and finally performance, plume and internal plasma measurements of the final graphite electrode design (Chapter 5 and 6).

Chapters 2 and 3 provide background information for the reader to familiarize themselves with the nature of the work and facilities. Chapter 2 describes the work to date on the areas of interest in this dissertation: in-channel electrodes, secondary electron emission from different materials, cusp-magnetic fields, and internal plasma potential structure. Chapter 3 discusses the facilities and equipment used in this work. The diagnostics used are described including their theory of operation and error.

Chapter 4 describes the initial work done on this project to design the magnetic field and the results of the initial design using stainless steel electrodes. The magnetic field design to incorporate cusp-magnetic fields is discussed first, followed by a discussion of thermalized potential and some theoretical performance improvements from looking at plume divergence. The HET performance results with stainless-steel electrode on krypton propellant are presented and discussed.

Chapter 5 presents the updated design that replaces the steel electrodes with graphite. The presence of the conductive graphite in the dielectric wall material is addressed. The thruster is then tested on krypton. The results are compared to the initial stainless-steel electrode data.

Chapter 6 continues the testing of the redesigned graphite electrodes with xenon propellant. More complete diagnostics are taken for xenon. The performance, plume, and internal plasma potential measurements are presented and discussed. Chapter 7 discusses

the findings and analysis of the results. Finally Chapter 8 summaries the major conclusions from this dissertation and suggestions for future work are proposed.

CHAPTER 2

BACKGROUND

2.1 In-Channel Electrodes

In standard HETs, the anode is the sole electrode within the discharge channel and is responsible for setting the acceleration potential. The addition of extra or secondary electrodes in HETs has been done before in the laboratory. Previous works with in-channel electrodes or similar additions are focused on the creation of a secondary anode for either two-stage operation or control of the anode temperature. Two-stage HETs have been a research interest since the 1970s.[14-16, 21-26] The goal of two-stage operation is to separate the normally overlapping ionization and acceleration regions to allow for individual control and thus improved performance. Research efforts in both Russia and the US on the D-80 [15] and D-100 [14] utilized an emissive electrode between the anode and exit plane for two-stage operation. The electrode is capable of emitting electrons through thermionic emission. In those works, it is found that two-stage operation increased thrust, I_{sp} , and efficiency over single-stage operation, but only at voltages greater than 500 V.

Raitses and Fisch utilized unshielded electrodes of various materials near the exit of the inner and outer channel walls to localize and control the acceleration field.[27, 28] Initially they used emissive electrodes biased to either cathode or anode potential. The theory is that the addition of the electrodes creates a localized potential drop separate from the regular anode-cathode potential. The magnetic field lines intersecting the electrodes would be at the corresponding potentials due to emitted electrons moving

along the field lines. This setup would create the ability to separate the ionization and acceleration processes in the HET, thus creating a two-stage effect.

Their secondary electrodes are located very near the magnetic field peak at the channel exit. Different combinations and placement of inner and outer electrodes are studied. Their results showed decreases in plume divergence angle, increases in propellant utilization, but a general decrease in thrust and efficiency. These observations are attributed to the different secondary electron emission (SEE) of the electrode materials changing the magnetic insulation. It is seen for a passive, or unbiased, electrode that the potential contours inside the channel shifted slightly upstream toward the anode, effectively moving the acceleration region.

Kieckhafer studied control of the anode temperature and performance changes with unshielded metal in-channel electrodes. Kieckhafer's electrodes acted as a secondary anode to pull discharge current away from the main anode to control anode Ohmic heating.[29] The goal is to control anode heating for the evaporation of bismuth for use as HET propellant. Both researchers observed various effects on the performance, the most noticeable is a reduction in plume divergence angle.[28, 29] The plume reduction effect is mainly attributed to the difference in the SEE coefficient between the metals and ceramics, which results in different sheath and potential drops. The modified wall-sheath potential reduces the off-axis velocity component of the ions, which correlates to an increase in thrust. Furthermore, both Raitses and Kieckhafer observed small increases in the T/P ratio with the unshielded electrodes. Drawing from their conclusions, it may be possible to enhance the ability of the wall sheath and potential

drop to collimate the ion beam through active control of the electrode potential and magnetic shielding with cusp fields.

Another similar use of wall electrodes is seen in the NASA-457M thruster shown in Figure 6.[30] The 457M has an anode that covers a large portion of the discharge channel. As shown in the picture, only a fraction of the channel length is comprised of ceramic material. Unlike a TAL thruster where the metallic walls float in the plasma, the 457M metal anode is biased. This creates a much larger potential surface than a standard ring anode. The exact magnetic field topography of the 457M is unavailable; however it is known to have a magnetic field similar to the NASA-173M HET. A preliminary magnetic field for the 173M v1 is shown in Figure 7. The field exhibits the typical characteristics of modern magnetic field design which will be detailed in Section 4.1.1.

The work done with the electrodes in this dissertation differs from the previous efforts with two-stage thrusters and the 457M in that the electrodes are separate from the main anode and biased above the anode potential. Additionally the electrodes are shielded with cusp-magnetic fields. Generally a two-stage effect is obtained by driving the second electrode to a potential between the anode and cathode, to create a two step potential profile. The electrodes in this work are biased above anode potential and have the observed behavior of stealing the discharge current from the main anode. The cusp-magnetic fields are a new addition to the use of secondary electrodes. The magnetic fields near the biased electrodes will interact with the local plasma to change the normal behavior of properties such as potential contours and the near-wall plasma sheath.



Figure 6. NASA-457M Hall thruster. The annular anode covers the rear plane and extends along the channel walls. Propellant injection occurs at holes along the inner and outer walls of the annular anode.[30]

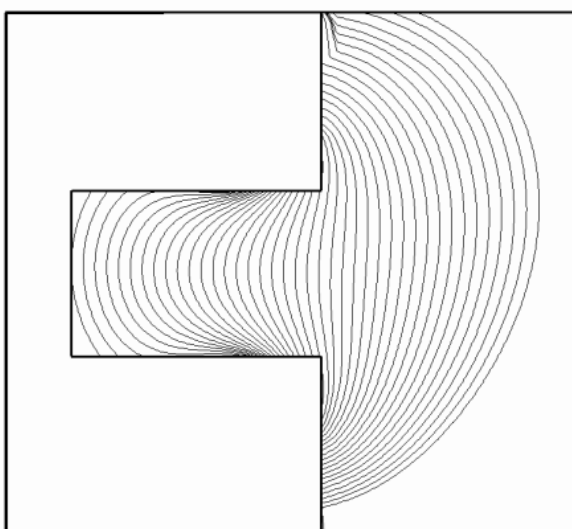


Figure 7. Magnetic field topography of the NASA-173Mv1. The field follows standard magnetic field design principles and generates predominantly radial fields in the channel. Similar fields are used for the NASA-173Mv2 and the 457M.[20]

2.2 Secondary Electron Emission

SEE occurs when an energetic primary plasma electron strikes a material and the collision ejects a second less energetic, or cold, electron. The SEE yield is defined as the ratio of secondary electrons to primaries.[31] The addition of cold electrons to a plasma will lower the average electron temperature. This can affect thruster behavior such as ionization ability, erosion, and electron mobility. In HETs, the electron temperature depends strongly on the material of the discharge channel. The two types of HETs, the Thruster with Anode Layer (TAL) and Stationary Plasma Thruster (SPT), differ largely by their channel material, which in turn affects other thruster characteristics. TALs use a metal channel, typically stainless steel, while SPTs use a ceramic channel, commonly boron nitride (BN). Ceramic usually has a much higher SEE than metals, and thus creates more secondary electrons when struck by a hot primary electron. This results in a lower electron temperature for SPTs.[32]

The expression for the exponential curve fit for SEE ratio, γ , due to electron bombardment is given by Equation 2-1.[33] Here T_e is the electron temperature in electron volts, a , and b are constants.

$$\gamma = \Gamma(2 + b)aT_e^b$$

Equation 2-1

Curve fits for experimental data by various researchers has produced the values of a and b shown in Table 1.[33-36] Figure 8 shows SEE curves for boron nitride (BN) and Stainless Steel (SS), the two standard channel materials for SPTs and TALs. As the graph shows, BN has more than double the secondary electron yield as stainless steel.

Table 1. SEE exponential curve fit values from Goebel.[33]

	a	b	Gamma(2+b)
BN	0.15	0.549	1.38
SS	0.04	0.61	1.44

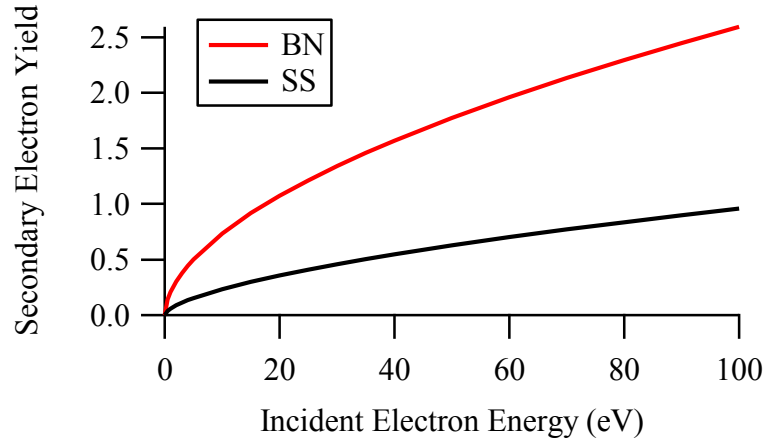


Figure 8. SEE curve fits for boron nitride and stainless steel from data in Table 1 for a range of electron temperatures. HETs typically operate in the 20 eV+ range.

The higher SEE can be beneficial in regulating the electron temperature. High electron temperatures (> 40 eV) cause highly energetic collisions which can produce double or triply-charged ions.[37] The ionization energies for the second and third ionization states are many times higher than the first. It takes more energy to create one doubly-charged ion than two singly charged. Thus, the creation of multiply-charged ions causes a drop in efficiency. The ceramic walls of the SPT helps to reduce the number of multiply charged ions. Changing the wall material, especially to higher SEE materials can have pronounced effects on the thruster. Raitses showed that above $400 V_d$, a high SEE material in the channel will cause increase discharge current and electron temperature.[38] Additionally, the high SEE causes increased electric field and electron mobility. These effects can greatly change the function of the thruster, for example by changing the size and location of the acceleration zone.[32, 38]

2.3 Cusp Magnetic Fields

The cusp-shaped magnetic fields used to shield the electrodes in this work are similar to those used in ion engines. In both cases they perform the function of electron trapping to prevention collision with a positively-biased surface: the anode in an ion engine, and the electrodes in this work. Ring-cusp ion engines are the most common type of ion engines because they can achieve very high efficiency with proper design. The cusp fields are generated by alternating polarity permanent magnets as shown in Figure 9.[33]

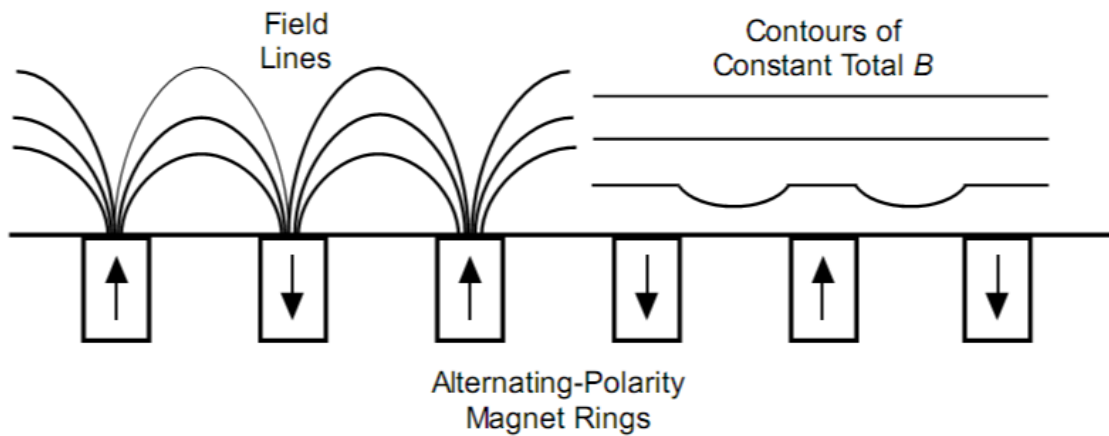


Figure 9. Ion engine cusp field schematic from [33]. The magnetic field lines indicate vector directions, while the contours show the magnitude of the field.

The right half of Figure 9 shows that the magnetic field magnitude flattens a short distance away from the magnets. In ion engines it is customary to define a closed magnetic field contour around the discharge chamber at 50-60 G. At this field strength, low-temperature electrons will become magnetized and trapped within the contour and prevented from being collected by the anode. In this work, electromagnets are added near the electrodes to achieve the same electron magnetization effect.

Cusp-shaped magnetic fields have been used in cylindrical HET research. As an annular device, standard HETs are difficult to scale to very small sizes, where they

become inefficient and suffer increased wall erosion.[39] The channel volume to surface ratio decreases to the point where wall losses become dominant and degrades the thruster performance. Cylindrical thrusters use a can-shaped channel instead of an annulus. They have reduced surface area without the inner wall and are easier to scale down.[40] Without a center magnetic pole and electromagnetic, the standard magnetic field is no longer possible, thus cylindrical thrusters use ring or cusp-shaped fields. Work done at the Princeton Plasma Physics Laboratory (PPPL)[39, 41, 42] and MIT[43] show the feasibility of such a thruster design.

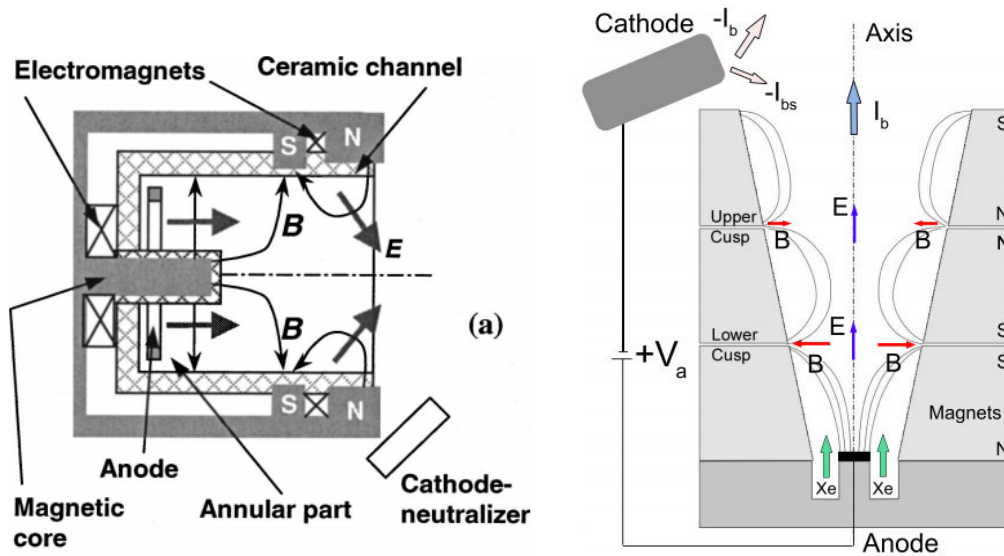


Figure 10. Cylindrical HET schematic from PPPL [41] (left) and MIT [43] (right). Both thruster utilize cusp-shaped magnetic fields along the walls due to the lack of a center magnetic pole.

The addition of extra electromagnets in an HET is a common technique in the laboratory. They are usually called trim coils, and acts as an in-situ magnetic field topology control when testing HETs. They have been added inside and outside the thruster to control different portions of the magnetic field. Trim coil use dates back to the Russian experiments on HETs in the 70's.[44, 45] More recently, internal trim coils have

been used by Kim[46] and King[47] to shape the channel field topology. Garrigues[48] and Day[49] added external coils to control the plume for thrust vectoring or plume divergence angle reduction respectively. To date, no work has been done that investigates placing a cusp-shaped field over the positive electrode in a thruster. Given in standard HETs the anode is the only positive electrode and the current knowledge of magnetic field design dictates no cusp fields, it is understandable.

2.4 Internal Plasma Potential Structure

The plasma interactions that occur in an HET within the discharge channel are in part driven by the plasma potential structure. The internal potential structure determines the size and location of the ionization and acceleration zone, and the electric field shape. The acceleration zone is defined as the axial length where the potential drop occurs. Figure 11 shows an example channel centerline plasma potential profile. Near the anode, the potential is at or very close to the discharge voltage potential. As the plasma moves downstream, the potential decreases little until near the channel exit. Near the discharge channel exit where the radial magnetic field is the peaks, the potential drops sharply over a short distance and reaches plume plasma potential. This sharp potential drop defines the acceleration region.

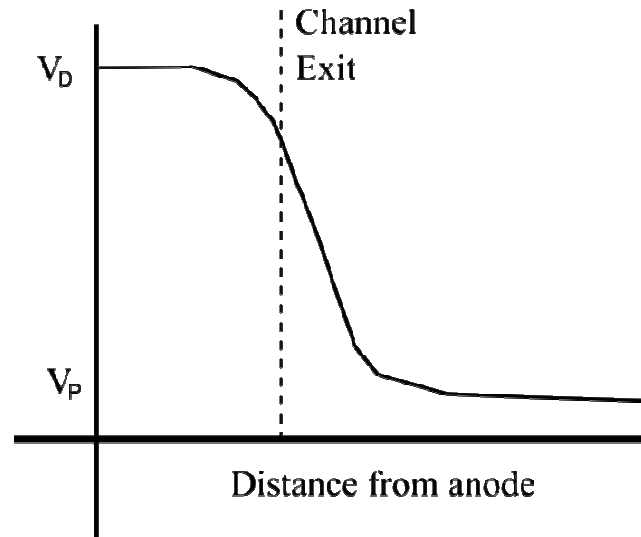


Figure 11. Example of the plasma potential profile along the discharge channel centerline. A significant portion of the potential drop and acceleration occurs outside the thruster.

The magnetic field plays a large part in the internal potential structure and the potential profile. The reason for the different rates of change in potential is the changing electron mobility in the channel caused by the varying magnetic field strength. The plasma potential is largely defined by electrons as they are the most mobile charge carriers. The potential difference between the anode and cathode cause the ions and electrons to be attracted to one or the other. Electrons emitted from the cathode start at a low cathode potential. They become trapped on the radial magnetic fields due to the Hall effect. The Larmor radius defines the level of confinement of the electrons along a given magnetic field line. Stronger fields cause smaller Larmor radii, thus reduced electron mobility across field lines. A higher potential gradient is then needed to pull particles across field lines and provide charge balance in the system. The radial magnetic field in the discharge channel peaks near the channel exit, and decreases as you move upstream or downstream. This means near the anode the plasma is weakly magnetized and electron mobility is high. Electrons have little difficulty reaching the anode, thus the local

potential difference is small. Figure 12 shows the axial electric field profile for HETs, which is the gradient of the potential profile. The electric field profile aligns well with the radial magnetic profile. The magnetized electrons at the radial magnetic field peak generate large potential drops and high electric fields.

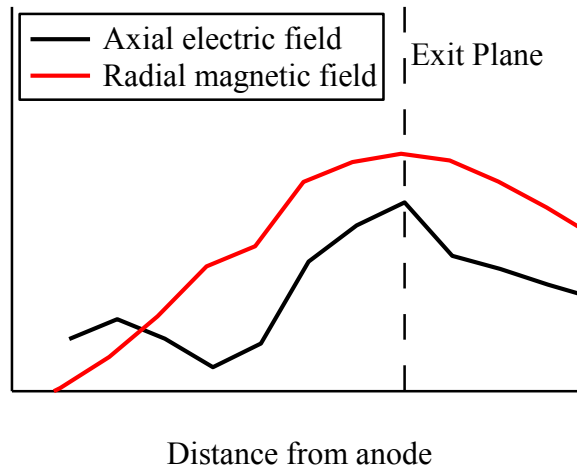


Figure 12. Axial electric and radial magnetic field profiles for HETs. The two fields peak near the same location.

Experimentally measuring the plasma potential inside the discharge channel is difficult. The difficulty arises primarily from the energetic discharge plasma inside the channel, and a desire to minimize disruptions to the plasma. The plasma potential in the discharge channel is near the anode potential, and the electron temperature can be tens of electron volts. This is a very hostile environment for the small probes necessary for good resolution measurements, for example the miniature emissive probe used in this thesis. The thin filaments used in these probes have very short lifetimes if immersed in the plasma for any significant period of time. Additionally, the energetic particles will collide and ablate the probe material, introducing foreign particles into the plasma. This can disrupt the standard plasma interactions and cause large errors in the data.

Some of the first experimental measurements taken of the internal potential profile of a HET are done by Haas. He developed a high speed linear motor capable of ~100 ms resident times inside the channel.[50] This allowed probes to survive for multiple tests, and minimized any disruption caused by probe ablation. Similar systems have been used since then to measure the internal plasma potential of different HETs.[51, 52] A system based on Haas's work was built at Georgia Tech and used in this investigation.

CHAPTER 3

FACILITIES AND DIAGNOSTICS

This chapter describe in the facilities and diagnostic tools used in this thesis.

3.1 Vacuum Chambers

The High-Power Electric Propulsion Lab (HPEPL) at Georgia Tech has two large Vacuum Test Facilities (VTF), VTF-1 and VTF-2. VTF-1 is a stainless steel diffusion pumped chamber 7 m long and 4 m in diameter. Twin 3800 CFM blowers and 495 CFM rotary-vane pumps rough the chamber and provide backing for the six 48” diffusion pumps that bring the chamber to high vacuum. The combined nominal pumping speed is 600,000 l/s on air and 155,000 l/s on xenon. The nominal base pressure is in the range of 1×10^{-5} Torr and the operating pressures seen in this work are below 3.2×10^{-5} Torr-Xe. A three axis motion control system with one meter axial and radial travel and 360 degree rotation allows movement of diagnostics during tests. A schematic and picture of the chamber are shown in Figure 13 and Figure 14 respectively.

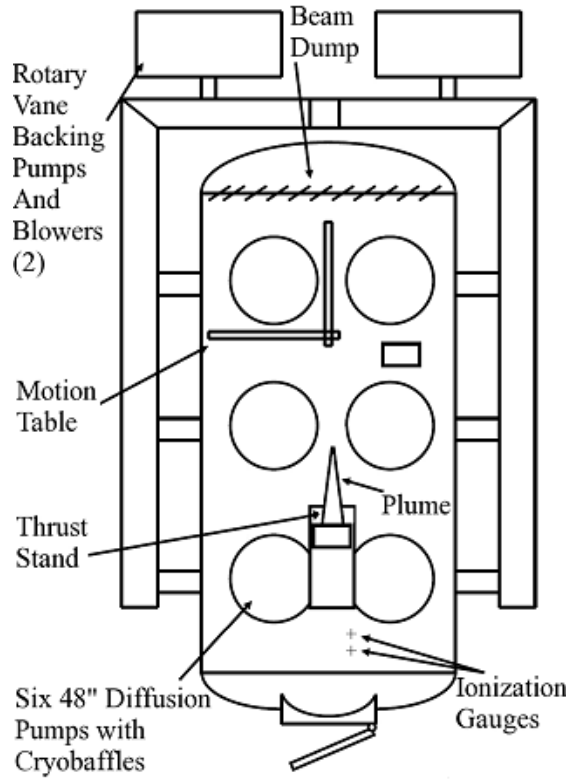


Figure 13. VTF-1 Schematic.



Figure 14. VTF-1 picture showing the blue diffusions pumps below.

VTF-2 is a cryopumped chamber 9.2 meters long and 4.9 meters in diameter. It is pumped to rough vacuum with one 3800 CFM blower and one 495 CFM rotary-vane pump. Ten liquid nitrogen cooled CVI TMI re-entrant cryopumps with a combined pumping speed of 350,000 l/s on xenon bring the chamber to a base pressure of 1.9×10^{-9} Torr. The system also incorporates a liquid nitrogen regeneration system to reduce operating costs. The regenerator is a Stirling Cryogenics SPC-8 RL Special Closed-Looped Nitrogen Liquefaction System with a reservoir capacity of 1500 liters of LN₂. Figure 15 and Figure 16 show a schematic and picture of VTF-2.

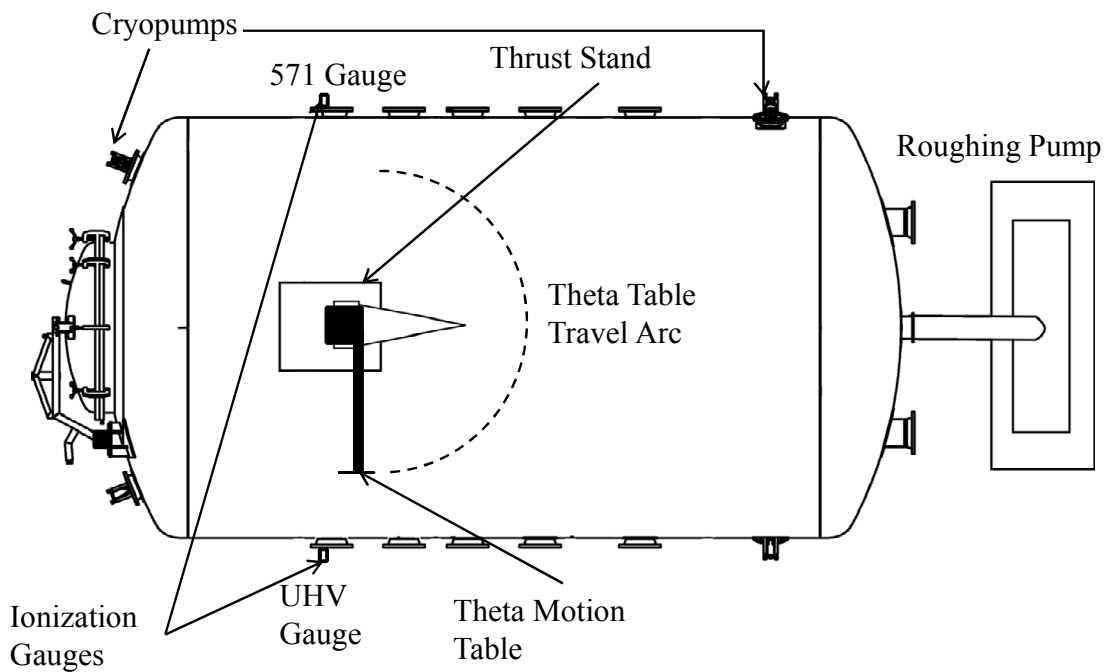


Figure 15. VTF-2 schematic.



Figure 16. VTF-2 picture.

3.2 T-220HT Hall Effect Thruster

All experiments are performed on a modified Pratt & Whitney Rocketdyne T-220HT HET. Extensive testing has mapped the performance of the thruster over a power range of 2-22 kW at discharge voltages of 200-600 V.[53] The T-220HT has a mean channel diameter of 188 mm, channel depth of 65 mm, and nominal power rating of 10 kW. An Electric Propulsion Laboratory 375 series cathode is located at the 12 o'clock position above the thruster and parallel to the local magnetic field lines. The cathode orifice is located approximately 30 mm downstream from the front face of the thruster and 178 mm from thruster centerline. The cathode flow rate is set to a constant 1 mg/s for all 9 A cases and 2 mg/s for all 20 A cases investigated. The discharge channel of the thruster is made of M26 grade boron nitride. A pair of electromagnets provides the magnetic field for operation. A more detailed description of the T-220HT and its characteristics can be found in Ref [53].

The T-220HT discharge is powered by either an EMHP 60 kW in VTF-1 or Magna-Power Electronics 45-kW power supply in VTF-2. All electrical connections enter the chamber through separate feedthroughs. The thruster discharge supply is connected to an RC filter consisting of a 1.3 Ω resistor and 95- μ F capacitor. The filter acts as a low pass filter preventing oscillations in the current over 1.4 kHz from reaching the discharge supply. High purity (99.9995%) krypton and xenon propellant are supplied to the thruster via stainless steel lines. MKS 1179A mass flow controllers meter the propellant flow to the cathode and anode. The flow controllers are calibrated with a custom fixed-volume apparatus measuring gas pressure and temperature as a function of time.

3.3 Diagnostics

A variety of diagnostics are used in this work to measure thruster performance and plasma properties. A null-type inverted pendulum thrust stand is used for all thrust measurements, which then allowed determination of other performance parameters such as I_{SP} and anode efficiency. Thrust plume data is taken with a Faraday probe, Retarding Potential Analyzer (RPA), and emissive probe. Finally, in-channel measurements are taken with miniature emissive probes mounted to a High-Speed Reciprocating Probe (HARP) system to allow for fast interrogation of the high-energy channel plasma.

3.3.1 Motion Systems

The both vacuum facilities have a three axis motion system manufactured by Parker-Hannifin. The X, Y, and theta tables are all software controlled. The X and Y axis have 1.5 meter travel with less than 0.5 mm positional accuracy. The theta table is capable of 360 degree motion with 10 arc-min of positional accuracy.

3.3.2 Thrust Stand

Thrust is measured with a null-type inverted pendulum thrust stand based on the NASA GRC design by Haag. The null-type stand holds the thruster at a constant position with use of PID controlled solenoid coils moving a center magnetic rod. Thrust is correlated to the amount of current through the null-coil required to hold the thrust stand at zero. Thrust stand calibration is performed by loading and off-loading a set of known weights. The resultant linear curve fit of the null-coil current versus weight (thrust) is used as the conversion for thrust measurements. A water-cooled copper shroud surrounds the stand and used to maintain thermal equilibrium. The thrust stand has an average error of $\pm 0.6\%$ of full scale. Further details of the thrust stand and its operation can be found in Ref [54].

3.3.3 Faraday Probe

The Faraday probe is a simple plasma diagnostic used to measure ion current density in the HET plume. The ion current density is proportional to the ion number density. The ion beam current and plume divergence angle can be obtained from Faraday probe data. Its use has been well documented.[3, 55-57] The probe is swept in a 2D constant radius arc through the thruster plume. The ion beam current is obtained from a spherical integration of the measure current densities. The plume divergence angle is calculated by comparing the axial portion of the beam current to the total beam current. The following sections discuss the operation of the probe, error sources, and finally the setup and probe used in this work.

3.3.2.1 Theory of Operation

In its simplest form, Faraday probes consist of a planar metal collector, disc biased below ground to repel electrons and collect incident ions. The ion current density

is determined from the current collected by the disc divided by the surface area. It is desirable to operate the probe in the ion saturation region where further decrease in collector potential does not significantly increase the observed ion current. If the ion saturation region is not reached, then the probe is not collecting the full ion current. This bias level can be determined by taking a voltage versus collected current sweep.

To reduce error, most Faraday probes have an additional guard electrode surrounding and planar with the main collector. The guard, or shield, electrode takes the form of a metal ring. A small air gap exists between the guard electrode and the collector to prevent conduction between the two. The guard electrode is typically biased to the same potential as the collector. The purpose is to create a uniform potential across the entire surface of the collector. This eliminates possible edge effects compared to the simplest case. Edge effects occur at the edge of the collector where the potential field bends to follow the curvature of the collector disk and thus presents a larger surface. Ions that would not directly strike the collector face are collected due to the expanded potential field. This can skew the results. With the guard electrode, edge effects still exist, but extraneous ions strike the guard and do not affect the collector.

Figure 17 shows a sample Faraday probe sweep of ion current density in the plume of the P5 HET at various background pressures.[58] Lower profiles result in smaller ion beam current. A profile with steeper gradients resulting in low current density at large angles has smaller plume divergence angle as seen in the black and blue lines.

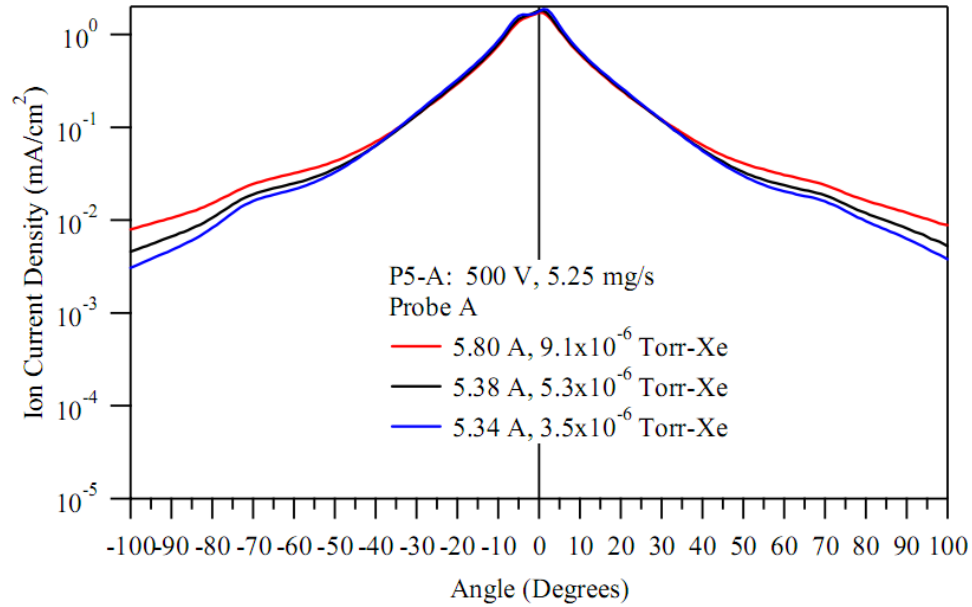


Figure 17. Example Faraday probe measurements of ion current density for varying background pressures.[58]

One of the uses of the ion current density profile is calculation of a plume divergence angle. The ion plume has a radial velocity distribution due to factors such as random thermal motion, electric field divergence, collisional angles, and charge-exchange (CEX) collisions with neutrals. The radial velocity results in a plume divergence, normally presented as the plume half angle that can be determined from the ion current density. Previous methods defined the plume angle as the angle from the centerline that contains 90 or 95% of the total ion beam current. This determination is made at the far-field, multiple thruster lengths downstream of the exit plane. The main source of error in this method is the contribution to the divergence due to CEX collisions.

CEX collisions occur when an energetic, fast ion collides with a slow neutral. The two particles exchange energy but retain their charge. This results in a slow ion and fast neutral. These collisions cause the ions to have a larger angular spread. The two sources of slow neutrals are propellant neutrals from the discharge channel, and residual chamber

neutrals. The latter is an effect of ground based testing that does not occur in orbit, thus standard far-field measurement of plume can over estimate the angle. To reduce these errors, measurements should be taken in the near-field plume where chamber CEX collisions are not yet present, [51, 59] or corrections such as the ones discussed in the following section should be applied.

3.3.2.2 Error

Faraday probes are a difficult diagnostic to use well. There are multiple non-systematic error sources that can contribute to large uncertainty in the data. This section describes some of the major sources and how they can be corrected for. As discussed previous, edge effects are one source of error, however that is easily addressed with the addition of a guard ring to the collector. A second source of error is secondary electron emission (SEE) from the collector due to ion strikes. SEE occurs when a high-energy ion strikes the collector surface and causes a low-energy electron to be emitted. This would artificially decrease the measured current as the ejected electron cancels an incident ion. Choosing a material with low SEE coefficient for the collector, such as tungsten, graphite, or tantalum, will mitigate this issue. In this work the collector is coated in tungsten which make the SEE error negligible.[60]

Two additional source of error present in Faraday probes are the uncertainty in the collector area, and the geometry of the measurement system. Brown performed a thorough analysis of both issues, and his results will be briefly repeated here for clarity.[61, 62] In standard Faraday probe analysis approaches, the collector area is taken as the geometric area of the collector face ($A_c = \pi R_C^2$). This is under the assumption that all the incident ions strike the collector face. In reality, ions can enter the air gap between

the collector and shield and strike the sidewall of the collector disk. This would increase the measure current and result in an inflated current density. To correct for this effect, Brown developed a gap correction factor, κ_G . The correction factor is calculated according to Equation 3-1.

$$\kappa_G = \pi(R_S^2 - R_C^2) \left(\frac{2\pi R_C h_C}{2\pi R_C h_C + 2\pi R_S h_S} \right)$$

Equation 3-1

Here R and h are the radius and height of the (s)hield electrode and (c)ollector. The gap correction factor is added to the geometric collector area to provide the effective area $A_{\text{effective}}$.

$$A_{\text{effective}} = A_c + \kappa_G$$

Equation 3-2

The effective collector area is 4.4 cm², versus the geometric area of 4.19 cm², an increase of 5%.

The second consideration for Faraday probe accuracy is the measurement geometry. The Faraday probe is typically swept through the plume on a constant radius probe arm. The arm has a central pivot point above the thruster exit plane. This creates a single pivot measurement. Meanwhile, in the 2D plane the HET is seen as two plasma sources due to the annular construction. There is a slight discrepancy between the data and the actual ion current if the measurements are analyzed without correcting for the dual sources. There were two corrections analyzed by Brown, one to account for variation in probe angle with respect to the sources, and the second to correct for the different path lengths between the probe and the two sources.

The first issue of probe angle arises due to the fact in a single pivot/single source system, the probe face is always perpendicular to the source in a 180° sweep. However with two point sources, the probe is only perpendicular at the two ends, 0 and 180°. This changes the incident angle of ions as they strike the collector, thus changing the effective probe collection area. The incident angles, α_L and α_R , for the left and right sources are calculated from Equation 3-3.

$$\alpha_{L,R} = \pm \left[\frac{\pi}{2} - \theta - \tan^{-1} \left(\frac{\cos(\theta) \mp (R_{CL}/R)}{\sin(\theta)} \right) \right]$$

Equation 3-3

The variables R_{CL} and R denote the median channel centerline radius and the probe measurement distance respectively. Figure 18 shows schematically the relationships between the various angles and distances.[62] The effect on the probe can be summed up as a correction to the effective collector area, κ_A .

$$\kappa_A = \cos^2 \left(\frac{\alpha_L + \alpha_R}{2} \right)$$

Equation 3-4

The left and right distances, R_L and R_R , are calculated based on the probe distance R from Equation 3-5.

$$\frac{R_{L,R}}{R} = \sqrt{\sin^2(\theta) + \left(\cos(\theta) \mp \frac{R_{CL}}{R} \right)^2}$$

Equation 3-5

The distance correction to the probe collector area, κ_D is:

$$\kappa_D = \left[\frac{1}{2} \left(\frac{R_L}{R} + \frac{R_R}{R} \right) \right]^2$$

Equation 3-6

The two correction factors κ_A and κ_D are applied to the measured current density.

The total integrated ion beam current, I_{beam} is obtained from Equation 3-7,

$$I_{beam} = 2\pi R \int_0^{\pi/2} \frac{I(\theta, R)}{A_{effective}} \left(\frac{\kappa_D}{\kappa_A} \right) \sin[\theta + \pi/2] d\theta$$

Equation 3-7

where $I(\theta, R)$ is the ion current measured by the Faraday probe at angle θ and distance R from the thruster centerline. This formulation includes the correction for the probe air gap mentioned previously.

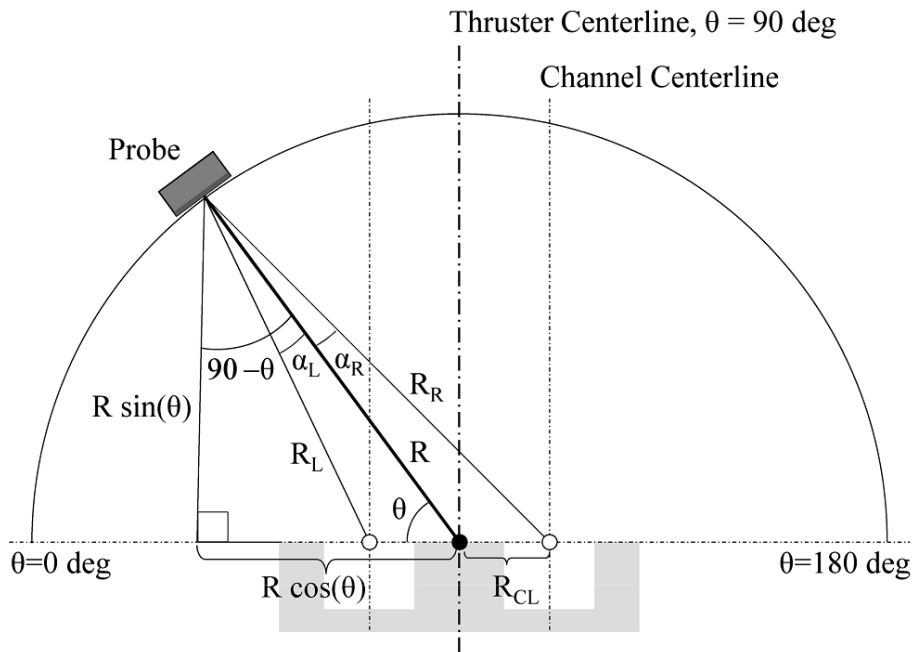


Figure 18. Measurement geometry for the Faraday probe. The angles and distances are shown for the correction for the two point sources. Figure is borrowed from Brown and Gallimore.[62]

To calculate the plume divergence angle, an evaluation of the axial beam current is needed. The axial ion beam formulation accounts for the difference in plume angle when referenced to thruster centerline versus channel centerline, another symptom of the two point source geometry. In Figure 18, the standard plume angle calculated for a single point source is taken from the probe to thruster centerline along distance R . In reality, the plume angle should be taken with respect to channel centerline along distance R_L . The axial beam current is calculated as,

$$I_{Axial} = 2\pi R^2 \int_0^{\pi/2} \frac{I[\theta, R] \cos(\alpha_A)}{A_{effective}} \left(\frac{\kappa_D}{\kappa_A}\right) \sin(\theta) d\theta$$

Equation 3-8

Here α_A is the angle ($90 - \alpha_L$) from Figure 18 and calculated as,

$$\alpha_A = \begin{cases} \tan^{-1} \left(\frac{\cos(\theta) - \left(\frac{R_{CL}}{R}\right)}{\sin(\theta)} \right) & \text{for } 0^\circ \leq \theta \leq \cos^{-1} \left(\frac{R_{CL}}{R} \right) \\ 0 & \text{for } \cos^{-1} \left(\frac{R_{CL}}{R} \right) \leq \theta \leq 90^\circ \end{cases}$$

Equation 3-9

With the axial beam current, the plume divergence half angle is calculated from Equation 3-10.

$$\lambda = \cos^{-1} \left(\frac{I_{Axial}}{I_{beam}} \right)$$

Equation 3-10

An additional and major source of error is charge exchange collisions due to residual chamber tank neutrals. Near thruster centerline, ions comprise a majority of the total particles and tank neutrals are sparse. At larger angles from centerline, the ion

density is lower, and ambient neutrals become a larger fraction of total particle density, thus CEX become a larger effect. The Faraday probe is unable to distinguish the difference between the fast ions from the discharge and slow CEX ions, resulting in artificially high current measurements at large angles. This leads to over-prediction of the ion beam current and plume angle. A low facility pressure will help to reduce the CEX error, but it is difficult to eliminate completely and can cause rather large uncertainties.

One method to adjust for the presence of CEX in the Faraday probe measurements is to measure the current density profile at multiple background pressures. The change in the measured current density due to CEX is relatively linear with backpressure. Thus, data can be extrapolated to zero backpressure and provide a better approximation of space conditions.[62, 63] This is done in VTF-2 prior to data collection using krypton propellant in order to determine the level of CEX contributions. The chamber pressure is artificially increased by flowing propellant krypton through an open line into the chamber. The same thruster operating conditions are measured with four different backpressure levels flowing 0, 25, 60, and 100 sccm of krypton. Figure 19 shows the measured current densities at 300 V_d . The data exhibits a clear linear trend and can be extrapolated to zero pressure.

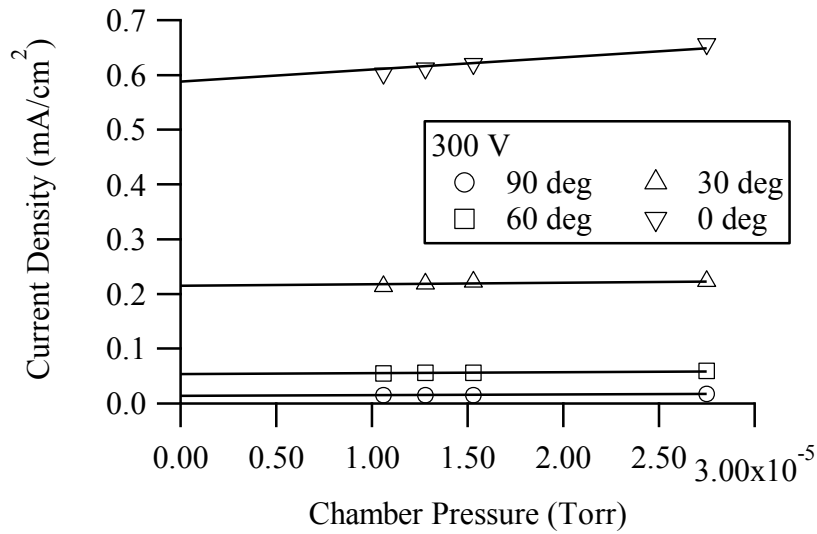


Figure 19. The backpressure variation of ion current density shows a linear trend. Extrapolation to zero pressure (space conditions) allows better approximation of true current density. Measurements are take 1 meter from thruster exit plane in the plume.

This extrapolation is done for all angles. Figure 20 shows two profiles comparing the chamber without artificially raised backpressure to the computed space current densities. The space condition correction reduces the current densities slightly, predominately near centerline and at large angles. This difference would cause an over estimation of the beam current and divergence angles. Figure 21 and Figure 22 show the calculated ion beam current and the plume divergence half angle. The CEX collisions results in a maximum 5% error in the beam current, and a 1.5% error in the plume angle. The error from CEX is deemed small enough, and the cost of propellant high enough, that the space condition extrapolation is not performed for all Faraday probe measurements.

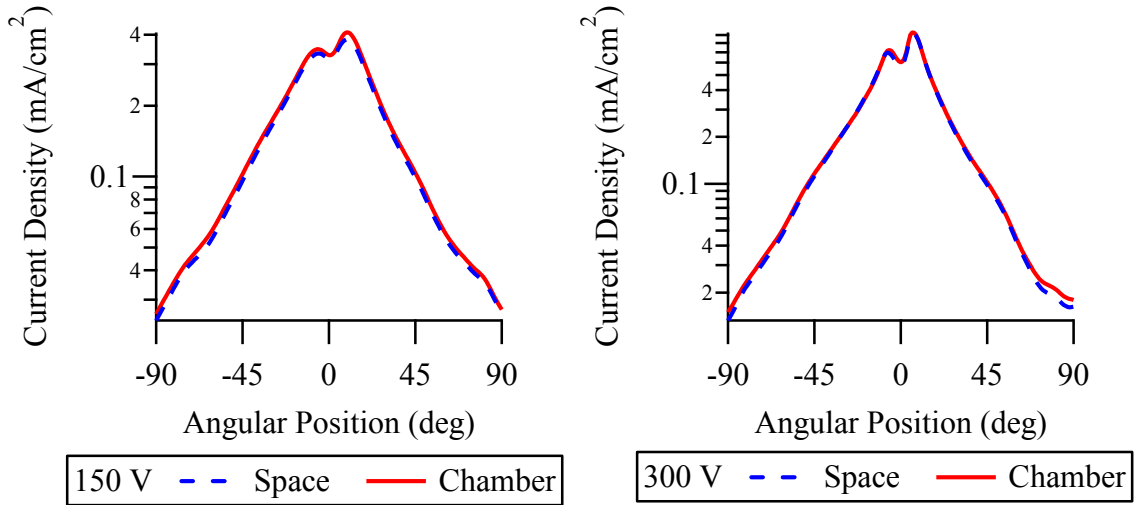


Figure 20. The measured chamber current profiles at 0 sccm are very similar to the computed densities for space conditions.

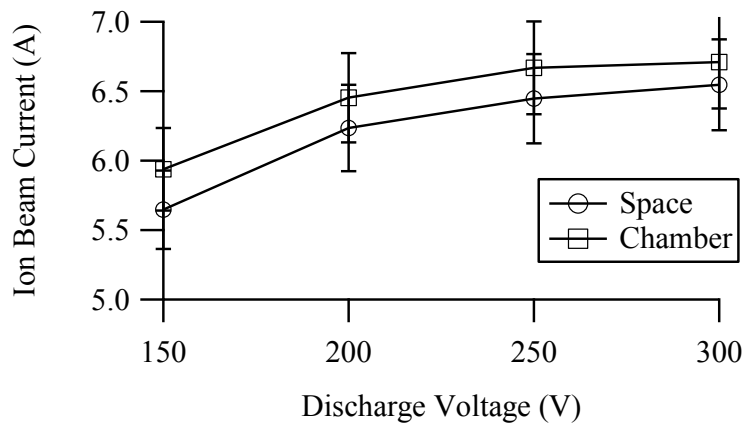


Figure 21. Beam current for the chamber and space conditions. The chamber condition exhibits slightly higher total beam current, largely due to CEX collisions creating extra ions from chamber neutrals.

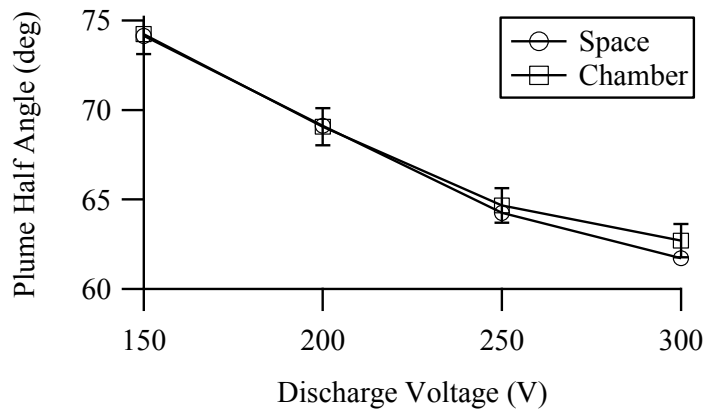


Figure 22. The plume divergence half angle for space and chamber conditions. The two have very similar plume angles, with slight differences at high voltage.

The divergence of the plume comes from two primary sources, initial ion trajectories from collisions and acceleration in the discharge channel, and ion interactions with thruster and chamber neutrals in the plume. The later occurs downstream of the thruster exit and significantly affects the plume angle while having negligible effect on the net thrust. Previous methods of taking the divergence angle as 95% of the total beam current over predict the plume angle due to plume interactions such as CEX collisions. For determination of ion divergence, it is thus best to take near-field Faraday measurements such that far-field CEX collisions can be ignored, or through calculation of I_{Axial} and I_{beam} at low background pressures as done in this work.

3.3.2.3 Setup and Design

A schematic and picture of the Faraday probe used is shown in Figure 23. The probe consists of a tungsten coated aluminum collector electrode with an aluminum shield electrode. The collector is 2.31 cm in diameter with a 1.15 mm gap between the collector and shield. The collector and shield are both biased to -20 V to repel electrons. Macor insulators are used to isolate the two electrodes. The overall length of the probe is one inch.

The Faraday probe is mounted on a one meter long radial arm connected to the theta motion table centered above the thruster. The probe is swept in a 180 degree arc around the thruster from -90 to 90 degrees with thruster centerline at 0 degrees. The collector current is passed through a 1.417 k Ω resistor and the voltage drop across the resistor is used to determine the ion current density. An electric schematic is shown in

Figure 24. Current measurements are taken throughout the plume and integrated to determine total current density. The plume divergence angle is determined by comparing the axial ion beam to the total ion beam according to Equation 3-10.

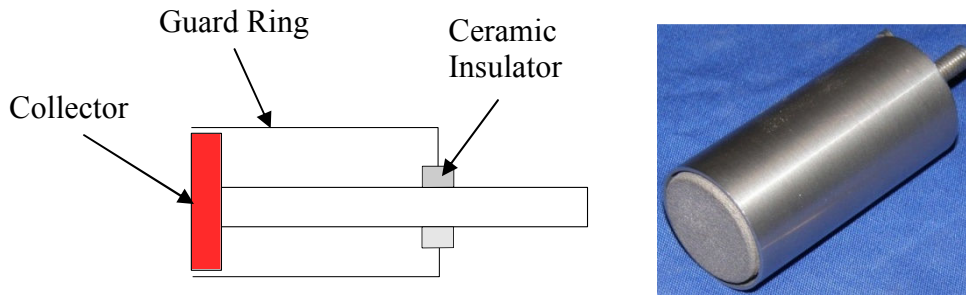


Figure 23. HPEPL Faraday probe diagram and picture.

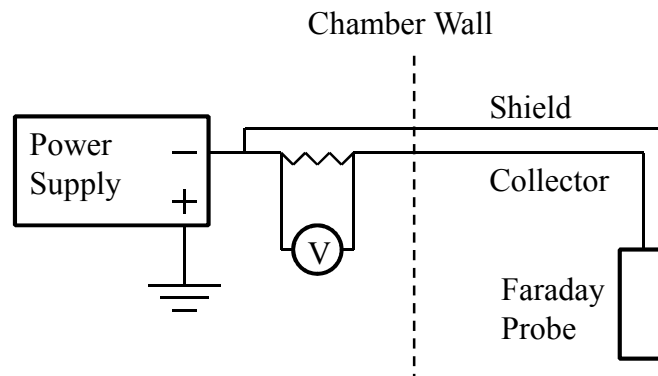


Figure 24. Faraday probe electric schematic.

3.3.4 Retarding Potential Analyzer

The Retarding Potential Analyzer (RPA) is a probe that measure ion energy distribution. The in-channel electrodes are biased above anode potential, thus providing an increase electric field. This may result in an increase of the ion energy. Using the RPA, the level of energy change caused by the electrodes can be determined. Along with the Faraday probe data, the two probes allow quantitative measurement if how the ions are affected. The following sections present the theory, error, and design of the RPA.

3.3.4.1 Theory of Operation

An RPA measures ion energy distribution by presenting a potential wall against which ions must climb to be measured. The probe uses a series of biased grids to selectively filter ions to determine their energy distribution.[20, 64, 65] A basic RPA consists of two grids and a collector. The first grid is the electron repulsion grid that is negatively biased to repel plasma electrons. The second grid is the ion repulsion grid that is positively biased to repel ions. The ion repulse grid potential is scanned from zero to the discharge voltage or above. When the grid voltage, thus potential energy, equals the kinetic energy of the ion, the ion is repelled while ions with higher energy move through grid and are collected and measured. Advanced RPA probes have more grids to reduce uncertainty. The probe acts as a high pass filter, allowing only ions with energy, or velocity, higher than the ion repulsion grid to pass through to the collector. Ions below a critical velocity, defined by Equation 3-11, are repelled. Here i is the interested particle species (electrons, ions, neutrals). Equation 3-11 comes from equating kinetic energy, $\frac{1}{2}mv^2$, with electrostatic grid potential energy, qV_{grid} .

$$v_{crit} = \sqrt{\frac{2qV_{grid}}{m_i}}$$

Equation 3-11

The critical velocity is dependent on the charge state and mass of the species. The ion current collected, I_c , by the probe can be calculated from Equation 3-12, where j is the charge state of the species

$$I_c = A_c e \sum_j n_j q_j \int_{V_{grid}}^{\infty} v f(v) dv$$

Equation 3-12

By substituting v_{crit} and its derivative (Equation 3-13) into Equation 3-12, the equation can be simplified to Equation 3-14.

$$dv_{crit} = \frac{1}{2} \sqrt{\frac{2q_i e}{m_i}} V_{grid}^{-\frac{1}{2}} dV$$

Equation 3-13

$$I_c = -\frac{q_i^2 e^2 n_i A_c}{m_i} \int_{V_{grid}}^{\infty} f(V) dV$$

Equation 3-14

Differentiating both sides with respect to the voltage V , yields

$$\frac{dI}{dV} = -\frac{Z_i^2 e^2 n_i A_c}{m_i} f(V)$$

Equation 3-15

For a discharge comprised of the same charge and same particle (q_i and $m_i =$ constant), Equation 3-15 provides the ion energy distribution, $f(V)$. However in a HET the plume is comprised of singly and multiply charged ions, with 10-35% being multiply charged depending on distance from the thruster and operating conditions.[66] In the far-field, where all the RPA data presented here is taken, multiply charged ions account for ~10% of the total particles. Since $V=E_i/q_i$, where E is the kinetic energy of the ion, q is the charge of the species, a singly-charged ion with energy E looks the same as a doubly-charged ion with energy $2E$.

Figure 25 below show a sample RPA data plot. The solid line is the raw collected RPA current. It decreases as the ion repulsion grid voltage increases. The dotted line shows the dI/dV profile. The collected current at varying voltages is reduced according to Equation 3-15, and the resulting dI/dV curve gives the most probable ion potential, V_{mp} ,

which characterized the ion energy and acceleration potential, and the Half Width at Half Maximum (HWHM) that characterizes the spread of the distribution.

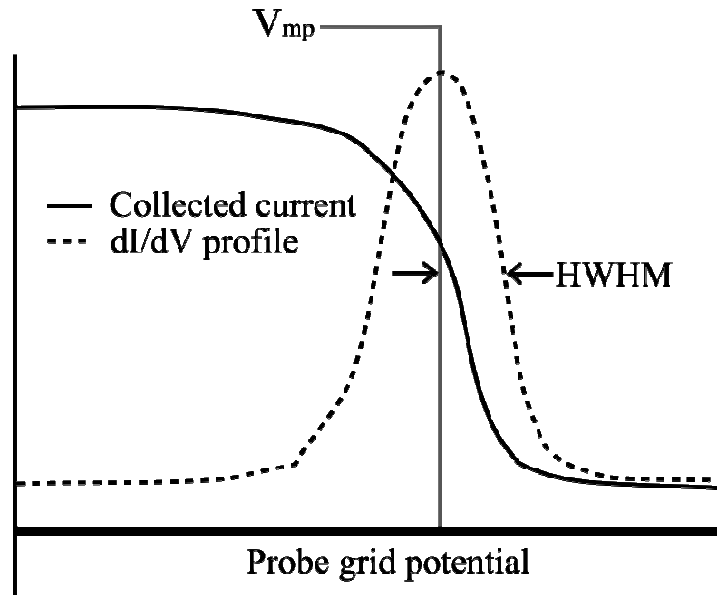


Figure 25. Example RPA ion energy measurement. The most probably energy is taken as the energy of the ion beam, and the HWHM characterizes the uncertainty.

3.3.4.2 Error

Two primary sources of error exist for RPAs. The first is SEE from the ion repulsion grid. Ions can interact with the grid in three ways: they can pass through, be repelled, or impact the ion repulsion grid. The ions that impact the grid can cause SEE. The emitted electrons are measured by the collector. This reduces the measured ion current. The primary method to reduce SEE effects is to use a second electron repulsion grid behind the ion repulsion grid to repel secondary electrons. This second grid is called the electron suppression grid. The suppression grid only needs to be biased slightly negative as secondary electrons have low energy, 1 – 2 eV typically.

The second possible error comes from small electron Debye lengths. The Debye length is the distance over which charge carriers shield out electric fields. In other words

it is the distance over which significant charge separation occurs. The potential across the electron repulsions grid holes are not uniform and decrease towards the center. Electrons with Debye lengths smaller than the grid holes may not be fully repelled and be able to move through the grid. This can be solved by making the electron repulsion grid more negative and thus have stronger repulsion.

The uncertainty in the most probable ion energy measurement can be estimated as 50% of the HWHM value. This value decreases with discharge voltage as the dI/dV profile becomes narrower. The uncertainty of the RPA measurements in this work varies from ± 5 V to ± 10 V depending on operating condition.

3.3.4.3 Setup and Design

The RPA used in this work is a modern design with of four grids before the collector, as shown in Figure 26. In order from right to left they are the floating, electron repulsion, ion repulsion, and electron suppression grids. The floating grid is unbiased and subsequently becomes charged to the plasma potential. This reduces perturbations caused by the biased grids. The electron repulsion grid is biased to -20 V to repel plasma electrons. The electron suppression grid is also biased to -20 V to repel secondary electron emitted due to ion collisions with the ion repulsion grid. The ion repulsion grid is scanned from 0 to 400 V with a Keithley 2410 Sourcemeter and the collector current is measured with a Keithley 6487 Picoammeter. A schematic of the electric setup is shown in Figure 27. The RPA is mounted on the same theta motion arm as the Faraday probe and offset by 5 degrees.

Two RPA sweeps are taken for each operating point. At each ion repulsion grid potential, three measurements are taken and averaged to produce the recorded value. A

4th-order Savitzky-Golay smoothing filter is applied to the raw data prior to taking the derivative.

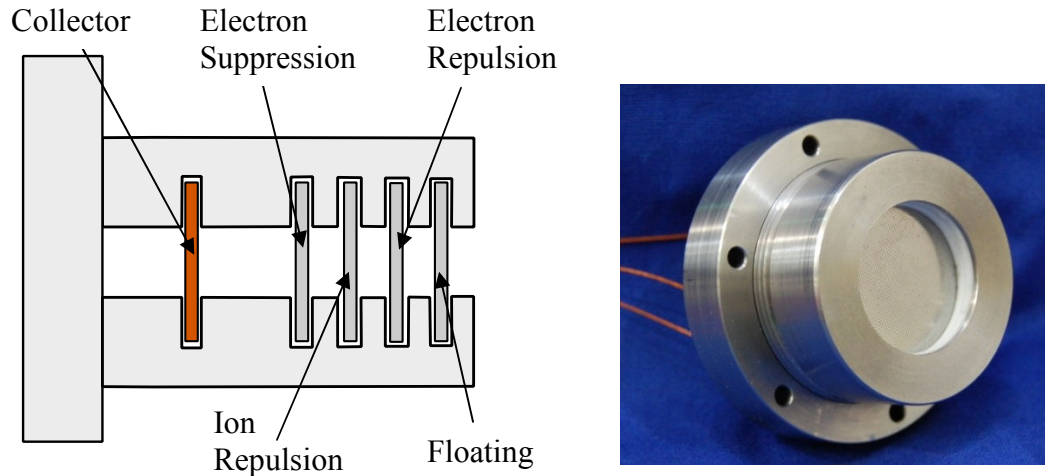


Figure 26. HPEPL four grid RPA diagram and picture.

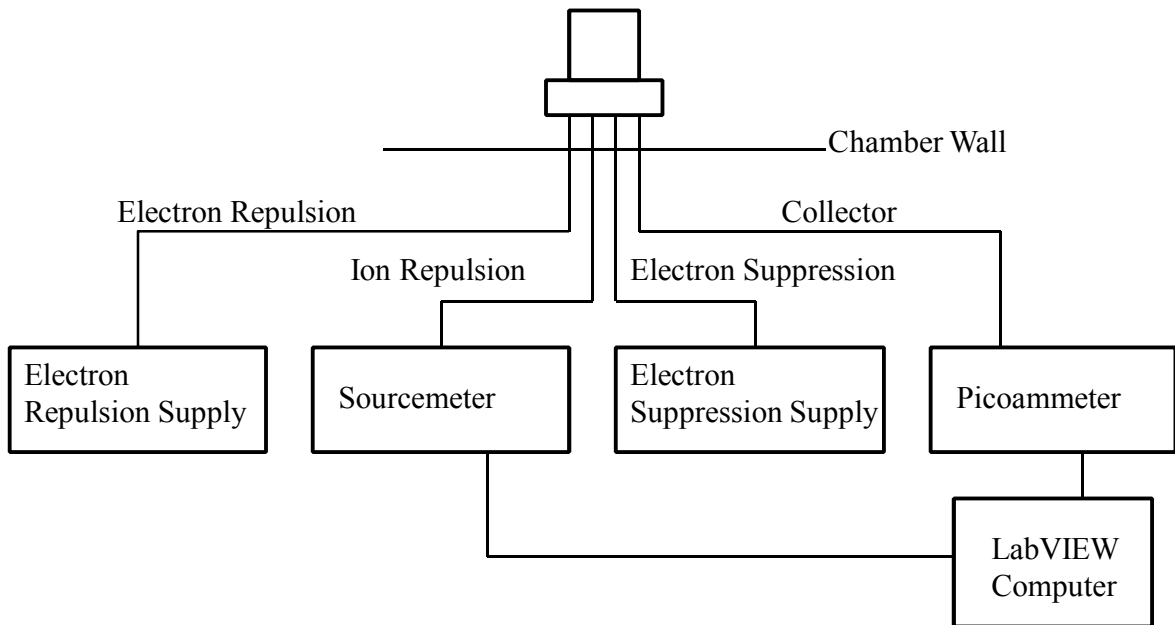


Figure 27. RPA electric schematic.

3.3.5 HARP

The High-Speed Reciprocating Probe (HARP) is a linear motor system capable of very high speeds and accelerations. The system allows for fast interrogation to minimize

disturbances to the plasma caused by inserting a probe into the plasma. The HARP is capable of speeds up to 3 m/s, with residence times of 50 ms. A picture of the HPEPL HARP is shown in Figure 30. The HARP is used primarily to study the in-channel plasma where its short residence times are necessary [11, 67]. Measuring inside the channel presents two problems, namely probe interference with normal plasma behavior and probe damage. In plasmas with highly energetic particles, probes will experience sputtering or ablation due to direct particle impacts on a very short time scale (< 1 s). The ablated material can interact with the local plasma and change the plasma parameters resulting in incorrect measurements. Prolonged immersion in the plasma will also cause severe damage to probes. Using a fast interrogation system reduces or eliminates these problems.

Theoretical calculations by Hass [11] on an alumina insulated probe gives a minimum ablation time of 150 ms for alumina in a 5-kW HET. The discharge conditions measured in this work is always below 5 kW. The lower power increases the minimum ablations times and allows longer residence times. The HARP speed is set to provide a 120 ms residence time in the HET channel. The HARP has a positional accuracy of 1 μ m. Figure 28 and Figure 29 show sample data of the HARP position as it relates to the potential measurement and discharge current oscillations. The short residence time of the probe is sufficient for the measure potential to be flat. The high speed of the probe also causes minimal perturbations to the thruster as seen in the current oscillations.

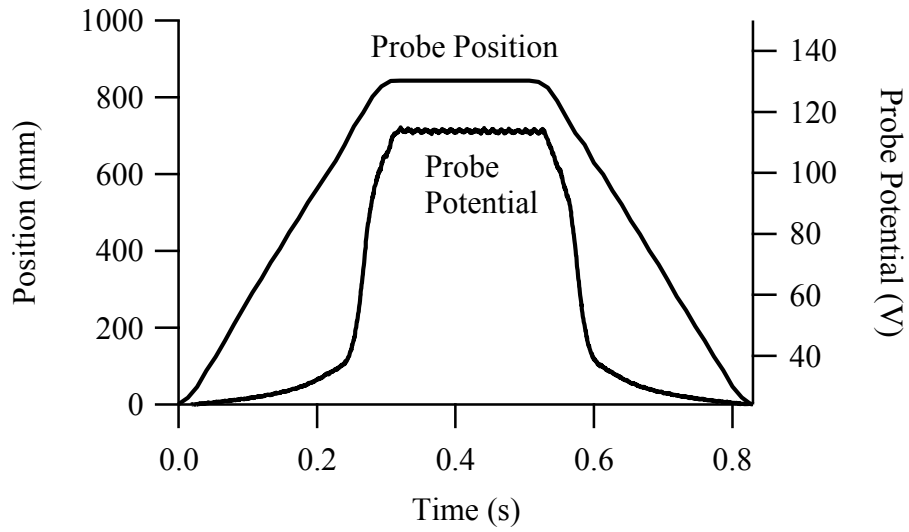


Figure 28. Example HARP position and measured probe potential. The potential is nearly flat for the short time it is at the target location, and has a very steep rise and fall when the probe enters and leaves the discharge channel.

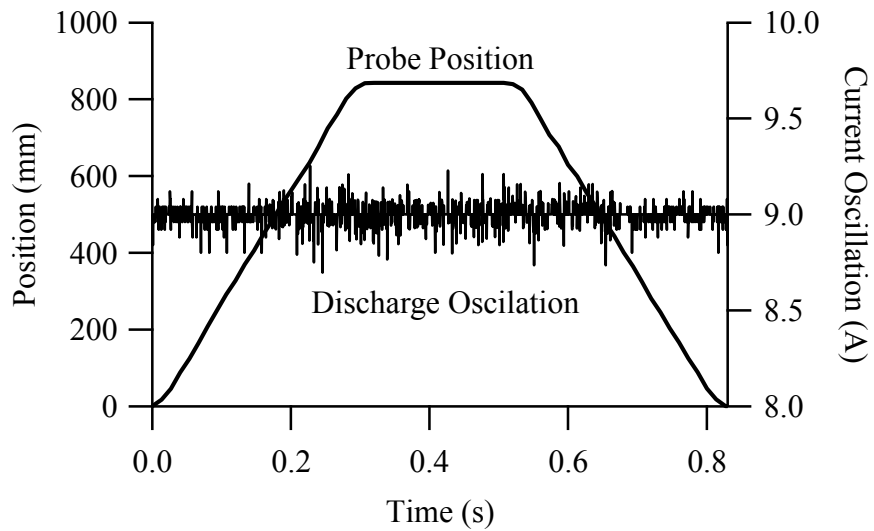


Figure 29. Example HARP probe position and discharge current oscillations. The insertion of the probe causes small increase in discharge oscillation as measured at the discharge power supply line.

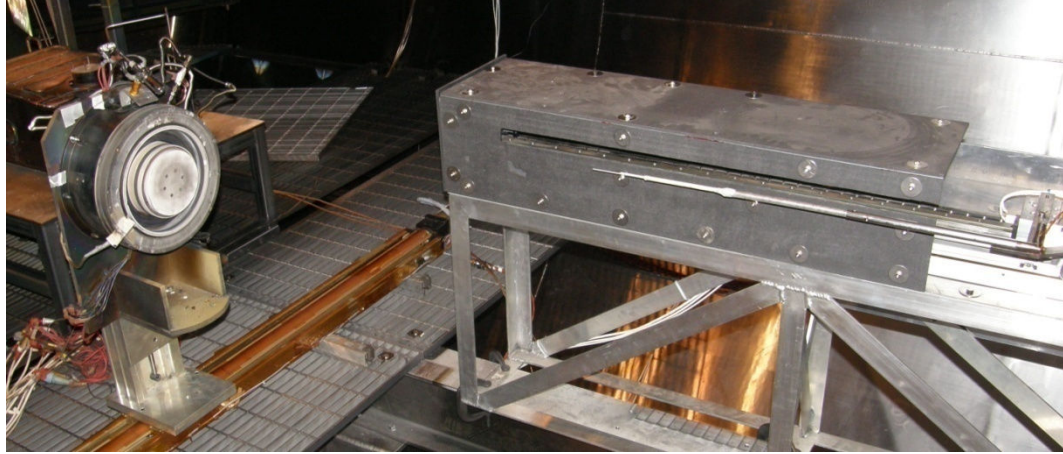


Figure 30. The HARP (right) and the modified T-220HT HET (left) in VTF-2 prior to testing. The miniature emissive probe is mounted on the HARP arm.

3.3.6 Floating Emissive Probe

The in-channel plasma potential is measured using floating emissive probes. The theory of emissive probes is well established, [29, 68, 69] and similar use to characterize in-channel properties have been done before [11, 52, 67]. The emissive probe is preferable for plasma potential measurements as it allows instantaneous measurement without prior data reduction. The emissive probe can be operated in two modes, biased or floating. The probe is used in floating mode in this work, but both are discussed below.

3.3.6.1 Theory of Operation

Emissive probes are simple probes made of a filament loop that is exposed to the plasma. The filament is typically made of a material with low work function, such as thoriated tungsten. A DC current is used to heat the filament until thermionic emission of electrons is achieved. The emitted electrons sit on the surface of the probe until subject to a potential difference. In the biased mode, a voltage sweep using a second power supply is performed. The resultant current is measured to produce an I-V curve. When the probe is biased below plasma potential, the electrons from the filament are repelled by the

potential difference between the probe and local plasma and escape into the ambient plasma. This creates an apparent ion current to the probe or decreased electron current. As electron emission increases, the measured probe current decreases rapidly as probe voltage is decreased. This is caused by an increasing potential hill between the probe and plasma allowing easier escape for surface electron. Eventually the current will flatten out and reach a sort of ion saturation region, though it will not be the same as the actual saturation current, thus emissive probes are not particularly useful for ion saturation measurements.

If biased above plasma potential, the probe immediately collects any emitted electrons, resulting in no net current. An electron sheath now forms around the probe. As the potential is further increased, the sheath does not expand greatly due the abundance of electrons available from the thermionic emission to counteract the increasing potential. This makes the slope of the electron saturation region much shallower, and allows easy analysis.

The second mode for emissive probes is floating. When used as a floating probe, no secondary scanning voltage is applied to the probe, though a heating current is still applied. When exposed to the plasma, any material naturally floats from ground to the floating potential. At the floating potential a sheath forms around the probe and there is no net current to the probe. This is due to the negative plasma electron current balanced by the positive plasma ion current and secondary electron emission. However, because the emissive probe emits its own electrons, the probe becomes more positive, which in turn draws in more plasma electrons. This process continues causing the probe potential to increase until it reaches the plasma potential. The emitted electron flux escaping into

the plasma decreases as the probe potential increases due to a shrinking potential hill between the probe and plasma, until the probe reaches the plasma potential or slightly above, at which point emitted electrons return to the probe. The measured probe current plateaus at this point and the probe floats at the plasma potential. Figure 31 shows an ideal example of emissive probe data. The plasma potential and a point of insufficient electron emission are shown.

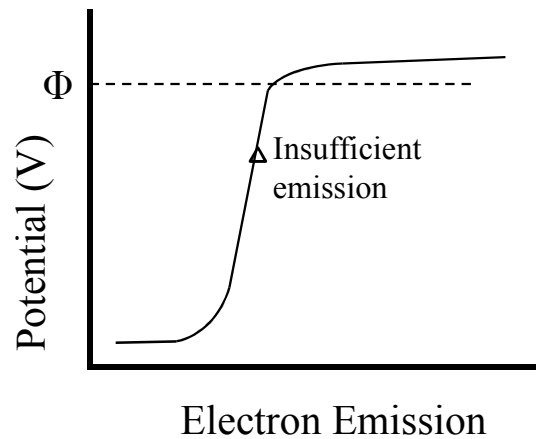


Figure 31. Ideal emissive probe thermionic emission curve. The measured potential plateaus once sufficient electron emission is reached. At this point the probe is at the plasma potential.

One issue that complicates emissive probe data analysis is a mismatch in probe and plasma electron temperatures. To account for the error introduced by the electron temperature mismatched, the measured potential is corrected by adding $0.6 T_e$ according to Equation 3-16.[51]

$$V_p = V_{p,raw} + 0.6T_e$$

Equation 3-16

V_p is the calculated plasma potential in volts, $V_{p,raw}$ is the raw measured potential in volts, and T_e is the local electron temperature in eV. The electron temperature can be calculated from the floating potential by Equation 3-17,

$$V_p - V_f = -\frac{k_B T_e}{e} \ln \left(0.605 \sqrt{\frac{2\pi m_e}{m_i}} \right)$$

Equation 3-17

where V_f is the floating potential, k_B is the Boltzmann constant, e is the electron charge, and m_e and m_i are the electron and ion masses respectively.

3.3.6.2 Error

For unbiased, floating emissive probe operation, the two largest contributions to deviation from ideal probe behavior are space-charge limitations and magnetic fields. Ideally the electron emission is able to increase continuously until the probe reaches the plasma potential. However in reality the emission is limited, and stops before reaching plasma potential as pointed out by Chen [69]. The emitted electrons have a much lower energy than plasma electrons, on the order of 10-100 times less. The much faster plasma electrons will thus provide a larger current than the slow emitted electrons can cancel. At high enough probe potential the plasma electrons overwhelm the emission rate and the probe current plateaus; however the measured potential is lower than actual plasma potential due to the extra plasma electrons. The measure potential is equal to the true plasma potential only when the probe electron temperature equals the plasma electron temperature. This error can be corrected for by adding a factor of the electron temperature as shown in the previous section.

Due to the reliance of the emissive probe on emitted electrons, strong magnetic fields can adversely affect the measurements. Strong magnetic fields can magnetized electron and cause errors in the potential measurement. To reduce the effect, the probe filament diameter needs to be less than the electron gyro radius. Hershkowitz [70] indicated condition as shown in Equation 3-18

$$B \ll \frac{4.8(T_e)^{1/2}}{d}$$

Equation 3-18

where B is the magnetic field in Gauss, T_e is the electron temperature in eV, and d is the filament diameter in cm. The filament used in this work has a diameter of 0.013 cm, and the minimum electron temperature in the channel is conservatively estimated at 5 eV. This results in a maximum B field less than 825 G. The maximum B field in the thruster is 300 G. Thus, the error caused by electron magnetization should be minimal.

A final source of error is the potential drop across the filament caused by the heating power supply. The heating current necessary to bring the probe to thermionic emission in this work is typically in the 3.3 A range. Due to the long cable runs this requires a heating voltage around 8 V. This voltage is applied half to each leg of the probe, and introduces a ± 4 V uncertainty in the potential measurements.

3.3.6.3 Setup and Design

A schematic of an emissive probe is shown in Figure 32. Two emissive probes of difference sizes are used in this work. The large probe has an alumina tube diameter of 5 mm and the filament loop has a diameter of 3.5 mm. This probe is used in the thruster plume to measure the plume plasma potential for the RPA data analysis. A second, miniature emissive probe is used to measure the internal plasma potential. The miniature

probe consists of a series of nested alumina tubes ending in a 0.8 mm diameter double bored alumina tube. The filament loop of the miniature probe is only 1.3 mm in diameter. The emissive filament used in both probes is 0.13 mm diameter 2% thoriated tungsten. Copper wire is wrapped around the ends of the filament to provide solid contact. 30 gauge magnet wire is used to connect the filament to electrical leads exiting the probe. Figure 33 shows the miniature emissive probe used in the in-channel measurements. The probe is mounted to the HARP for internal measurements.

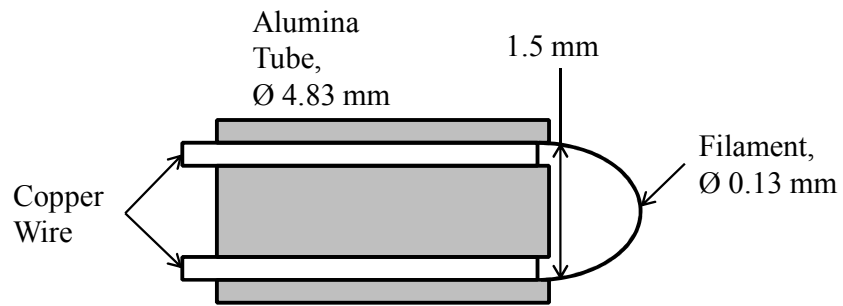


Figure 32. Miniature emissive probe schematic.



Figure 33. Miniature emissive probe.

3.4 Summary

This chapter presented the facilities and diagnostics used in this dissertation. The operational theory, error, and design of probes were also discussed. The majority of the recognized error sources present in these diagnostics are systematic errors due to design or operation as opposed to random error. While the uncertainty may be large in some situations, the trends and relations between data are still valid.

CHAPTER 4

INITIAL DESIGN: STAINLESS STEEL SURFACE ELECTRODES

This chapter presents the magnetic field design, and initial experimental results for the ion focusing research. The magnetic field of a HET is a key part of the performance of these thrusters. With the biased electrodes, the magnetic field needed to be redesigned to incorporate shielding cusp fields to reduce electron current to the electrodes. The design of the magnetic field also controls the potential contours within the channel, something called the thermalized potential which is discussed in this chapter. The initial electrode design used stainless steel (SS) bands that are welded into a ring for placement on the surface of the channel for ease of integration into the existing thruster. The thruster performance is measured on krypton propellant.

4.1 Magnetic Field Design

The electrodes in this work are biased above anode potential in order to repel ions. The high potential will make the electrodes attract electron. The collection of plasma electrons by the electrodes would result in an additional power sink which would reduce gains in the T/P ratio. Thus, it is necessary to shield the electrodes with cusp-shaped magnetic fields to magnetize electrons and reduce their mobility toward the electrodes. The magnetic field of the T-220HT is redesigned to incorporate magnetic shielding around the electrodes. This is performed with the commercial software MagNet by Infolytica, a finite element magnetic field modeling code.

The effect of the magnetic field topography within the discharge channel has been studied extensively in the past [20, 24, 71]. The majority of the past research into HETs

has been focused on magnetic field design. The literature has concluded a few guidelines for B field design to provide efficient thruster operation. These are: a symmetric field along centerline, a flat plasma lens near the exit, a low radial magnetic field at the anode, and a $B_{r,\text{wall}}/B_{r,\text{center}}$ ratio greater than 1 inside the channel. These known characteristics of a good field design are kept in mind during the field redesign of the T-220HT. In addition to known characteristics, the redesign also needed to incorporate a cusp-shaped field around the electrode locations. These parameters and the final design are described in more detail in the following section.

4.1.1 Magnetic Field Design Characteristics

A symmetric magnetic field along the channel centerline is necessary to help contain the discharge plasma. A skewed or unsymmetrical field would cause the plasma to strike one channel surface with increased frequency. This can cause ion losses and increased channel erosion. The plasma lens describes the predominantly radial magnetic field structure near the exit of the discharge channel where the field strength is the strongest. The plasma lens should be flat to reduce electric field divergence. The plasma lens is roughly the location off the electron cloud due to the high magnetic field providing strong electron trapping and reducing cross-field electron mobility. The effective cross-field electron mobility $\mu_{e\perp}$, can be defined as,

$$\mu_{e\perp} = \frac{\mu_e}{1 + \Omega_e^2}$$

Equation 4-1

Where μ_e is the electron mobility and Ω_e is the electron Hall parameter defined as follows.

$$\mu_e = \frac{e}{mv_m}$$

Equation 4-2

$$\Omega_e = \frac{\omega_c}{v_m}$$

Equation 4-3

Here e and m are the electron charge and mass respectively and ω_c is the electron gyro frequency defined as,

$$\omega_c = \frac{eB}{m}$$

Equation 4-4

and v_m is the momentum-transferring collision frequency which is the sum of the electron-ion collision frequency, ν_{ei} , and electron-neutral collision frequency, ν_{en} . The Hall parameter is the ratio of the gyro frequency of the particles with the collision frequency. A large Hall parameter, $\gg 1$, means the particle is magnetized and makes multiple orbits around a magnetic field line before a collision with neutrals or ions occur. Electrons are magnetized at the high B field locations near the plasma lens making the electron Hall parameter much larger than unity. This causes the cross-field mobility to become very small.

Reduced electron mobility increases the density near region of high magnetic field. The high electron density increases the chance of collisions with neutral atoms, which increases the ionization rate. The HET typically has a high ionization rate over 90%. Electrons that collide with other particles will jump to weaker field lines and slowly move toward the anode as the magnetic field decreases in strength towards the anode. The decrease in B field is also important as electrons need to reach the anode in order to complete the electrical circuit between the anode and cathode.

The requirement for a low radial B field at the anode is also related to the need for a complete electrical circuit between anode and cathode. The magnetic field in a HET channel is designed to trap electrons on radial fields as stated previously. The field strength is highest at the channel exit and decreases upstream until it reaches a point of zero field strength. Then the field changes direction and begins to increase in magnitude, but with the opposite sign. As electrons travel from high to low fields, their cross-field mobility increases due to weakening B fields and larger gyroradii. The electron is able to slide down the decreasing B field toward the anode. The opposite, moving up an increasing B field is difficult and requires higher energy. If the zero field point is far in front of the anode, the electrons will be impeded in crossing the strengthening B field to reach the anode. This situation will cause the electron temperature, thus electron velocity, to increase in order to preserve the electron circuit. This results in a loss of efficiency as extra power is needed to maintain thruster operation without a reciprocal gain in performance. Ideally, the magnetic field should be designed to have the zero point behind the anode, so there is no mirror effect. If that is not possible, then placing the zero point close to the anode ensures low field strength and thus minimizes the effects.

The requirement for a wall to center B_r ratio greater than one is to ensure the plasma is confined near the center of the channel. At any axial location, a ratio below one would cause the plasma to exist predominately near the walls, which increases losses and erosion. Both situations are bad for thruster performance and operation, thus a high ratio is needed.

The final requirement for the magnet field redesign is the existence of strong cusp fields around the electrodes. The strength of the ring-cusp magnetic field around the

electrodes varies with distance from the wall. The minimum necessary strength of the ring-cusp magnetic fields is determined by the Larmor radius of the electrons in the crossed electric and magnetic field near the electrodes. Using Equation 1-5, a first order calculation for the Larmor radius can be computed. Velocity is assumed to be purely thermal. A near-wall electron temperature of 25 eV is assumed based upon electron temperature measurements made by Haas on a 5-kW HET. [11]

To achieve a 1-mm Larmor radius in this configuration requires a 95 G magnetic field. The magnetic field simulation gives a field of 110 G at a location 5 mm from the electrode, and the field increases in strength closer to the wall. The cusp-field is large enough to magnetize the majority of the electrons and thereby shield the electrodes. It should be noted that the magnetic field created is highly two dimensional and concave over a large portion of the channel area. Standard HET magnetic fields maintain a predominantly radial field. The concavity of the magnetic field will help the electric field lines to focus toward centerline by is an untested design.

4.1.2 Final Magnetic Field Design

Figure 34 shows the redesigned magnetic field as well as the locations of a second set of magnets added to generate and strengthen the cusp-magnetic fields. These are denoted as inner ring-cusp coil (IRC) and outer ring-cusp coil (ORC). The electrode locations are also shown for comparison. The new magnetic field has a flat plasma lens near the exit plane, is predominately symmetric until the anode, and provides cusp magnetic field shielding of the electrodes. The wall to centerline B_r ratio varies from 1.1 to 2.3 in the channel depending on location, but remains above 1 throughout the channel. The radial field changes direction just downstream of the anode, and forms one half of a

magnetic mirror. However, the radial strength at the anode is on the order of -20 G at the highest magnet current levels, which will only affect the lowest energy electrons, thus will have minor if any detrimental effects. From measurements provided by Pratt & Whitney of the original magnetic field of the T-220HT, the radial field at the anode is on the order of -10 G at the same current levels, very close to the redesigned field.

Physical measurements of the centerline radial magnetic field with a radial Gauss probe match the simulated centerline radial profile except at the anode and exit. The simulated anode radial field is 11 G smaller than the measured field, and the exit plane radial field is 46 G (24%) larger than the measured field. The discrepancy is attributed to machining tolerances, Gauss probe accuracy, and probe position accuracy. Physical magnetic mapping of the channel magnetic field is performed with a radial and axial Gauss probe to confirm the field shapes. The magnetic field physical measurements and simulations match within 5%. Figure 35 plots the centerline radial magnetic field from simulations for the original PWR T-220HT configuration and the new redesigned field. The two fields align well, though the redesigned field has slightly higher maximum radial peak and is shifted downstream.

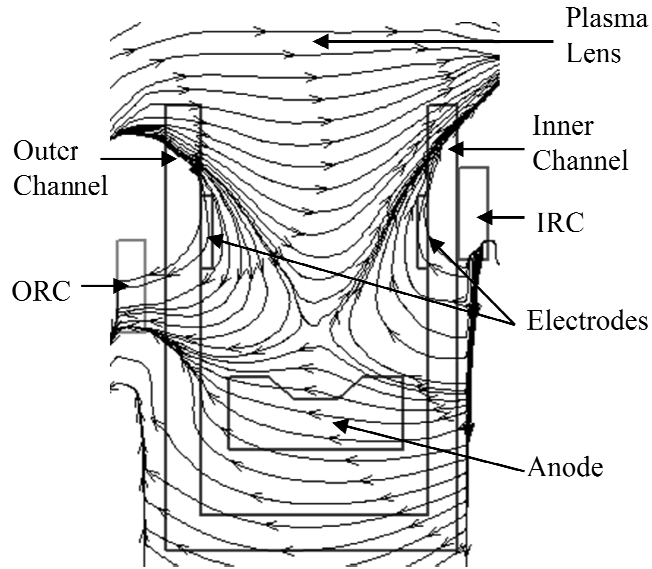


Figure 34. The redesigned magnetic field for this dissertation. The field meets the historical metrics of good B field design, and incorporates cusp-shaped fields covering the electrodes.

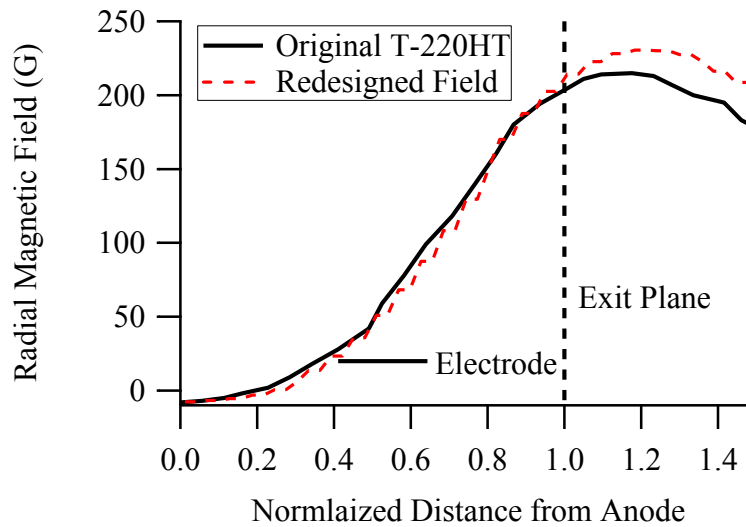


Figure 35. Centerline radial magnetic field for original T-220HT and redesigned field from simulations. The redesigned centerline radial strength matches closely to the original field, thus the electron motion should be similar.

4.2 Electrodes

The electrodes used in the initial design are made of 304 stainless steel. Steel stock 0.05 in. thick is cut into 0.4 in. wide strips and spot welded to form rings

conforming to the diameter of the inner and outer discharge channel. Small threaded rods are spot welded to the electrode surfaces. Figure 36 shows pictures of the outer and inner SS electrodes after manufacturing. Matching holes are drilled in the back of the channel to allow the rods to pass through and electrical connections to be made. Alumina tubes are used to cover the rods and insulate them from the plasma and anode. The electrodes are placed a set distance into the discharge channel across from each other.



Figure 36. The stainless steel outer (left), and inner electrodes (right). The electrodes are made from strips of steel and curved to the proper diameter. Steel threaded rods are welded for electrical connections.

The stiffness of the steel resulted in a non-uniform curvature of the bands. This caused the electrodes to sit above the channel surface at locations. On average the bands protruded 0.1 inches into the channel. Figure 37 shows the T-220HT with the SS electrodes added. The electrodes are electrical connected to the anode power line as shown in Figure 38. This setup means the electrode is biased to the anode potential when connected. Additionally, the electrode power supply only needs to provide 10-30 volts to result in a potential higher than the anode. An RC filter is placed in line with the discharge power supply to provide oscillation damping. The primary goal of the initial design is to determine the feasibility of operating the thruster with the new B field and if T/P ratio improvement with electrodes is possible.

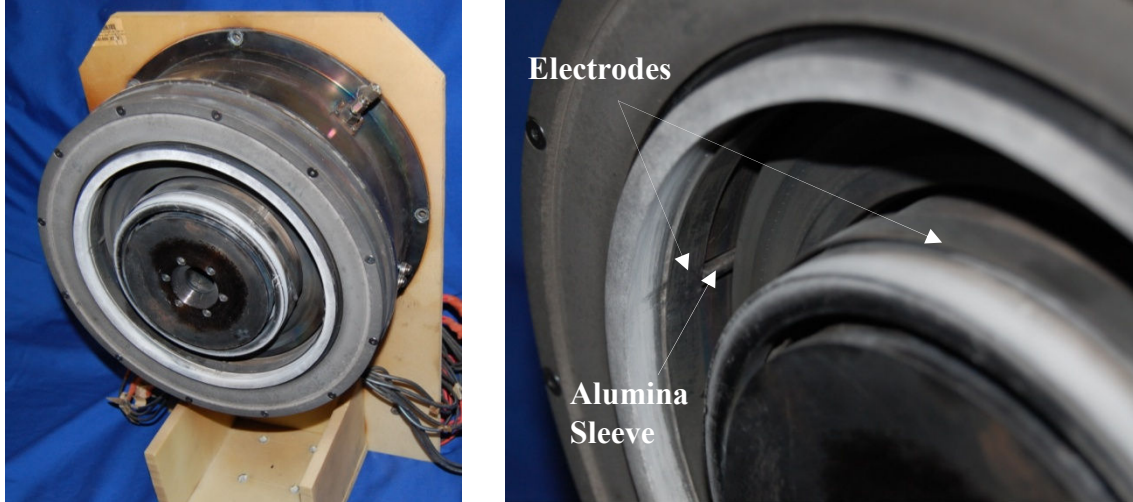


Figure 37. T-220HT with stainless steel electrodes. Grooves are made in the channel material for the threaded rods to allow the electrodes to slide as close to the surface as possible.

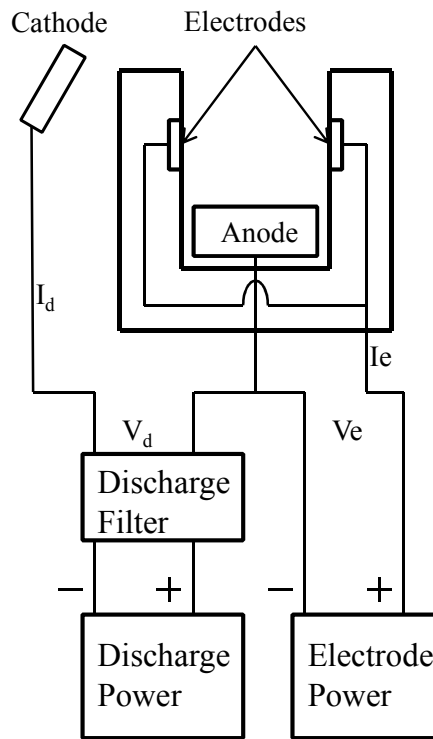


Figure 38. Electrical schematic for the thruster showing connection to anode power line. The electrodes are connected to be biased on the anode voltage.

4.2.1 Electrode Placement

The location of the electrodes will affect their effectiveness. There are three main considerations: cusp-magnetic field placement, Hall current shorting, and wall ion

density. The requirement to shield the electrodes with the cusp fields means they must be placed upstream of the channel exit where the magnetic field needs to be largely radial and with high strength. A high B_r at the channel exit is crucial for proper HET operation as mentioned previously. The second factor that contributes to an upstream placement of the electrodes is the presence of the electron Hall current near the magnetic field peak. The Hall current is comprised of the high energy cathode electrons that cause ionization of propellant. A biased electrode, especially a positive one, placed within the Hall current would collect the electron and effectively short the Hall current. This would prevent the thruster from operating when the electrodes are biased.

These two factors determine an upstream placement of the electrodes away from the channel exit. The last consideration, the ion wall density, actually says the opposite. This work is interested in reducing ion-wall collisions, thus it is logical to place the electrodes in areas with high wall collisions. The majority of wall collisions occur near the exit plane of the thruster where the electric field begins to diverge. This behavior has been seen in both models[13] and experiments[59]. Shastry calculated the ion density at the channel wall using wall-mounted Langmuir probes and compared it to simulations using the code HPHall-2. Both results showed the density peaks around $0.15 L_C$ from the exit plane, where L_C is the channel length from the exit plane to the anode, and drops quickly to zero past $0.5 L_C$. [59] This would suggest the electrodes should be placed at $0.15 L_C$. However this location would cause the cusp-magnetic fields to interfere with the plasma lens structure near the exit. The simulation of the channel centerline electric field in Figure 39 shows that the leading edge of the electrode strongly decides the electric potential. After multiple iterations, it was decided to place the electrode at $0.5 L_C$. This

placement avoids deformation of the exit plasma lens due to the shield cusp-magnetic fields, and the electric fields from the electrodes should be able to affect the start of the ion wall collision region.

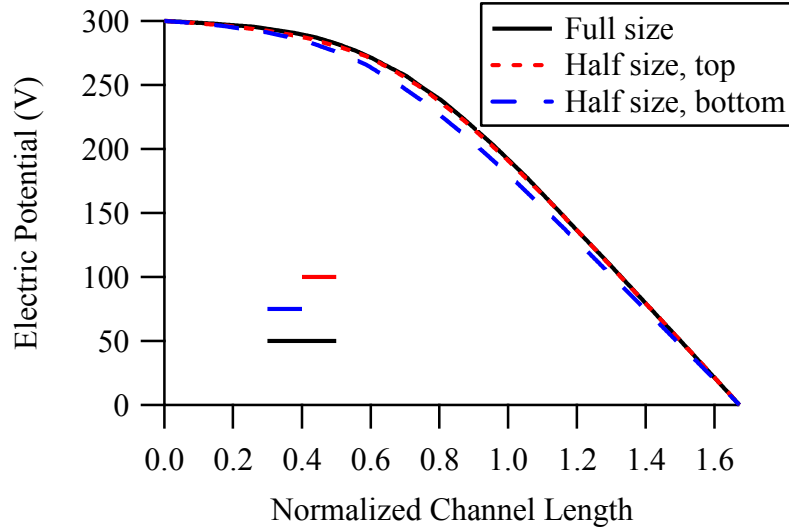


Figure 39. Simulation of channel centerline electric potential for the full sized electrode (0.4 in) and two half sized electrodes (0.2 in) at the top and bottom of the same area.

4.3 Thermalized Plasma Potential

One of the major effects of the magnetic field, and one reason its design has been studied so much in past research is the thermalized potential. As discussed in the previous section, the cross field electron transport is small; however the transport along magnetic field lines is largely unimpeded. The magnetic field lines trap electron of similar energies. Electrons determine the local potential, thus magnetic field lines become equipotential lines. This is called the thermalized potential. Thermalized potential can be defined as,

$$\varphi_{th} = \varphi_p - \frac{k_B T_e}{e} \ln \left(\frac{n_e}{n_0} \right)$$

Equation 4-5

where ϕ_p is the plasma potential, k is the Boltzmann constant, T_e is the electron temperature, e is the electron charge, n_e is the electron density, and n_0 is the reference electron density at a reference plasma potential [72].

The thermalized potential assumption holds when the electron density variation across a field line is low. Due to the high mobility along field lines, the density variations are small. Thus, it can be assumed the thermalized potential is constant along a magnetic field line. The magnetic field lines are equipotentials within kT_e/e order of accuracy. The low-density variation and thermalized potential occurs when the electron temperature is low and uniform along a field line. In HETs this is generally only true in the near anode or plume regions. Near the exit where the Hall current is and the electron temperature is high, the equipotential lines deviate from the magnetic field lines. Nonetheless, this relation between magnetic field lines and equipotentials helps design the magnetic field to alter ion trajectories as electric fields are perpendicular to equipotentials.

4.4 Ionization and Recombination

The stated goal of this work is to increase HET performance by reducing ion losses, specifically ion-wall neutralization. It is thus prudent to consider the various ion sources and sinks present in HETs to determine the percentage of total ions lost to wall neutralization. There are two primary sources of ion losses, wall and particle collisions. Both will be described and their contributions to the total ion population analyzed.

4.4.1 Ionization

The ionization process in HETs is purely collisional. Electrons emitted from the cathode obtain energy from the electric field and collide with neutral atoms to create ions. The production rate of ions is given by the rate equation

$$\frac{dn_i}{dt} = n_n n_e \langle \sigma_i v_e \rangle$$

Equation 4-6

where n_i and n_n are the ion and neutral particle densities respectively, σ_i the ionization cross-section, and v_e the electron velocity. The term in the brackets is the ionization reaction rate constant, which is the ionization cross-section averaged over the electron velocity distribution function. The values for the ionization rate constant have been tabulated for multiple temperatures. Goebel [33] presents tabulated xenon ionization constants for electron temperatures up to 10 eV, and curve fits for larger values of T_e . His calculations are used here. A graph of the ionization constant over a range of electron temperatures above 5 eV is shown in Figure 40. The constant increase is linear after 30 eV.

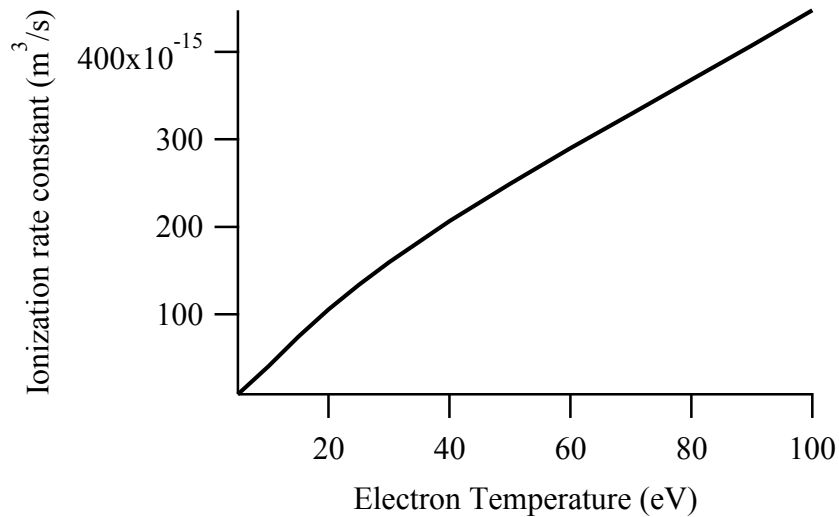


Figure 40. Xenon ionization rate constant from Goebel[33] for 5 - 100 eV. There is little ionization below the xenon first ionization energy of 12 eV.

The electron number density, which from the quasi-neutral assumption is equal to the ion number density, can be calculated from the ion beam exiting the thruster from

$$n_e = \frac{I_b}{ev_b A_c} = \frac{\eta_b I_d}{e A_c \sqrt{\frac{2\eta_b e V_d}{M}}}$$

Equation 4-7

where I_b is the measured ion beam current, e is the electron charge, A_c is the channel area, η_b is the beam efficiency which is equal to the beam current divided by discharge current (I_b/I_d), and M is the ion mass (2.18×10^{-25} kg for xenon). The measured beam current, presented later, varies from 6.9 to 8.2 A for a 9 A discharge current on the anode. The difference between the ion current exiting the thruster and the electrical discharge current seen by the anode is due to ion losses and the electron leakage current.

The discharge current consists of two primary sets of electrons: ionization electrons and cathode electrons. The dominant source of the discharge current comes from the ionization of propellant where the electrons removed from the neutral atoms are collected by the anode. Cathode electrons that slowly make their way across the magnetic field to the anode also make a small contribution to the discharge current. The cathode electrons are caught on the strong magnetic field, but every collision causes the electrons to lose energy and jump to a weaker magnetic field and eventually reached the anode. This is called the leakage current. Thus only a portion of the discharge current is from ions.

Taking an average I_b of 7.6 A for an I_d of 9 A at a discharge voltage of 200 V yields an electron number density of $1.6 \times 10^{17} \text{ m}^{-3}$. This is on the low end of the in-channel measured and simulated electron density from the literature, but sufficient for our purposes.[11, 13, 73, 74] It is interesting to note that Equation 4-7 has very little variation

in the electron density with the three variables: discharge current, discharge voltage, and beam efficiency. There is a linear variation due to beam current, I_d , if voltage and beam efficiency are held constant. However HETs typically operate over small current ranges, say 10 – 30 A, thus the effect of current on density is small.

The effects of voltage and beam efficiency are even smaller as shown in Figure 41 and Figure 42. The graphs show that the electron density is a relatively stable quantity over a large range for both variables. Both only increase the density by a maximum of 3.16 times, if the other parameters are held constant. In reality the voltage, current, and beam efficiency are tied together. Assuming a constant propellant supply, increased voltage creates more energetic electrons with energy approximately $1/10^{\text{th}}$ the voltage, which results in higher beam current and higher beam efficiency. The three variables will thus tend to cancel one another and make the overall change in electron density even smaller. This can also be seen from measured data of in-channel plasma density.[11, 51, 73] The point of this discussion is to show the plasma density is a rather stable value in HETs for a large range of operating conditions.

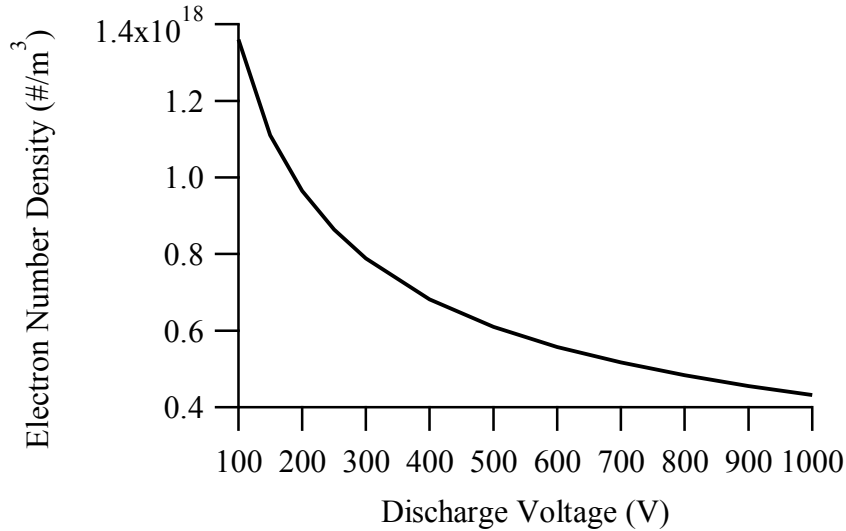


Figure 41. The calculated electron density as a function of the discharge voltage for a constant 50 A current, and beam efficiency of 1. The maximum change in density is 3.16 times from low to high voltage.

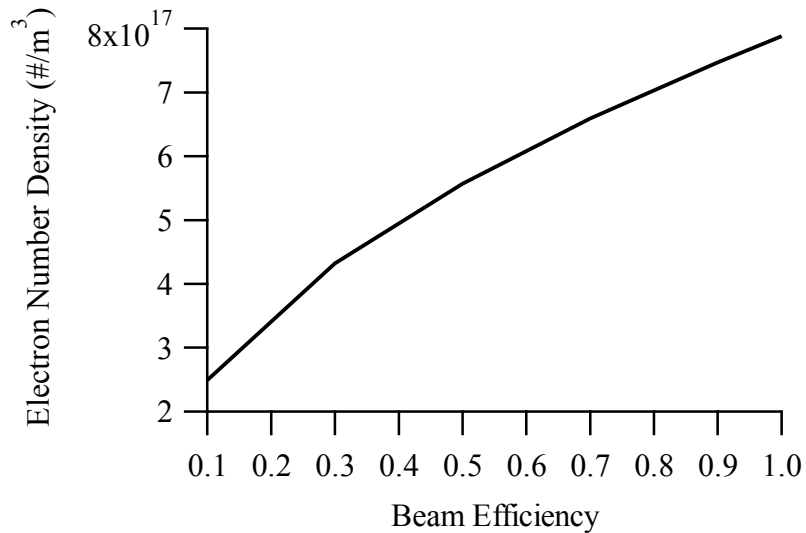


Figure 42. Electron density for the range of beam efficiencies at constant 300 V and 50 A discharge. There is a maximum of 3.16 times increase in electron density from perfect to low beam efficiency.

The neutral density is typically two orders of magnitude larger than the plasma density, so will be taken as $1 \times 10^{19} \text{ m}^{-3}$. [51, 73, 75] The electron temperature in the ionization region is usually on the order of 20 eV or more. A value of 25 eV will be assumed for this analysis. This falls within the range measured for this thruster as shown in Section 7.3. The resulting ion production rate constant is thus $2.14 \times 10^{23} \text{ m}^{-3} \text{ s}^{-1}$.

The ionization process occurs within a relatively small volume of the discharge channel upstream of the magnetic field peak.[33, 51, 73] This axial distance is on the order of the characteristic ionization mean free path (MFP) λ_i .

$$\lambda_i = \frac{v_n}{n_e \langle \sigma_i v_e \rangle}$$

Equation 4-8

Here v_n is the neutral particle velocity which can be calculated from the mean 3-D thermal velocity,

$$v_n = v_{th} = \sqrt{\frac{8k_b T_n}{\pi m_n}}$$

Equation 4-9

where k_b is the Boltzmann constant, T_n is the neutral particle temperature, and m_n the neutral mass. The neutral temperature can vary greatly depending on operating conditions. Huang measured the neutral temperature inside a HET channel with laser-induced fluorescence and showed the temperature can vary from 600 – 1600 K.[76] The operating conditions in this work correspond to an average of 800 K based on his results. This gives a neutral velocity of 357.5 m/s. The resulting ionization MFP is thus 1.67 mm. Multiplying by the channel area, the total ion production rate is $6.76 \times 10^{19} \text{ s}^{-1}$, which is an ion current of 10.8 A. This is larger than the assumed beam or discharge current, but acceptable for this analysis.

Combining Equation 4-6 thru 4-9, one can calculate the ion current from ionization as shown in Equation 4-10. This ion current is independent of the electron

density and the electron temperature. The combined current equation only depends on the neutral temperature and density.

$$\begin{aligned}
 I_i &= eA_c \frac{dn_i}{dt} \lambda_i = eA_c (n_n n_e \langle \sigma_i v_e \rangle) \left(\frac{v_n}{n_e \langle \sigma_i v_e \rangle} \right) \\
 &= eA_c n_n v_n = eA_c n_n \sqrt{\frac{8k_b T}{\pi m}}
 \end{aligned}$$

Equation 4-10

Equation 4-10 makes sense since an increased ionization rate means a decreased ionization MFP, with a net result being a small increase in ion production. An increase in the neutral density means increased propellant flow rate and thus increased current. A larger channel area can also cause increased ion current, assuming the propellant flow rate is increased to maintain the neutral density. So for high ion current, a large thruster with high flow rate is desirable.

4.4.2 Electron-Ion Recombination

Electron-ion recombination will decrease the number of ions available for thrust, if the ions recombine prior to exiting the thruster. So for concerns of net thrust loss due to electron-ion recombination, only the ionization and acceleration regions need to be considered. The electron-ion recombination rate equation (assuming electrons are the dominant third-body) is

$$\frac{dn_i}{dt} = -k_r n_e^2 n_i = -\alpha n_e n_i$$

Equation 4-11

where k_r is the recombination rate constant, which can be calculated as α from [77]

$$\alpha = 1.09 \times 10^{-20} n_e T^{-\frac{9}{2}} \text{ m}^3/\text{s}.$$

Equation 4-12

Using the density and temperature values from the previous section, the electron-ion recombination rate constant is $1.17 \times 10^7 \text{ m}^{-3}\text{s}^{-1}$. The acceleration region has a length of 3 – 5 mm as shown in Section 7.2. Taking an average length of 4 mm, combined with the ionization mean free path and channel area gives the ions lost to electron recombination as $1.26 \times 10^4 \text{ s}^{-1}$, which is a current of $2 \times 10^{-15} \text{ A}$. This is a miniscule amount of ions lost compared to the 10.8 A of ions produced. The recombination current is strongly dependent on plasma density and electron temperature. However even trying to maximize the recombination with a very low temperature of 5 eV and high density of $5 \times 10^{19} \text{ m}^{-3}$, the recombination current is only $6 \times 10^{-5} \text{ A}$; thus electron-ion recombination has a negligible impact on thruster performance.

4.4.3 Wall Losses

Ion-wall losses result from ion collisions with the channel wall. The quasi-neutral property of the plasma means on a macroscopic level, the plasma is free of electric fields, thus any ions that reach the wall are due to random thermal motions. At the wall, a thin plasma sheath region exists where quasi-neutrality breaks down and electric fields can exist. The sheath exists due to the different fluxes between electrons and ions. The ratio of electron to ion current flux, assuming quasi-neutrality, is

$$\frac{J_e}{J_i} = \frac{n_e e v_e}{n_i e v_i} = \frac{v_e}{v_i}$$

Equation 4-13

where J is the current density, e is the charge on the particle, and v is the particle velocity. The i and e subscripts correspond to ions and electrons respectively. The average 1-D particle thermal velocity is

$$v_{th} = \sqrt{\frac{2k_b T}{\pi m}}$$

Equation 4-14

If the ion and electron temperatures are assumed equal, then the current density ratio is proportional to the square root of the mass ratio.

$$\frac{J_e}{J_i} = \frac{v_e}{v_i} = \sqrt{\frac{m_i}{m_e}}$$

Equation 4-15

Ions are much heavier than electrons, for example the square root of the mass ratio for xenon is 491. This means the electron flux is much larger, and electrons will strike the wall before ions. This causes the wall potential to decrease and become negatively charged, which attracts ions and repels electrons. This decreases the electron flux to the surface. The wall potential and sheath stabilizes when the ion and electron flux at the sheath edge are equal. Inside the sheath, the potential decreases from the plasma potential to the wall potential. The sheath potential drop accelerates ions in the sheath toward the wall. The ion flux to the wall can thus be assumed equal to the ion density at the sheath edge if the sheath is assumed collisionless.

The plasma density at the sheath edge is 60.6% of the plasma density in the plasma far away from the sheath. This arises from the Bohm sheath criterion, which states that in order to have a monotonically decreasing potential in the sheath, ions must

fall through a potential of at least $T_e/2$ before entering the sheath. This expression can be written as

$$\Phi_o > \frac{k_b T_e}{2e}$$

Equation 4-16

where Φ_o is the potential drop. This condition can be expressed in terms of a velocity from the electric to kinetic energy balance $e\Phi = 1/2 mv^2$:

$$v_i = \sqrt{\frac{2e\Phi}{m_i}}$$

Equation 4-17

The resulting velocity

$$v_i \geq \sqrt{\frac{k_b T_e}{m_i}}$$

Equation 4-18

is known as the Bohm velocity, or ion acoustic velocity when entering a sheath.

Combining Equation 4-16 with the Boltzmann equation for electrons,

$$n_e = n_o \exp\left(\frac{e\Phi_o}{k_b T_e}\right)$$

Equation 4-19

where n_o is the plasma density far away from the sheath, gives

$$\begin{aligned} n_e &= n_o \exp\left[\left(\frac{e}{k_b T_e}\right)\left(\frac{-k_b T_e}{2e}\right)\right] \\ &= 0.606n_o . \end{aligned}$$

Equation 4-20

The negative sign in Equation 4-20 comes from the potential drop from the bulk plasma to the sheath edge. Knowing the plasma density, and thus ion density at the sheath edge, it is possible calculate a value for the current loss to the wall. The assumption made here is all ions that enter the sheath strike the wall and become neutralized. This is a valid assumption as the sheath is very thin, typically less than 1 mm, and the potential profile within the sheath causes ion acceleration toward the surface. Thus, the sheath ion current density can be written as

$$J_i = 0.6n_o e v_i = 0.6n_o e \sqrt{\frac{k_b T_e}{m_i}}.$$

Equation 4-21

Equation 4-21 can also be written in terms of a sheath current, I_S , for a sheath area A .

$$I_S = 0.6n_o e A \sqrt{\frac{k_b T_e}{m_i}}$$

Equation 4-22

Using the plasma density of $1.6 \times 10^{17} \text{ m}^{-3}$ calculated in section 4.4.1, and half the channel surface area for the reasons mentioned in Section 4.2.1 (there are no ions in the near anode region), the ion current lost to the walls is estimated to be 1.37 A. This is almost 13% of the total produced ion current, which means reducing this loss of ions to the walls could provide a significant increase in the thruster performance.

It should be mentioned that the surface area assumed here is based on the assumption of no ions at the wall upstream of $0.5 L_C$. This assumption was based on data of another thruster, the H6 from the University of Michigan.[59] The H6 and the T-220HT are similar in size, power, and design, thus the correlation is made with a

reasonable level of confidence. In general, the location of wall ions is dictated by factors such as the placement of the ionization zone and magnetic field, which will be different for different thrusters. Another method to define the beginning of the ionization region, and thus the beginning of the wall loss region, is to consider the location of the 12 eV electron temperature contour. The first ionization energy of xenon is 12.13 eV, and thus the 12 eV contour can be assumed as the start of the ionization region. As will be shown later in Section 7.3, the 12 eV contour in this work roughly corresponds to half the channel length, thus the half surface area approximation used above is reasonable.

The expression for ions lost to the wall can be simplified by combining the result of Equation 4-10 and Equation 4-22:

$$\begin{aligned} \frac{I_S}{I_i} &= \frac{n_o e A \sqrt{\frac{k_b T_e}{m_i}}}{e A_c n_n \sqrt{\frac{8 k_b T_n}{\pi m_n}}} = \frac{0.6 n_o A}{n_n A_c} \sqrt{\frac{\pi T_e}{8 T_n}} \\ &= 0.626 \frac{n_o A}{n_n A_c} \sqrt{\frac{T_e}{T_n}} \end{aligned}$$

Equation 4-23

Here, the neutral mass is taken to be equal to the ion mass. The neutral density is generally two orders of magnitude larger than the plasma density as mentioned in Section 4.4.1, thus the ratio n_o/n_n is around 0.01 – 0.02. The square root of the temperature ratio also tends to stay relatively constant around 10 – 12. This is because a higher electron temperature causes heating of the anode and channel walls, which subsequently heats the neutral propellant. Without external cooling, the neutral temperature should track the electron temperature relatively well. Thus, the only major factor in the fraction of ions

lost to the walls is the dimensions of the thruster channel. The term A/A_c can be broken down into considerations of channel length and diameter.

$$\begin{aligned}\frac{A}{A_c} &= \frac{\pi L_c}{2} (OD + ID) \bigg/ \frac{\pi}{4} (OD^2 - ID^2) \\ &= 2L_c \frac{OD + ID}{OD^2 - ID^2} \\ &= \frac{2L_c}{OD - ID} = \frac{2L_c}{D_r - 1}\end{aligned}$$

Equation 4-24

Here OD and ID refer to the outer and inner diameter of the discharge channel, and D_r is the ratio of outer to inner wall diameter. The channel surface area is taken as half the total surface area as done previously. Combining this with Equation 4-23 and replacing the density and temperature ratios with constants 0.015 and 11 respectively gives:

$$\frac{I_s}{I_i} = 0.224 \frac{L_c}{D_r - 1}$$

Equation 4-25

This suggests that the fraction of ions lost to the wall can be reduced by designing thrusters with shorter channels and larger channel area. The latter occurs because an increase in outer diameter or decrease in inner diameter causes the channel exit area to increase faster than the surface area. Thus ion production increases faster than wall losses. Using the dimensions for the T220-HT, Equation 4-25 under predicts the percent ion-wall losses by 20% compared to the loss calculated using actual plasma properties. It

is useful, however, as an approximation for wall losses. A more thorough analysis of the particle interactions, such as how neutral temperature scales with electron temperature, or how neutral density relates to ionization rate and channel dimension, would give a more accurate prediction of ion-wall loss.

Many assumptions were made for this analysis. The actual physics inside the thruster are more complicated than these equations reflect. Nonetheless, the results show that ion-wall neutralizations are a significant portion of the total ions produced, and much greater than ions lost through electron-ion recombination.

4.5 Experimental Results

Figure 43 shows the modified T-220HT HET with stainless steel electrodes. The thruster is tested in VTF-1. All thrust measurements are taken with the null-type inverted pendulum thrust stand in VTF-1. The thruster operation conditions such as voltage and currents are recorded from meters located in the control room. Performance parameters such T/P ratio, I_{sp} and efficiency are derived from the measured thrust and power using Equation 4-26 to 4-8.

$$\frac{T}{P_{tot}} = \frac{T}{P_D + P_E} = \frac{T}{V_D I_D + V_E I_E}$$

Equation 4-26

$$I_{SP} = \frac{T}{\dot{m}_{tot} g_0}$$

Equation 4-27

$$\eta = \frac{1/2 T^2}{\dot{m}_{tot} P_{tot}}$$

Equation 4-28

Here T is thrust, P is power, the D, E, and tot subscripts denote discharge, electrode, and the sum of the two respectively. \dot{m}_{tot} is the total mass flow rate (anode and cathode), and g_0 is acceleration of gravity.

The performance of the thruster was measured over a discharge voltage range of 125-300 V at discharge currents of 9 A and 20 A on krypton propellant. Xenon is the standard propellant for EP, but krypton is used for the initial tests due to its lower operational cost. The thruster was run in constant current mode where the anode mass flow rate varied to maintain the current. This choice was made, instead of running in constant mass flow, in order to run at a set discharge power at a given discharge voltage. This choice makes comparison of the various electrode conditions easier and reduces the number of variables in the experiment. For example, 200 V_d will always run at 1.8 kW for each electrode voltage tested. HETs are typically run in constant power mode on satellites as well.

The magnetic field was kept constant through all tests in this work. This is contrary to standard HET operations where magnetic are optimized for minimum discharge current at each operating condition. The fields are kept constant throughout this work because the magnetic field topology is a crucial part of the design. Varying the magnetic field off design caused the field to shift left or right, unshielding the electrodes. Keeping a constant magnetic field also reduces the number of variables in the analysis.

Figure 43 shows the T-220HT thruster during testing. The effect of ion focusing is first investigated at 9 A. A discharge current of 20 A should result in larger performance improvements with biased electrodes due to increased number of ions. With more ions, a

larger portion of them will have large radial velocities that can be focused toward channel centerline.



Figure 43. T-220HT with stainless steel electrodes running on krypton.

4.5.1 Steel Electrode Performance

The performance of the thruster is measured over a discharge voltage range of 125-300 V at a discharge current of 9 A and 125 – 225 V at 20 A on krypton. The mass flow is held constant for all voltage settings. The setup allows the discharge current to change freely with the electrode voltage. This generally resulted in an increase in discharge current with electrode voltage. Figure 45 shows the measured thrust, total T/P ratio, I_{sp} , and anode efficiency of the thruster in this configuration. The calculations of T/P ratio and anode efficiency include the additional power due to the electrodes. The error bars shown on the graphs are the maximum uncertainty for all data.

The data shows four data sets for the various electrode voltages tested. The “Floating” data set has electrical connections from the electrodes removed at the power supply so the electrodes can float in the plasma. The 10, 20, and 30 V_e cases have the electrodes biased above anode potential by the stated voltage. Figure 44 and Figure 45

shows an increase in thrust as the electrode voltage increases. The increase is larger at lower discharge voltages. The T/P ratio however shows a general decrease with applied electrode voltage. This drop in T/P ratio is due to the additional electrode power offsetting the gain in thrust, which results in a lower T/P ratio than in the Floating case without biased electrodes. If electrode power is not considered, the T/P ratio increases with electrode voltage, but that would not give a realistic picture of the performance. The I_{sp} and anode efficiency both show increases at low voltages and a decrease or no change at higher voltages. The change in performance with the electrodes is quite small, and often within the range of the uncertainty.

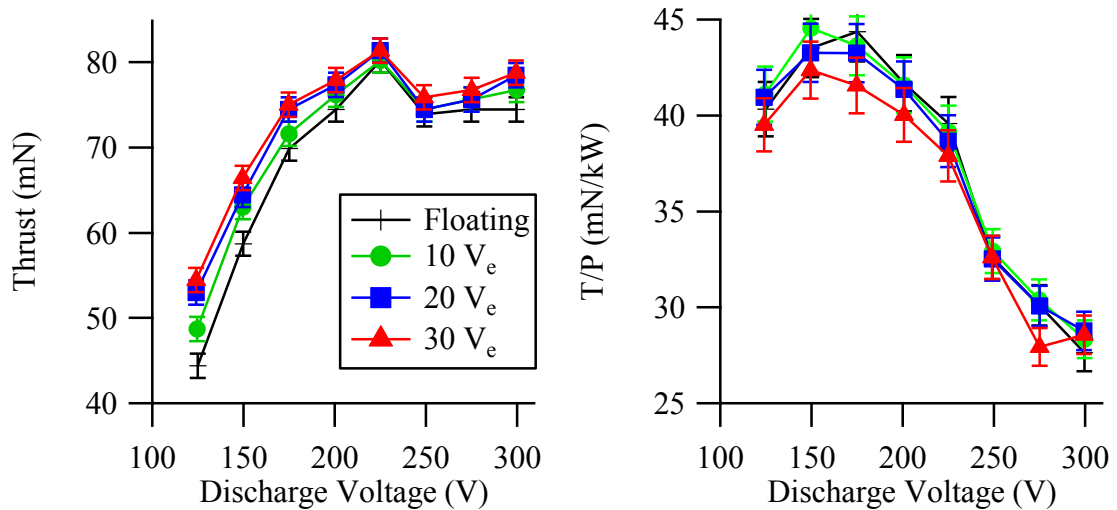


Figure 44. Stainless steel electrode performance at 9 A on krypton with 0-30 V electrodes. Electrodes cause increase in thrust, but decrease in T/P ratio.

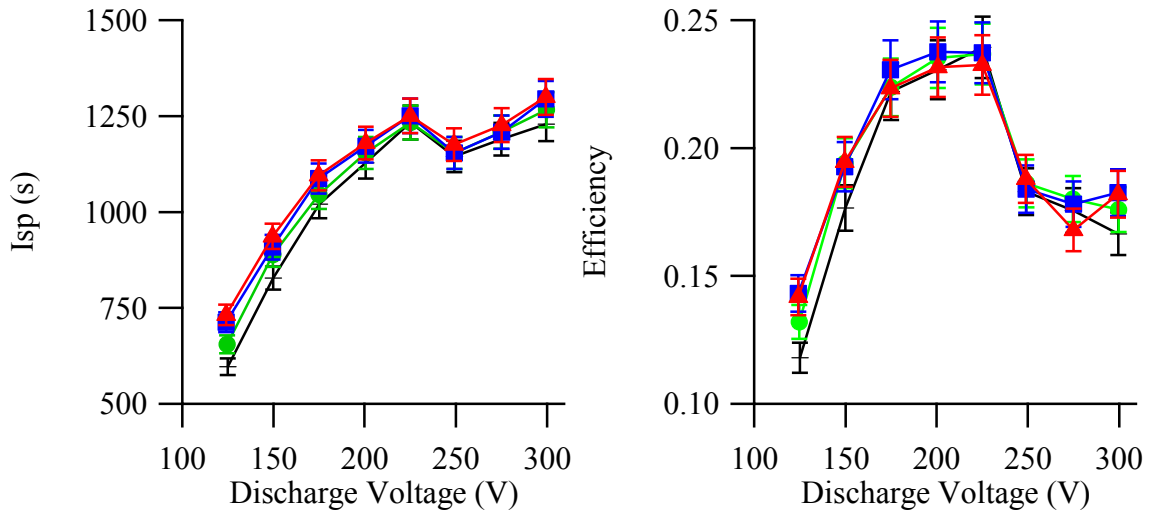


Figure 45. Stainless steel electrode performance at 9 A on krypton with 0-30 V electrodes. Electrodes cause increase in I_{sp} and efficiency.

Figure 46 shows the thruster at 20 A discharge current for Floating and 10 V_e cases. The electrodes are only tested at 10 V due to abnormally high current loads at higher voltages risking thermal damage. The thrust, T/P ratio, I_{sp} , and efficiency improvement with electrodes is higher at 20 A than 9 A. This seems to confirm the idea that biased electrodes generate larger performance improvements at higher discharge currents. The larger number of ions generated at high currents means more ions are repelled from the wall and focused toward channel centerline, which generates more thrust than at lower currents.

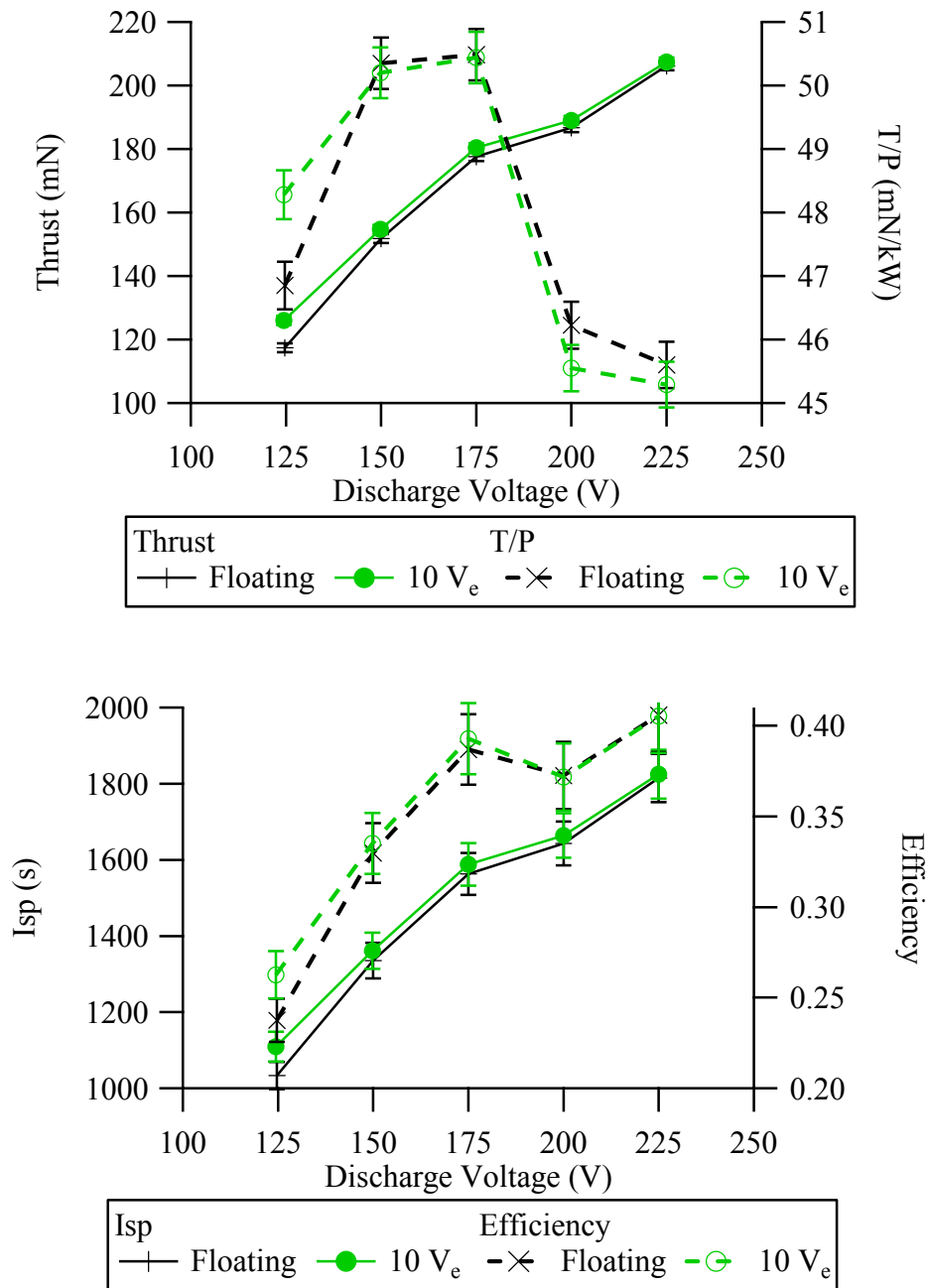


Figure 46. Stainless steel electrode performance at 20 A on krypton with 0 V and 10 V electrodes. The performance improvements are higher at 20 A than 9 A.

The calculated data shown here are comprised of T/P ratio I_{sp} , and anode efficiency. The measured quantities are thrust, discharge voltage, discharge current, and anode mass flow. The thrust stand data has an accuracy of ± 1.4 mN, the mass flow,

voltage, and current measurements all have accuracies of $\pm 0.1\%$. Mean squared error analysis yields maximum error of: T/P ratio $\pm 3.5\%$, I_{sp} $\pm 3.6\%$, and efficiency $\pm 5\%$. The accuracy of the electrode current measurements presented later is ± 100 mA.

4.6 Results and Discussion

In all of the data sets, there is a consistent increase in thrust, I_{sp} , and efficiency at low voltages with electrodes. The increase in thrust at low voltages indicates that the electrodes enhance the ability of the thruster to create a collimated ion plume. Whether this is through ion focusing or some other effect, such as a two-stage operation, or increased ion acceleration, cannot be determined from the performance data alone. However, the fact that improvements only exist at low voltages runs contrary to previous work on two-stage HETs, which indicates improvements primarily at high voltages [16, 24]. This suggests that the electrodes do not function as a second stage. The work done by Raitses with unshielded electrodes shows little to no performance improvement in the voltage range of 170 to 300 V, which again suggests that the changes seen here are not the result of two-stage operation.[22].

An important plasma property to consider is the plasma sheath that exists around the electrodes. The sheath is a thin layer of charged particles, on the order of 5-10 Debye lengths, that exist at the interface between the plasma and any surface. The sheath exists to shield out or neutralize the presence of the surface and any electrical fields from the bulk plasma. The sheath develops due to the different thermal velocities of electrons and ions. Electrons have much higher thermal velocities owing to their lower mass. Thus, they will strike a surface first and negatively charge it. Ions are attracted by the negative surface. The ion flux and electron flux balance and forms a thin layer near the surface.

Inside the sheath exists a local electric field caused by the charge imbalance, while outside the sheath the plasma only sees the quasi-neutral sheath boundary, thus is unaware of the surface.

The plasma sheath around the electrodes is on the order of 0.8 mm. This would mean the electrodes can only affect a small portion of ions due to the shielding aspect of the sheath. Thus, the electrodes should have little effect on thruster performance. Yet, noticeable changes in thrust are measured. The presence of the ring-cusp magnetic fields that shield the electrodes does complicate the analysis. The ring-cusp magnetic fields greatly retard the motion of electrons that move perpendicular to the magnetic field, which prevents a thin electron sheath from forming around the electrode and can extend the distance the electric field penetrates into the plasma. Ions are depleted in the sheath due to the electric field from the electrodes and are too heavy to be affected by the ring-cusp fields. Therefore, the calculated value of 0.8 mm sheath thickness is likely incorrect. Anders [78] and Keidar [79] show that a parallel magnetic field along a positively-biased wall extends the plasma sheath farther away from the wall for field strengths of at least a few hundred Gauss. The ring-cusp magnetic fields around the electrodes in this study are 100 – 300 G. Thus, the sheath and the electric field probably extend significantly more than 0.8 mm into the discharge plasma. How far the field penetrates is not known.

Assume for a moment the electrodes are able to affect the entire width of the channel, it will then change the local electric field and the overall potential profile. Fruchtman modeled a similar setup of an HET with in-channel electrodes and showed that the addition of a biased electrode can cause a sonic transition and an increase in thruster efficiency [6]. That work differs in that his electrode is biased slightly below

anode potential, to create a two step potential profile for a two-stage thruster. Electrons in the anode-electrode region would have slower velocities, thus increasing number density and ionization. In this work, since the electrodes are at a higher potential than the anode, the potential profile would have a peaked shape. The electric potential is highest at the electrode location and decreases toward both cathode and anode. Electrons moving toward the anode are accelerated by the potential between cathode and electrode, but then slowed by the lower potential anode. This can increase the electron number density in the region between anode and electrode, thus increasing ionization in that region in the same manner as Fruchtman's work.

For ions however, any created between the anode and electrode region would preferentially move toward the anode due to its lower potential. This suggests that ions created in this region may be neutralized by the anode and result in a loss factor. This is likely a small effect if any since the electrodes increase as opposed to decrease performance.

Another phenomenon common to all the data sets is the improvements caused by the electrode decreases as discharge voltage increases. This decrease is reasonable, because at high voltages a smaller fraction of the energy is needed for ionization, thus more is available for acceleration compared to low voltages where there is much less energy for acceleration [80]. This decrease in acceleration energy results in lower energy ions at low voltages and higher energy ions at high voltages relative to the discharge voltage. If we assume an acceleration voltage of 200 V, and an ion divergence angle of 30 degrees off centerline, the resultant maximum radial energy would be 100 V. Any electrode voltage below 100 V would be unable to fully focus these ions. At high

voltages the electrodes at 30 V_e will repel and turn ions with a 100 V radial energy to a small degree. In contrast, for a lower acceleration voltage of 90 V, with the same divergence angle of 30 degrees, the maximum radial energy is 45 V. Thus, the 30 V_e electrodes will repel and focus ions to a large degree at this operating condition. The varying amount of radial energy is likely why there is a larger improvement in thrust at low discharge voltages only.

The electrode current during these tests provides an idea of the electron behavior within the channel relative to the biased electrodes. Figure 47 shows the electrode current for the 9 A discharge condition on krypton. The electrode current increases as the electrode voltage increases. This is because as the electrode voltage increases, the electron attraction to the electrode is stronger, which results in a higher electrode current despite the same electron trapping field. As the discharge voltage increases, the reduced electrode current suggests either the anode absorbs a greater portion of the electron current, or the beam current is a larger fraction of total current. The former is more likely. As the discharge voltage increases, the additional voltage on the electrodes, 10-30 V, becomes a smaller fraction of the anode voltage. For example, 30 V electrodes at 100 V anode voltage results in the electrodes having a 30% higher potential as the electrodes are biased above anode potential, however if anode potential is 300 V, the same electrode only has a 10% higher potential. The additional voltage from the electrode is a smaller fraction of the total voltage so electrons are less likely to be attracted to the electrodes.

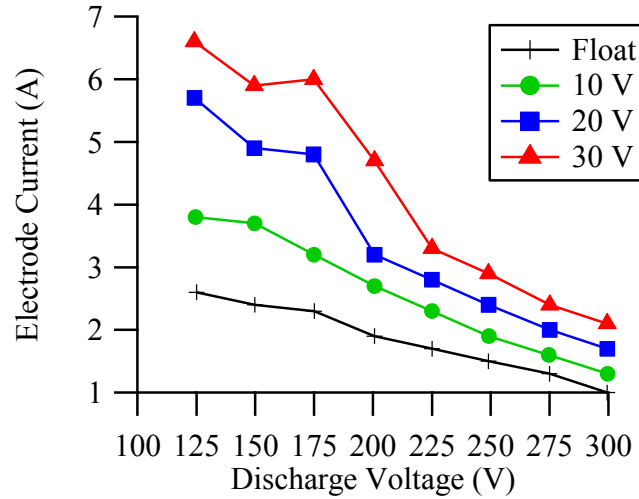


Figure 47. Electrode current at 9 A on krypton for thick electrodes with 0-30 V electrodes. The decreasing electrode current with increasing discharge voltage suggests anode absorbing increasing electron current.

4.7 Summary

To achieve the goal of repelling ions from the channel wall to reduce ion-wall neutralizations, stainless steel electrodes are added along the channel wall of a T-220HT (HET). A magnetic field redesign is required to generate shielding cusp magnetic fields around the electrode locations. The cusp fields would magnetize electrons and reduce the power draw by the electrodes. The final magnetic field incorporated the historical characteristics of a good HET magnetic field along with high strength cusp fields.

The thruster is operated with the new magnetic field and steel electrodes at constant mass flow rate and various voltages. The electrodes show increased performance at low discharge voltages across all four metrics of thrust, T/P ratio, I_{SP} , and efficiency. The electrodes are more effective at the higher current of 20 A than at 9 A. Without plume data, it is not possible to determine how the electrodes affected the ion population. The fact the electrodes primarily functioned at low discharge voltages is contrary to previous work with two-stage HETs, thus another behavior is likely occurring here. The

initial work showed that the electrodes can increase performance, but the changes are small.

CHAPTER 5

FINAL DESIGN: EMBEDDED ELECTRODE ON KRYPTON

The previous sections show the viability of the in-channel electrodes to improve HET performance. There are definite increases in thrust, I_{SP} , and efficiency. The T/P ratio showed a small increase at certain conditions. Plasma diagnostics were not performed with the initial design. It is believed changes to the design could improve the electrode performance and make electrode effects more apparent in plasma measurements. The steel electrode bands would also have made in-channel diagnostics difficult due to their protrusion into the channel area. Using lessons learned from the first round of tests, a redesign is done to embed the electrodes within the channel wall to increase performance and allow for in-channel diagnostics. The resultant thruster is designated the Embedded Electrode Hall Effect Thruster (EEHET). This chapter discusses the EEHET redesign, the performance and plume measurements, as well as some internal plasma potential measurements on krypton. The goal is to compare the embedded electrode performance with the steel electrodes and determine the possible effects of introducing graphite into the dielectric channel.

5.1 Electrode Redesign

The initial tests with the steel electrodes showed that small performance improvements are possible, but the physical presence of the electrodes is likely a detriment to the thruster. To improve performance, a smooth channel wall is deemed necessary. To that end, a new discharge channel was built with electrodes embedded within the channel wall itself. The embedded thruster was tested at the same conditions to

allow side by side comparisons as well as new conditions allowable by the new electrodes. The channel is the exact same design, but a portion of the channel walls are removed to allow the addition of electrode rings. Boron nitride rings of the same grade as the channel material make up the extra space. The channel has the same dimensions still. The embedded electrodes are made of isomolded graphite as opposed to steel. Graphite is a conductive material that can withstand higher thermal loads.

The electrode connections for power are run through the center of the thruster for the inner electrode (IE) and through the outside shell of the thruster for the outer electrode (OE). Tiny holes are drilled into the channel walls above where the electrodes rest. Similar holes are placed in the electrodes. Connecting wires run through the hole in the wall and are insert into the electrodes. Alumina tubes and ceramic paste provide insulation for the wire from the plasma. Each electrode is controlled by a separate power supply, unlike the initial tests when they are both controlled by a single power supply. This allows measurement of individual electrode currents.

Figure 49 shows a photograph of the new channel with graphite electrodes and BN spacer rings. The embedded nature of the electrodes should allow for improved performance, and easier diagnostics of the in-channel plasma. A combination of stainless steel clips and mica strips sandwiched between the rings and the channel held the electrodes and BN rings in place. The electrical connections for the electrodes and anode are the same as the initial steel electrode design as shown in Figure 38.

The thruster is run on 99.9995% pure krypton. All data for the EEHET was taken in VTF-2. A duplicate null-type inverted pendulum thrust stand is installed in VTF-2 and all thrust measurements are taken with it.

Graphite Electrodes

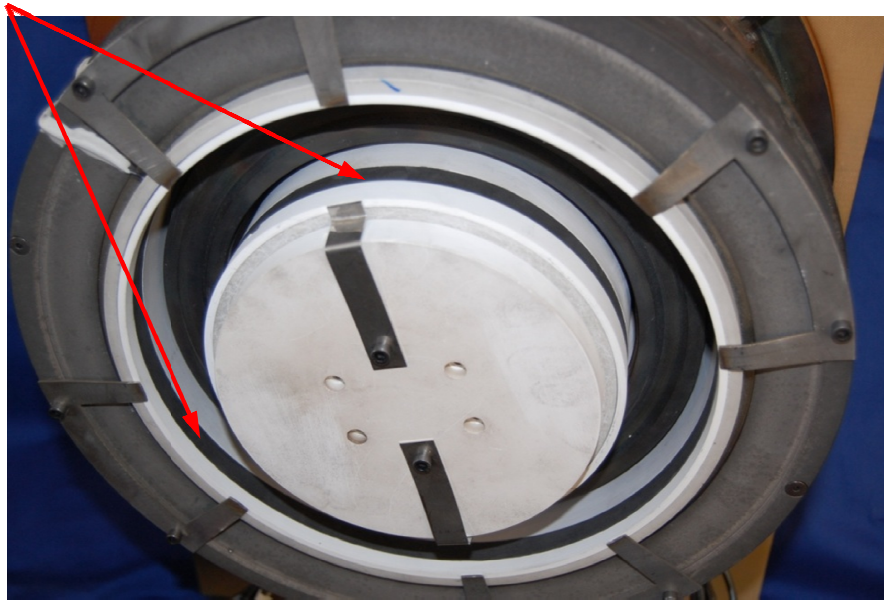


Figure 49. Embedded electrodes position in the discharge channel of the T-220HT. The steel clips around the edges were initially used to hold the rings in place.



Figure 50. EEHET post test. The white block on the right of the thruster (left side of picture) is a protective cover for the outer electrode wires.

5.2 Material Changes: Graphite versus BN

With the addition of graphite electrodes, the wall material of the discharge channel is now different. This may cause inherent changes in plasma behavior. The addition of different materials to the dielectric discharge channel of a SPT has been done before. Raitses *et. al* added rings made of graphite, quartz, and MACROR to the channel exit to change the plasma properties.[81] The introduction of different materials into the channel primarily affects the plasma through the secondary electron emission. A lower SEE can change the electron temperature, which affects the maximum electric field and the electron mobility across magnetic fields. TALs have higher electron temperatures and larger electric fields compared to SPTs due to its steel channel which has much lower SEE than BN.

Graphite has a lower SEE yield than BN.[81, 82] Raitses *et. al.* showed having graphite electrodes in the discharge channel will increase the electron temperature and electric field.[38] However, their measurements indicated changes to electron temperature and electric field are mainly at discharge voltages above 400 V. Below that voltage, the BN and graphite electron temperature and electric field are largely the same. This suggests that the graphite with the lower SEE may not have a large effect on the plasma in the EEHET as it is only tested up to 300 V.

5.2.1 Performance

Figure 51 - Figure 54 show the performance data for the BN and Floating electrode cases on krypton propellant. The thruster operated at a constant discharge current of 9 A for both cases. The magnet current is also held constant. In the BN case, the graphite electrodes are replaced with boron nitride rings to simulate a standard ceramic HET channel. The Floating case had graphite electrodes installed, but unplugged

and allowed to float to the local floating potential. The two cases have very similar performance, almost identical within the error. The data here was collected during two separate tests of the thruster, with physical changes made in between tests. Thus there may be environment factors inherent in the data due to the exposure of thruster to atmosphere between tests and slight differences in physical placement of electrodes. These results seem to substantiate the finding by Raitses that below 400 V, the SEE due to graphite has little to no effect on the thruster performance.

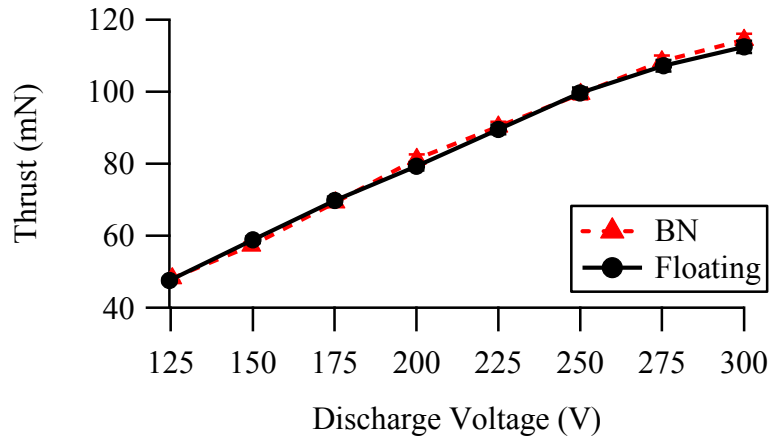


Figure 51. Thrust for BN and Floating electrode conditions on krypton at 9 A. The two cases have nearly identical thrust.

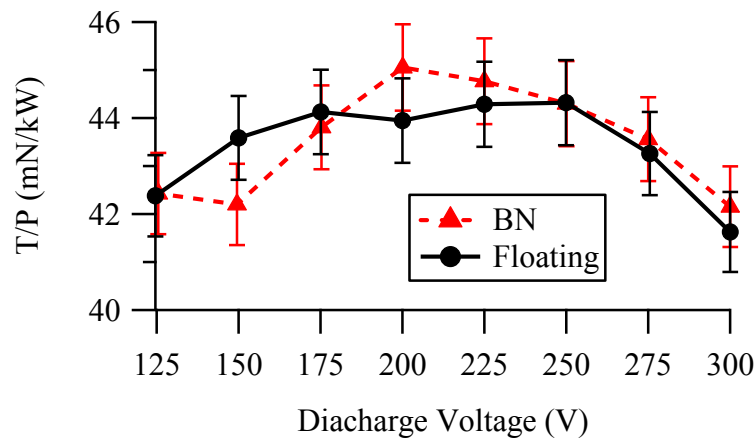


Figure 52. T/P ratio for BN and Floating electrode conditions on krypton at 9 A. The BN case exhibits slightly higher T/P ratio at a few locations due to differences in mass flow. The differences can be attributed to uncertainty in the measurements and changing environment conditions between tests.

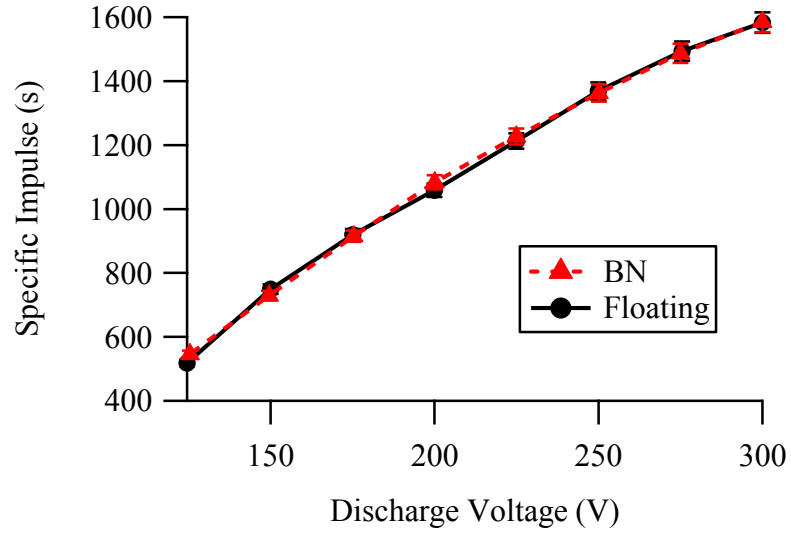


Figure 53. Specific impulse for BN and Floating electrode conditions on krypton at 9 A.

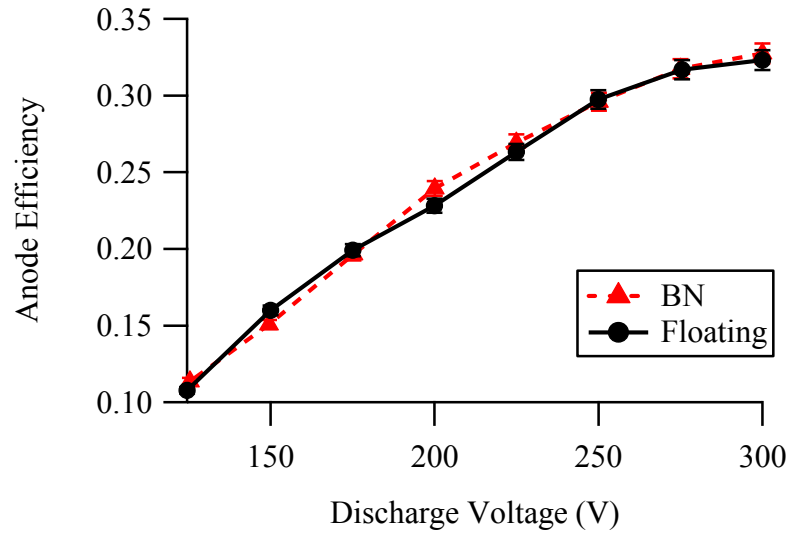


Figure 54. Anode efficiency for BN and Floating electrode conditions on krypton at 9 A.

The location of the graphite may be another factor to the lack of performance change. In the EEHET, the graphite electrodes are placed well upstream of the radial magnetic field peak, which exists near the channel exit as shown in Figure 35. The electron temperature is typically highest near the radial magnetic field peak at the channel exit and lowers upstream.[11, 51] This electrode placement means the electrodes see lower electron temperatures than if they are near the exit. The lower electron temperature

means a decrease in the SEE rate, so there is less of an effect due to the material change. Any reduction in SEE due to the graphite electrodes does not appear to influence the plasma in a major way.

The uncertainty in the performance measurements for the EEHET on krypton at 9 A is ± 1 mN for thrust, 1.8 % for T/P ratio 1.6 % for I_{SP} , and 2.3 % for efficiency.

5.2.2 Faraday Probe

Plume measurements are taken with the EEHET using the Faraday probe, RPA, and floating emissive probe. The emissive probe data is used to correct the RPA measurements. All three probes are mounted 1 meter downstream of the thruster channel exit plane. They are spaced 5 degrees apart and swept in a constant radius arc around the thruster centered above the channel exit. Figure 55 shows the three probes mounted inside the chamber. From left to right they are the RPA, Faraday probe, and emissive probe. Figure 56 shows a schematic of the swept area.



Figure 55. Plume probe setup.

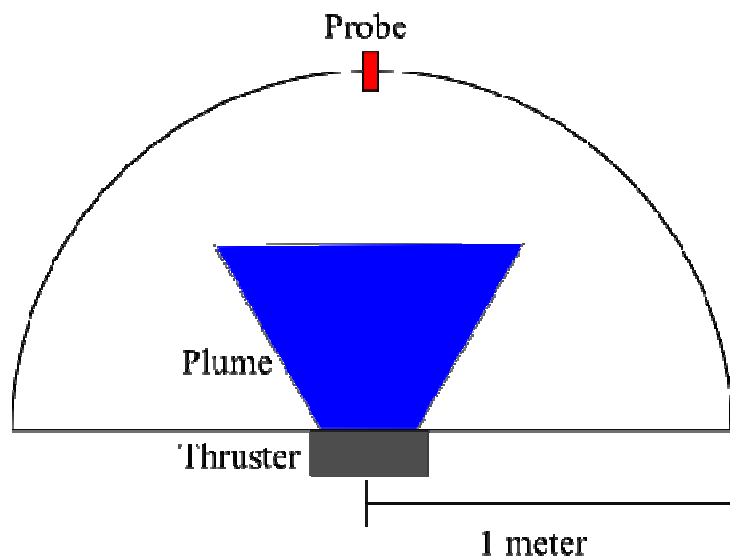


Figure 56. One meter thrust plume sweep for Faraday probe and RPA.

Figure 57 shows ion current densities at 300, 250, 200, and 150 V at 9 A on krypton for both the BN and Floating case. The profiles for the two cases appear nearly identical. The Floating case exhibits a slight increase in current density. The most noticeable change is seen at 150 V. Even at this voltage setting, the difference between the two cases is small. Additionally, the increase is a direct upward shift of the profile. The presence of the graphite is increasing the ion number density without affecting the potential and electrical fields. The scale of the profiles make direct analysis difficult, thus we will look at derived quantities.

Figure 58 shows the integrated total ion beam current for the cases in Figure 57. The Floating case has a noticeably higher beam current than the BN case. The discharge current is maintained at 9 A, thus the increased ion current signifies increased ion fraction of the total current. The ion beam current shows more clearly the change from BN to Floating, though the uncertainty makes the observed changes questionable. The beam

current increased by 0.63 A at 150 V where the most noticeable changes in the ion density profile are seen.

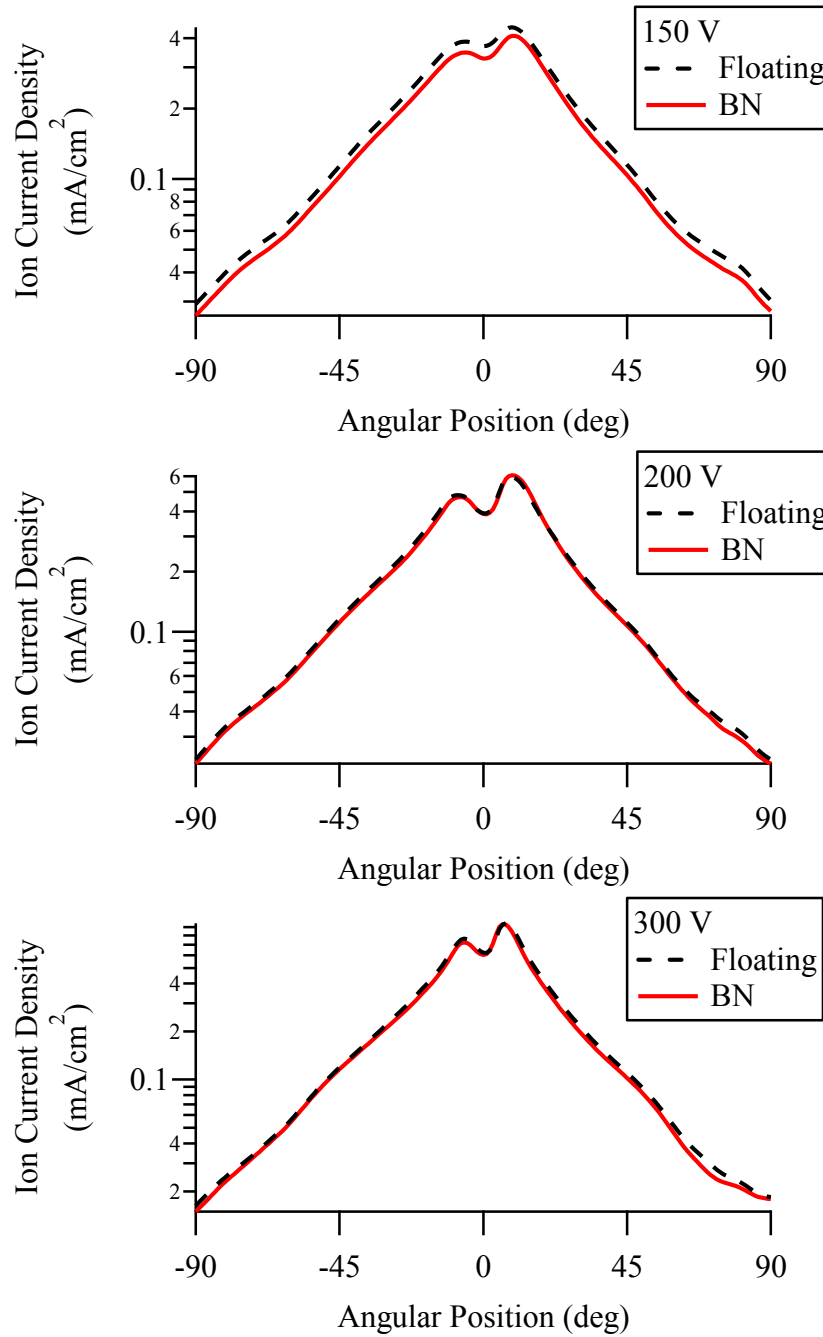


Figure 57. Ion current density for BN and Floating cases at 150 – 300 V_d and 9 A. Except at low voltages, the two cases have very similar ion density profiles.

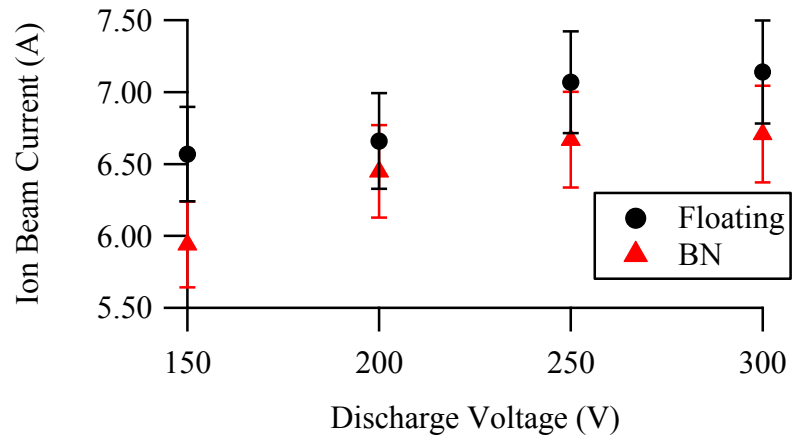


Figure 58. Integrated ion beam current for BN and Floating electrode at 9 A on krypton.

Figure 59 shows the calculated plume half angle. There is a slight increase in plume angle with the Floating electrode. The change is small compared to the increase in total beam current. This is due to a corresponding increase in the axial beam current with Floating electrodes. This means the thruster maintains the same ratio of ion divergence with the addition of graphite, even though the total beam current increases. This confirms the idea that more ions are produced, but without changing their trajectory.

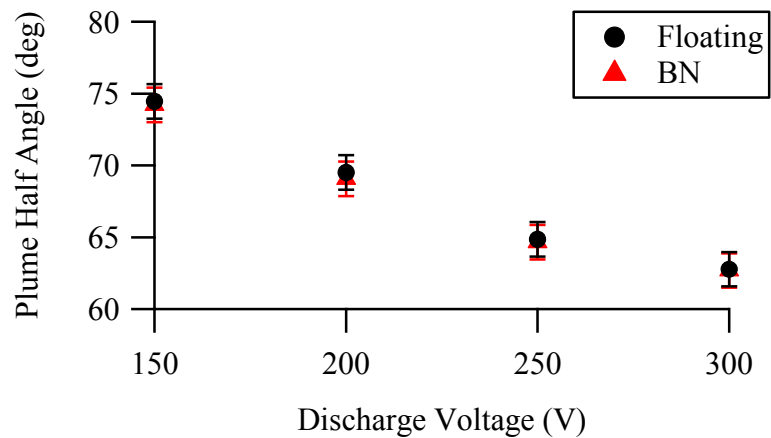


Figure 59. Plume divergence half angle for BN and Floating electrode cases on krypton.

5.2.3 RPA

Figure 60 shows two ion energy distribution functions for BN at 9 A on centerline at 150 and 300 V_d. The same Floating voltage case is also plotted for comparison. The two data sets are very similar, with the BN case having slightly higher ion energy. Figure 61 shows the most probable ion energy for all BN and Floating data. The Floating case exhibits slightly lower average ion energy across all discharge voltages, but the difference is small and within the uncertainty.

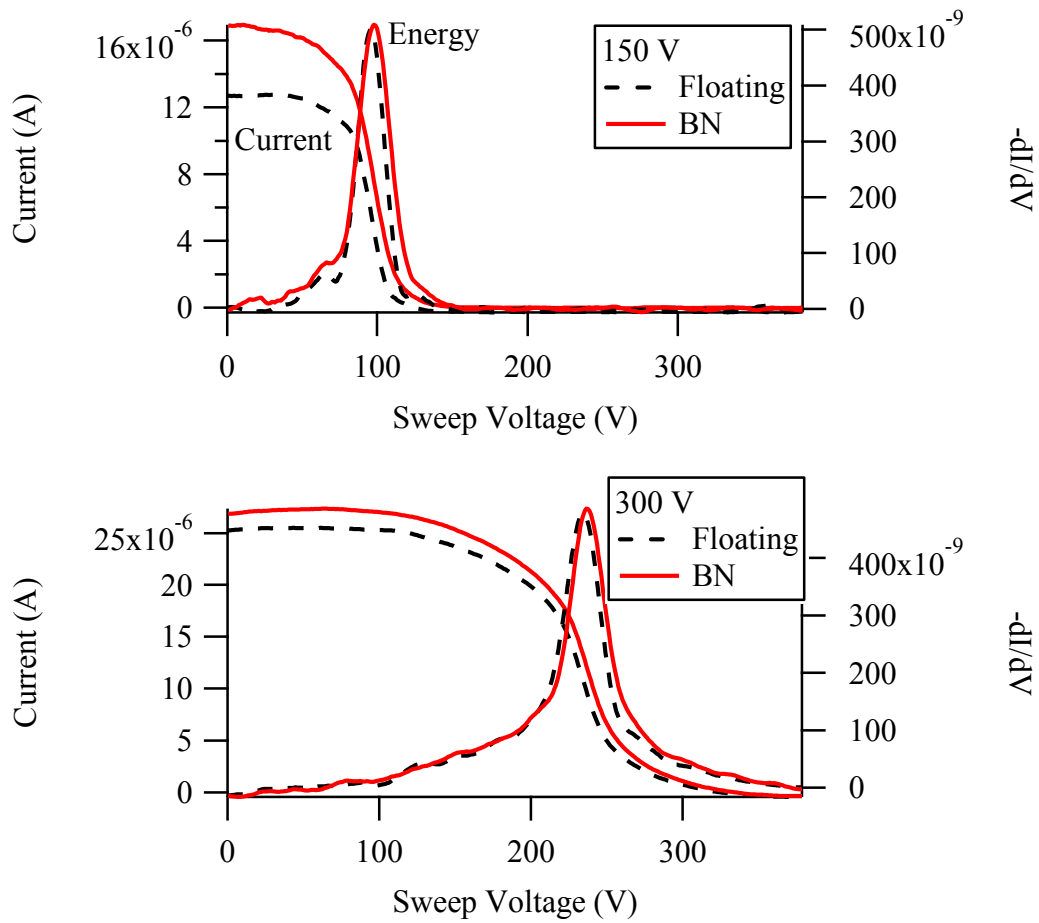


Figure 60. RPA ion energy distribution functions for BN and Floating electrode on channel centerline. There is very little difference in the energy of the ions with the presence of graphite.

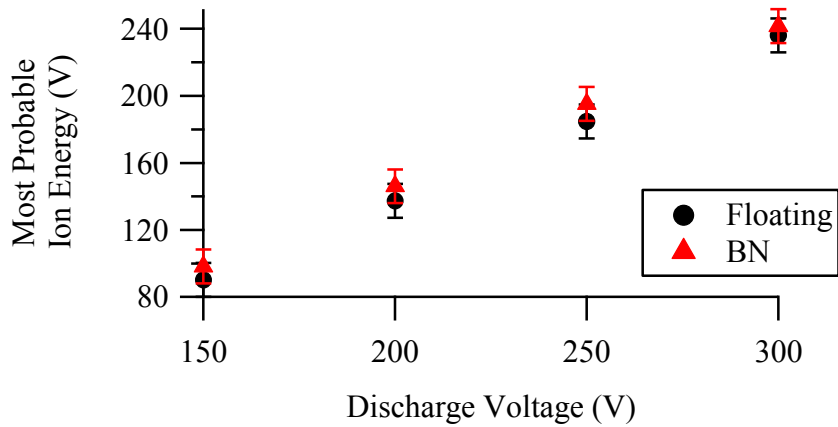


Figure 61. Most probable ion energy for BN and Floating electrode at 9 A on xenon. The BN case has slightly increased energy, but well within the uncertainty.

Figure 62 and Figure 63 show the propellant efficiency and total mass flow rate, respectively, for BN and Floating electrodes. Propellant efficiency is simply defined as measured ion beam current from the Faraday probe divided by the total mass flow rate as shown in Equation 5-1. The BN case has a slightly higher propellant efficiency because of its lower mass flow rate. This indicates the addition of graphite to the channel has a slight detrimental effect on the efficiency of ion production. Though again the changes are small and within the uncertainty.

$$\eta_p = \frac{I_b}{\dot{m}_{tot}} = \frac{I_b}{\dot{m}_{Anode} + \dot{m}_{Cathode}}$$

Equation 5-1

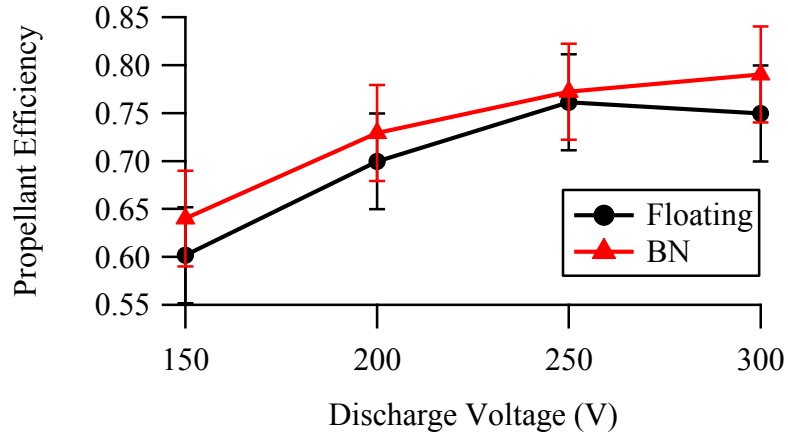


Figure 62. Propellant efficiency for BN and Floating electrode at 9 A on xenon. The Floating case has lower propellant efficiency even though the beam current was higher.

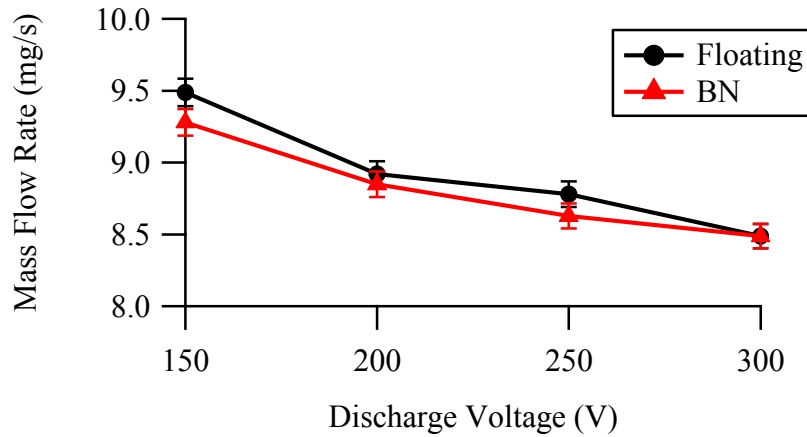


Figure 63. Total mass flow rate for BN and Floating electrode at 9 A on xenon. The Floating case required more propellant flow in order to maintain the same current, thus a lower propellant efficiency.

5.2.4 Internal Plasma Potential

Measurements of the plasma potential inside the discharge channel are taken with the miniature emissive probe shown in Figure 33. The probe is mounted on the HARP arm and aligned such that the plane of the filament loop is parallel to the channel wall and thus perpendicular to the magnetic fields. The thruster is mounted on the radial motion table for high precision movement as shown in Figure 30. The probe is swept a radial distance of 26 mm from the inner wall to the outer wall, leaving 2-3 mm of

clearance on either side for safety. The mapped area of the channel extends from 6 mm downstream of the anode to ~13 mm downstream of the exit plane covering a 50 mm length. The area is mapped in 5 mm axial steps and staggered radial steps decreasing in distance closer to the walls. Figure 64 shows the individual points mapped with the miniature emissive probe.

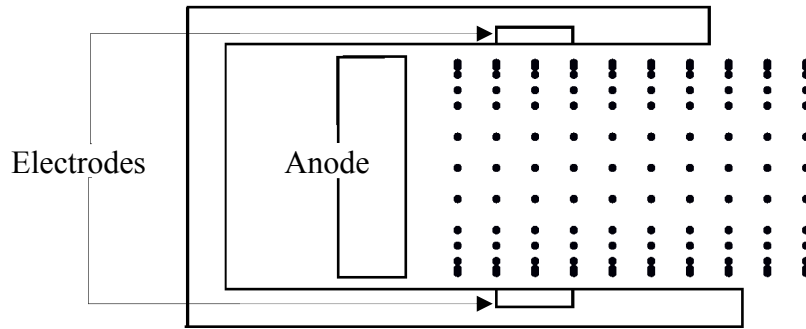


Figure 64. Mapped area of the discharge channel. Radial points are 4, 8, 10, 12, 13, and 13.5 mm on either side of centerline.

The miniature emissive probe is quite fragile due to the thin filament, and high electron temperature within the discharge channel. Due to these factors, the probe requires frequent replacement. 150 V_d was chosen as the test discharge voltage setting. Preliminary tests showed drastically reduced probe lifetimes at higher voltages. 150 V_d is also one of the voltages of interest as some of largest changes are observed there for the electrode cases.

Internal plasma potential measurements were made with both the BN ring and Floating electrodes. Figure 65 shows the potential contour map for these two cases. Indicated on the figure for clarity are the inner and outer channel walls, the anode, and the location of the BN/electrode rings. Both cases have nearly identical potential contours. The presence of the graphite electrodes does not appear to change the potential

and thus electric field to a noticeable degree as notes from the current density and ion energy profiles.

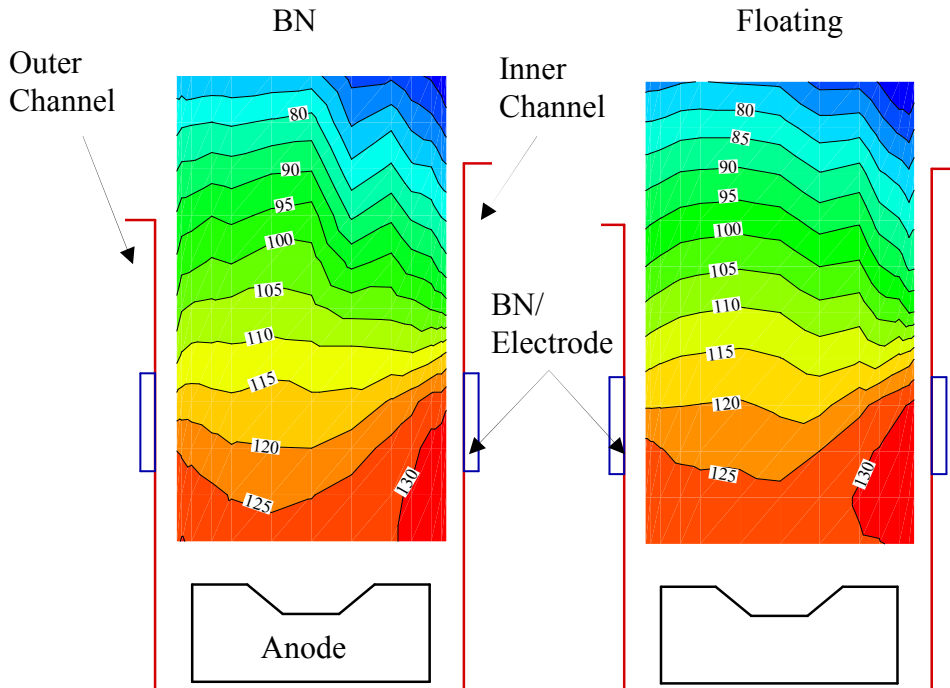


Figure 65. In-channel plasma potential contours for krypton at 150 V and 9 A for the BN (left) and Floating (right) cases. The two cases have nearly identical potential contours, with the Floating cases having slightly higher at any given location.

5.3 EEHET on Krypton

It was demonstrated the last section that the graphite material addition does not significantly change the plasma. Next, the EEHET is next tested on krypton from 125 – 300 V at 9 ± 0.05 A discharge with two electrode bias levels, 10 and 30 V_e . The cathode mass flow is maintained at 1 mg/s for all 9 A tests. The anode mass flow is varied from 8.65 to 11.5 mg/s krypton depending on operating condition in order to maintain constant discharge current. The magnetic fields settings are kept the same as previously. Magnet settings remained constant through all tests to provide the field topography shown in

Figure 34. This choice may have lead to some performance consequences, especially at high current levels which are discussed in later chapters.

The electrodes are tested at Floating, 10 V_e and 30 V_e , similar to the SS electrode test cases. The 20 V_e condition did not add much to the SS results and is omitted to reduce the test matrix size. The electrodes are electrically connected to the anode power line thus they share current with the main anode. Figure 66 shows the current collected by the electrodes during the tests. At 30 V_e , when the electrodes draw 6 – 8 A of current, the anode sees greatly reduced current. This large shift of current causes the electrodes to have a larger effect on the plasma than the primary anode. Indeed, the electrodes may act as the primary positive terminal for the thruster at certain points.

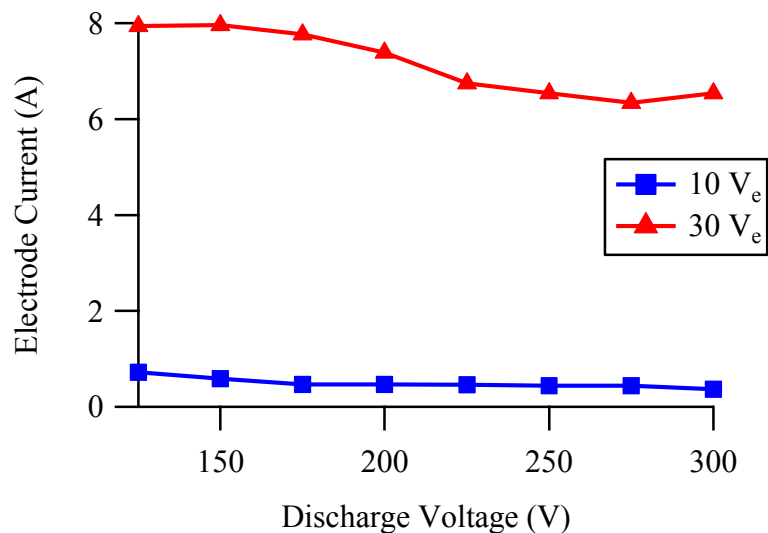


Figure 66. Electrode current for krypton at 9 A discharge current at 10 and 30 V_e . The 30 V_e case saw a large jump in the electrode current, pulling almost all discharge current from the anode.

5.3.1 Performance

Figure 67 - Figure 70 shows the thrust, T/P ratio I_{SP} , and efficiency for krypton at 9 A. Four sets of data are shown in each graph. These are the performance for Floating, 10 V_e , 30 V_e , and data from the SS electrodes. The SS data presented in each graph is

either the 10 or 30 V_e data, whichever had the greatest values. For example, the SS electrodes had larger thrust at 30 V_e , but larger T/P ratio at 10 V_e . This provides an easy way to see the changes from the best SS electrode results to the embedded electrodes.

The embedded electrodes greatly increase the performance of the thruster over the SS electrodes. In both thrust and T/P ratio the two electrodes have similar performance at 125 V_d , but as discharge voltage increases, the embedded electrodes perform much better. In specific impulse and efficiency however, the SS electrodes perform better or as well over a larger voltage range even though it had lower thrust. This high I_{sp} and efficiency is due to the lower mass flow required by the SS electrodes. The embedded electrodes required slightly more anode mass flow, an average of 1.87 mg/s. The largest cause of this increase in mass flow is the much lower chamber pressure between the SS electrode and the EEHET. The initial SS design is tested in VTF-1 with a base pressure of 1×10^{-5} Torr and average operating pressure of 2×10^{-5} Torr-Xe. The EEHET is tested in VTF-2 with a base pressure of 1.9×10^{-9} Torr and average operating pressure of 8.3×10^{-6} Torr-Xe, nearly an order of magnitude. It has been shown that high chamber pressure causes anomalous high thrust due to ingested chamber neutrals.

Comparing just the EEHET cases, thrust shows improvements with increased electrode bias. The values are larger than the uncertainty thus the results are valid. The increase in thrust results in a similar increase in the T/P ratio at 10 V_e , but a decrease at 30 V_e . This difference is caused by the electrode current differences between the two electrode voltages. The extra power at 30 V_e negates the thrust gain and reduces the T/P ratio. Specific impulse and efficiency follow similar trends as thrust and T/P ratio due to

the presence of the power term in the efficiency calculation. The EEHET does show a clear improvement in all four metrics with the biased electrodes.

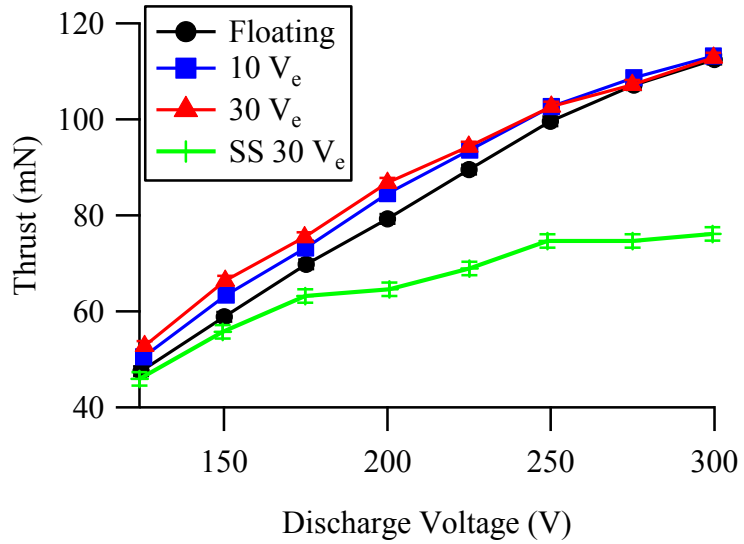


Figure 67. Thrust for EEHET on krypton at 9 A. Also shown in green is data from the stainless steel electrodes.

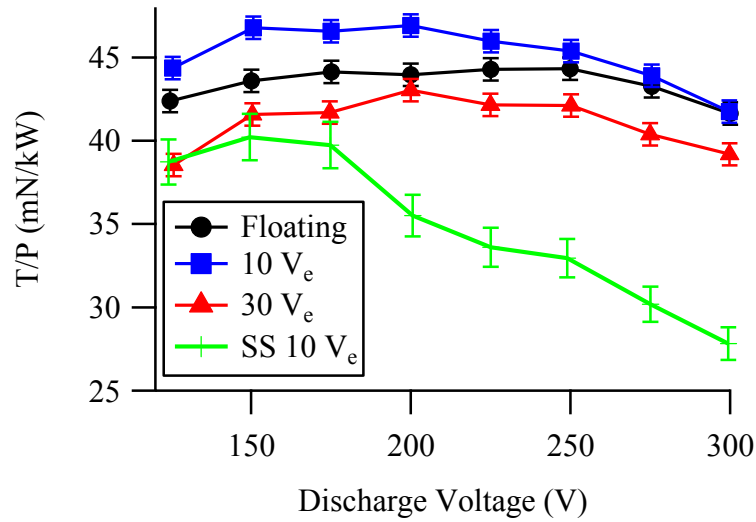


Figure 68. T/P ratio for EEHET at 9 A.

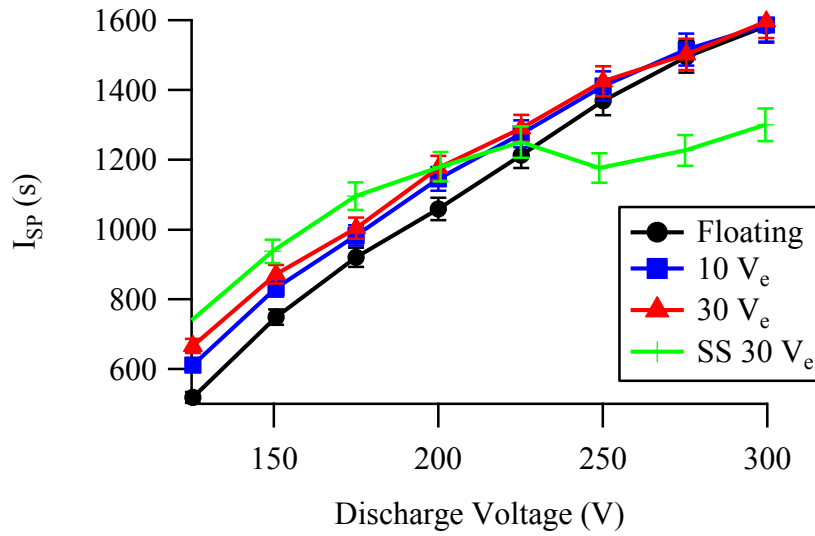


Figure 69. Specific impulse on krypton at 9 A.

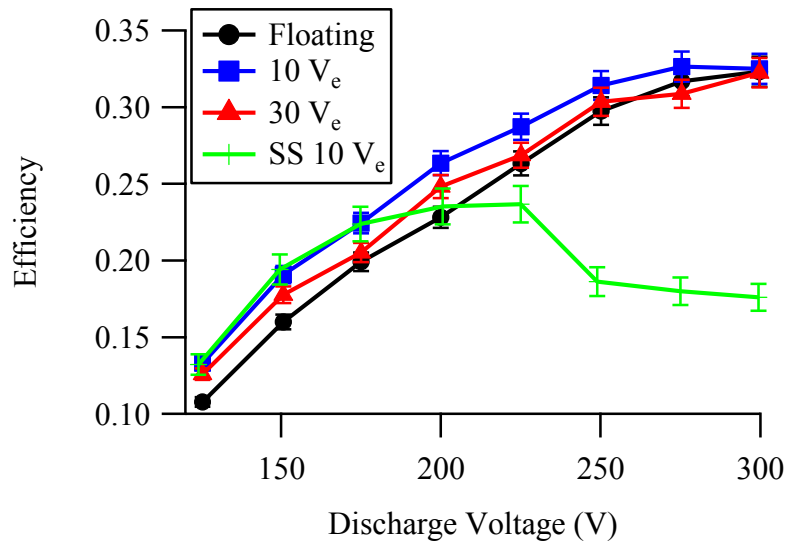


Figure 70. Efficiency on krypton at 9 A.

5.3.2 Faraday Probe

Along with thrust stand measurements, the EEHET far-field plume is investigated with the Faraday probe. The raw Faraday probe data for the Floating case is shown below in Figure 71. The profile exhibits a double peak structure signifying the focal length of the thruster is longer than the measurement radius of one meter. This is common

observation for large thruster such as the EEHET. If the measurements are taken further downstream, the ion density would have a single peak as the beams from the left and right sides of the channel merge. At low discharge voltages such as at 125 V_d, the profile falls to nearly a single peak. This is due to the decreased number of ions exiting the thruster with lower energy and larger angular divergence. The slower ions are able to merge faster and thus reduce the focal length.

The current density peaks rest around $\pm 6-9$ degrees on either side of centerline. The exact peak location depends on operating conditions. The asymmetry of the peaks and at the far left and right sides can be attributed to alignment errors and thruster imperfections. HETs are ideally axis-symmetric, but realistically small deviations exist. These can be caused by machining tolerances, alignment errors, and non-uniform propellant distribution from the anode. The deviations can cause the plasma to be denser or more divergent at certain locations, thus the non-symmetric profile.

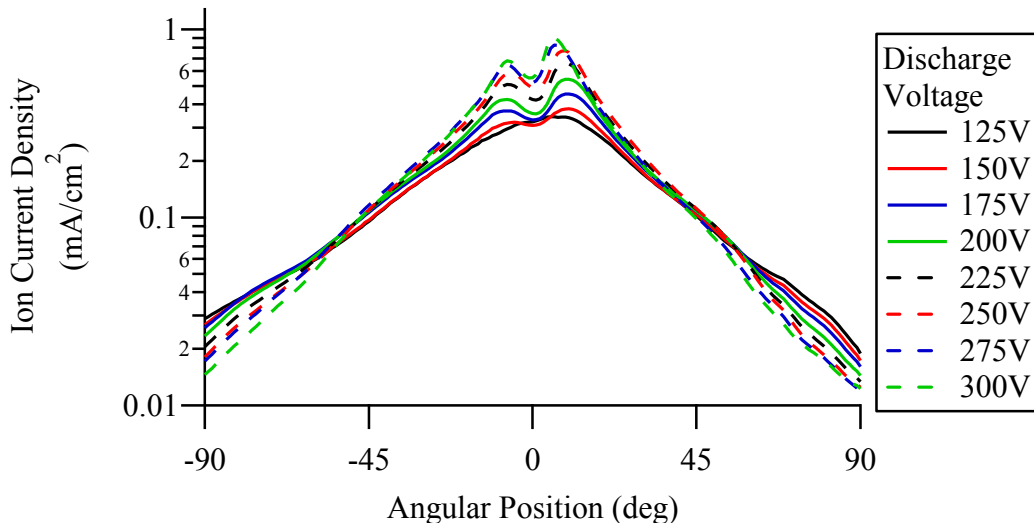


Figure 71. Ion current density profile for Floating electrodes on krypton at 9 A.

Figure 72 thru Figure 75 present the ion density profiles at select discharge voltages for all three electrode conditions. Additionally, an exploded view of the left

wings of the profile is shown. At low voltages, the electrodes cause increased ion density near centerline and decreased density in the wings. This is a different result than the BN to Floating case where the profile experienced an overall shift at all angles. This non-uniform increase and decrease signifies ions are being moved from the wings toward centerline. This is evidence for ion focusing by the electrodes.

At high voltages the effect is less pronounced, and at 300 V the electrodes cause decreased ion density. The electrodes appear to have decreasing effectiveness with increasing discharge voltage. This makes sense as the additional potential from the electrodes become a smaller fraction of the total potential as the discharge voltage increases. Also the electrodes may be causing interference with the normal thruster performance by acting as a partial sink for the current as shown by the electrode current graph in Figure 66. The left and right wings have slightly different shapes. The likely reason for this is the electrical connection for the outer electrode is made at the right side of the thruster which is present during the electrode tests. The connection is protected from the plasma with a ceramic block as seen in Figure 50. The block may interfere with the plume.

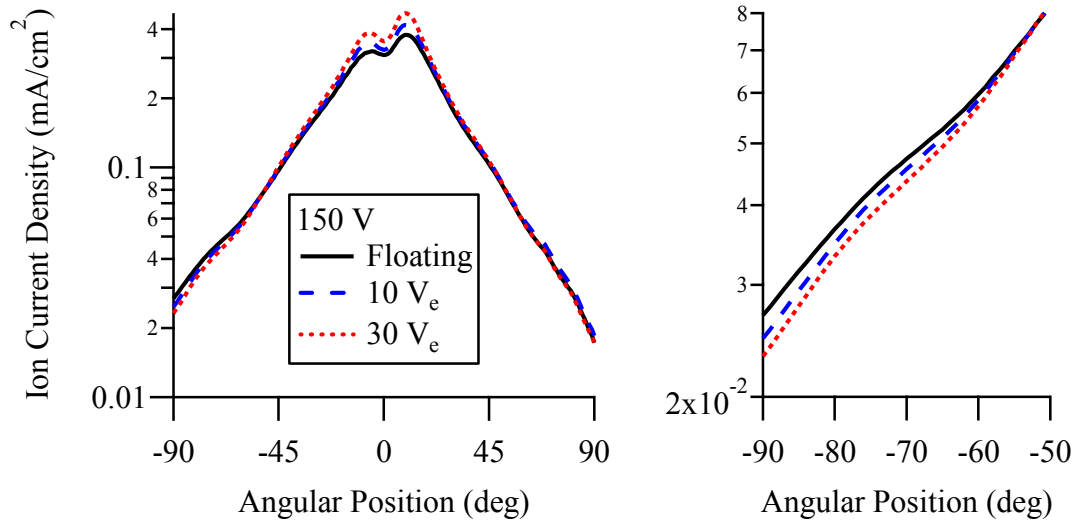


Figure 72. Ion current density profile for 150 V_d on krypton.

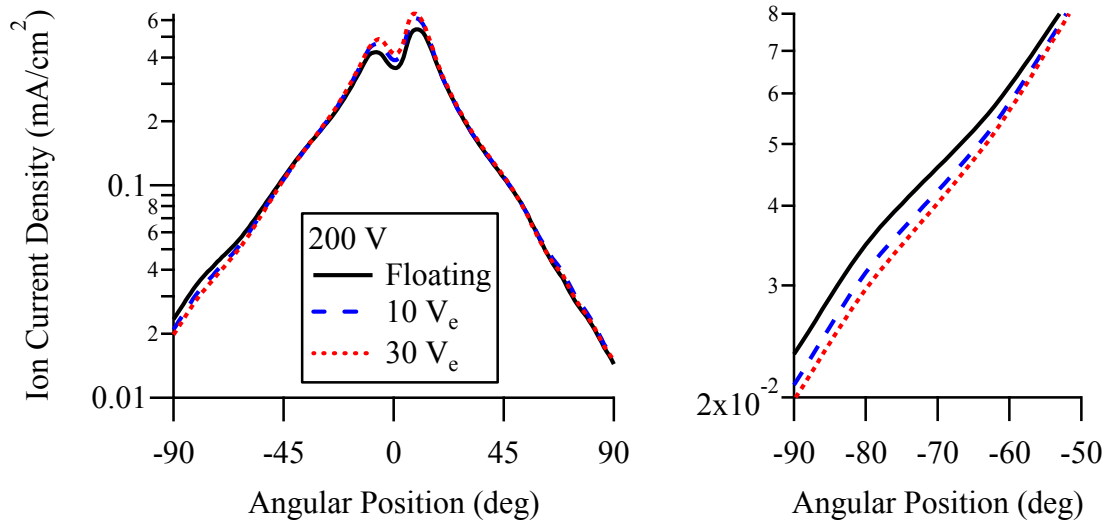


Figure 73. Ion current density profile for 200 V_d on krypton.

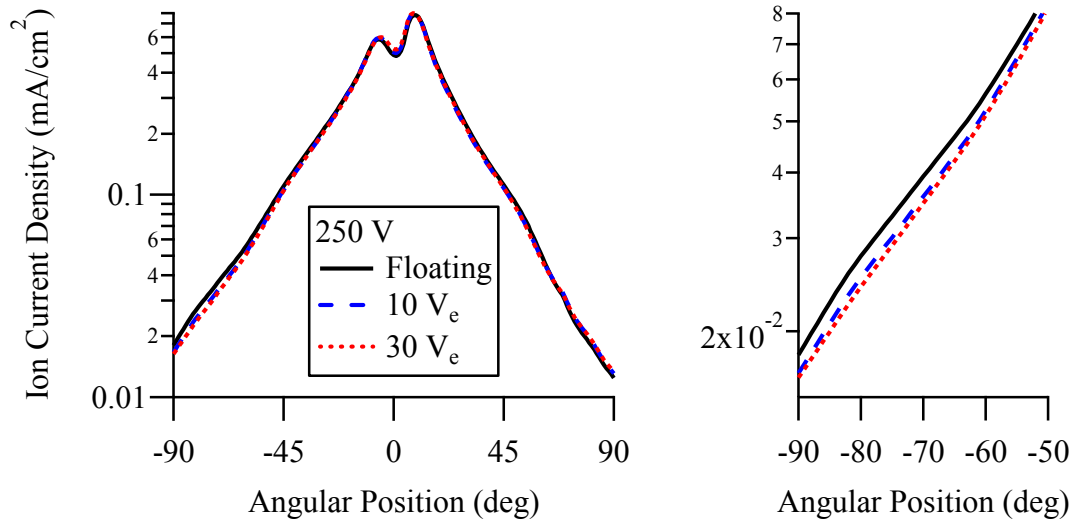


Figure 74. Ion current density profile for 250 V_d on krypton.

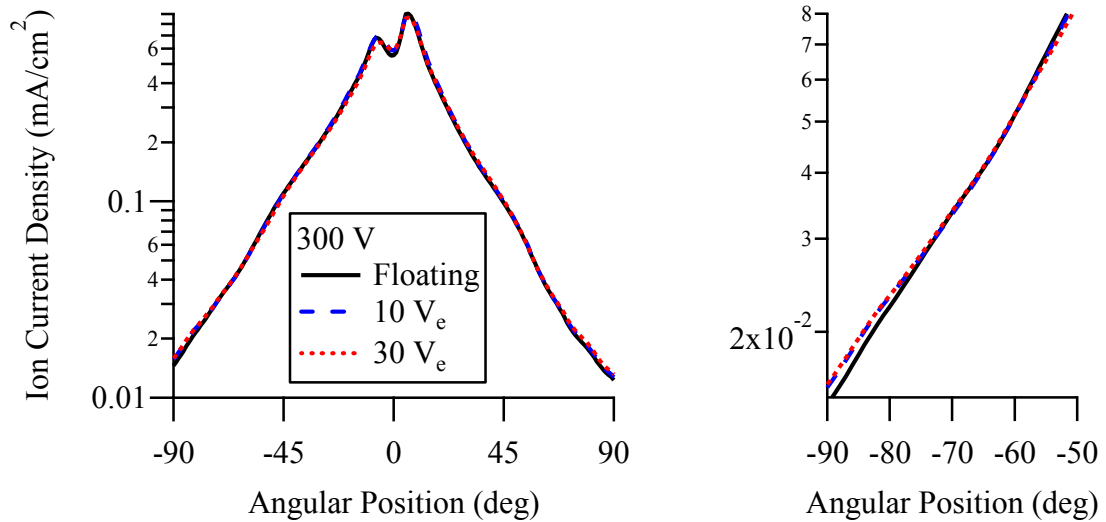


Figure 75. Ion current density profile for 300 V_d on krypton.

The ion beam current and plume divergence angle can be calculated from the ion current density profile. The beam current is a measure of the total positive ion current that exits the thruster. It is less than the discharge current as a portion of the discharge current is comprised of electron current from the cathode to the anode. The electron current is necessary to complete the electric circuit and maintain the discharge. Figure 76 shows the calculated beam current. The electrodes increase the ion beam current at low voltages and

decrease at high. The electrodes have similar levels of effect at 10 and 30 V_e . The reason for the drop in the beam current at 275 and 300 V is attributed to measurement uncertainties.

The overall change in beam current is relatively small, less than 0.5 A at any given discharge voltage. This does not necessarily confirm or deny the effectiveness of the embedded electrodes, especially taken into consideration the mass flow rate changes between the three electrode cases. The thruster is operated in constant current mode, thus the anode mass flow rate is adjusted to maintain 9 A current. Figure 77 shows the total mass flow rate for these operating points. These numbers include the anode flow and a constant 1.02 mg/s cathode flow. As the graph shows, biasing the electrodes results in decreased mass flow rate required to maintain current. The 10 and 30 V_e cases have similar flow requirements which are less than the Floating case. The 30 V_e case does exhibit a deviation at 125 V_d where the anode flow rate drops by a large amount while still maintaining 9 A.

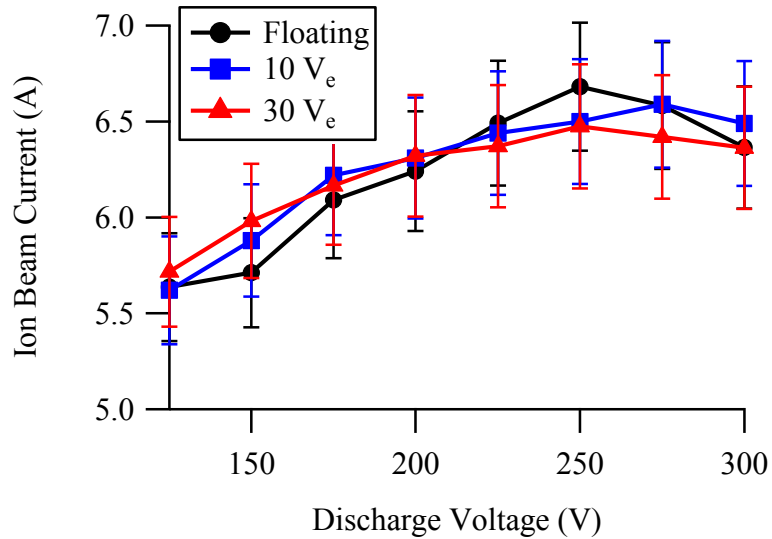


Figure 76. Ion beam current for total 9 A discharge current on krypton.

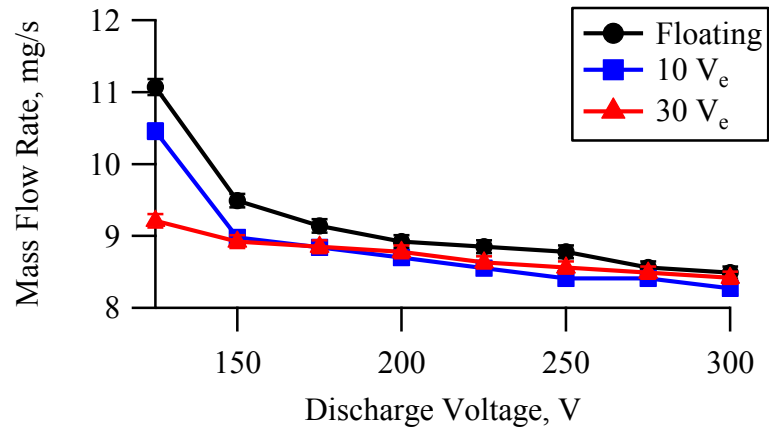


Figure 77. EEHET total mass flow rate for test cases on krypton.

To better visualize the relation between beam current and mass flow, consider the propellant efficiency shown in Figure 78. This is not the same parameter as propellant utilization. Propellant utilization takes into account multiply-charged ions, which is not done here. However the propellant efficiency still gives an idea of the ion beam behavior. As the graph shows, the electrodes increase the propellant efficiency. At 10 V_e this increase occurs at all discharge voltages, but at 30 V_e the propellant efficiency falls to Floating levels at high voltages. This matches with the observed changes in the ion current density profile seen in Figure 74 and Figure 75. At higher discharge voltages, the mass flow rates also do not vary much. These observations point to the electrodes having less effectiveness at high discharge voltages.

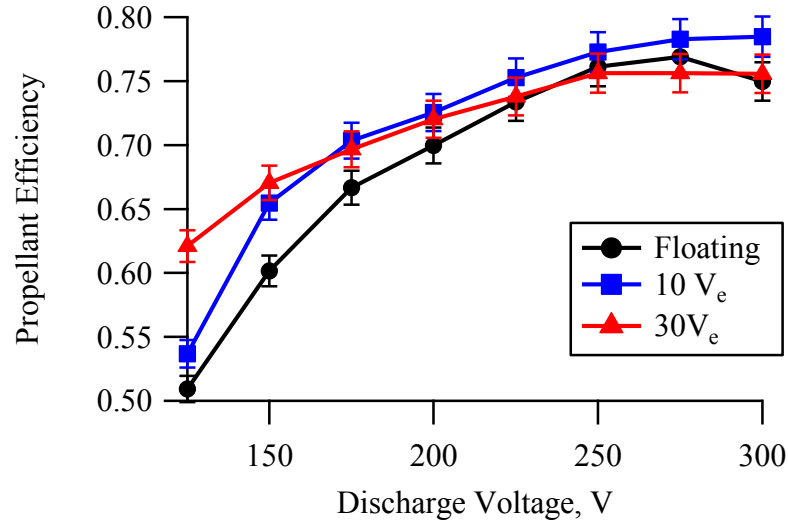


Figure 78. Propellant efficiency, defined as ion beam current/total flow rate, for the three electrode cases on krypton. The electrodes increase the propellant efficiency for most discharge voltages.

The second calculated value from the ion current density profile is the plume divergence angle, which is shown in Figure 79. In a similar trend as the beam current, the electrodes decrease (improves) the plume angle at low voltages. The maximum decrease is 2.7 degrees at 175 V_d, 30 V_e. The decrease in the plume divergence may contribute to the increased performance seen in the previous section. Decreased divergence means higher axial flux of ions thus increase thrust. The contribution is larger at 30 V_e than 10 V_e. The plume angle trends also match the observed trend of small to no effect at high discharge voltages.

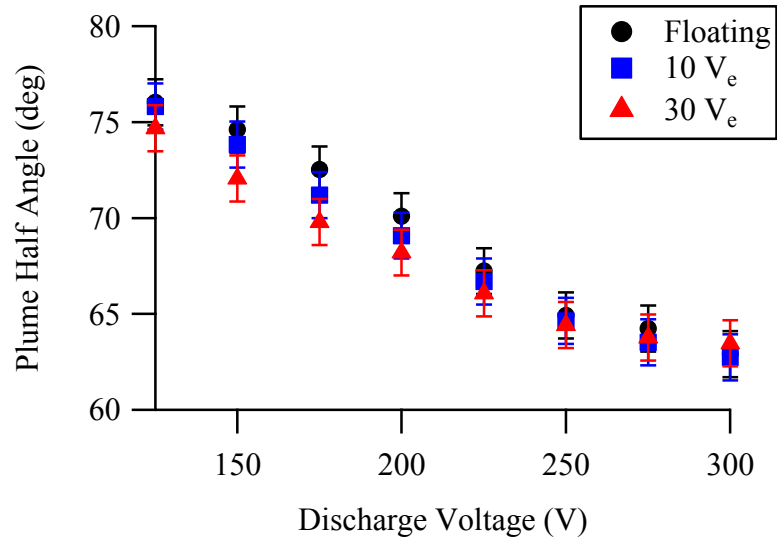


Figure 79. Plume divergence half angle at 9 A discharge current. The electrodes do cause a small decrease in plume angle, especially at low voltages.

5.4 Summary

The electrodes are redesigned from surface stainless steel bands to embedded graphite rings. The thruster channel is machined to allow the electrodes to sit flush with the channel surface. Additional BN rings are machined to fill in the extra space and maintain the same overall channel dimensions. The thruster is renamed the EEHET and tested on krypton propellant at constant 9 A discharge current. The BN and Floating cases tests showed the addition of the graphite into the channel caused very little changes to the thruster performance and plasma behavior. This matches well with previous work that shows the lower SEE of graphite only affects the thruster at voltages above 400 V. These results mean the Floating case is a good approximation for a standard BN channel. There may be a small increase in the ion density due to the addition of the graphite.

Performance measurements of the EEHET on krypton are taken and compared to the best data from the SS electrodes. The embedded electrodes perform better except at a few low discharge voltages. The SS electrodes have increased specific impulse and

efficiency at low voltages due to a lower mass flow rate. The decreased mass flow rate can be attributed to a high tank pressure causing neutral ingestion and thus abnormally high thrust for the given mass flow. Overall, the embedded electrodes demonstrate better performance as expected. A Faraday sweep of the krypton plume indicates the possibility of ions being moved from large angles towards centerline. The electrodes increase the propellant efficiency everywhere at 10 V_e, but only at low voltages at 30 V_e. This trend is also reflected in the plume divergence angle which shows small decreases at low discharge voltages.

CHAPTER 6

EEHET ON XENON

The EEHET was primarily tested from 125 – 300 V at $9 \text{ A} \pm 0.1 \text{ A}$ discharge on xenon propellant. A small amount of data was also collected at 20 A current. The propellant used was 99.9995% pure xenon. The magnetic fields settings were kept the same as the krypton and SS electrode tests. The electrodes were tested at Floating, 10 V_e and 30 V_e .

6.1 Low Current Xenon Operation

6.1.1 Performance

Figure 80 – Figure 83 show the performance (thrust, T/P ratio, I_{SP} and efficiency) of the EEHET running on xenon at 9 A. Shown are results for the three electrode conditions: Floating, 10 V_e , and 30 V_e . The definition for T/P ratio, I_{SP} , and efficiency are given in Equation 4-26 through Equation 4-28. The anode mass flow rate varied from 10.02 to 10.36 mg/s in order to maintain constant discharge current along with a constant 1 mg/s cathode flow rate.

The thruster performance increased along all four metrics with biased electrodes. T/P ratio and efficiency are higher at 10 V_e than at 30 V_e . The 30 V_e case has larger increases in thrust, however there is a corresponding large increase in electrode power which reduces the T/P ratio and efficiency. At 30 V_e , the electrodes collect 9 A of current. The current on the main anode is reduced to less than 1 A. The overall current supplied by the discharge power supply is still kept at 9 A however. This means there is some amount of current circulation between the electrodes and anode.

The maximum T/P ratio increase occurs at 150 V_d and 10 V_e, resulting in a gain of 7.69 mN (10 %) of thrust, 4.6 mN/kW (8.1 %) thrust-to-power, 123 s (17.4 %) I_{SP}, and 5.3% (27 %) anode efficiency. The percent values in the parenthesis indicate percent improvement over the Floating 150 V_d condition. The largest thrust increase is 15.3 mN at 150 V_d and 30 V_e. However the T/P ratio decreased at this condition. Chamber operating pressure is between $5 \times 10^{-6} - 7.7 \times 10^{-6}$ Torr-Xe for all tests. The uncertainties are estimated at $\pm 1.5\%$ for thrust, and $\pm 3\%$ for all other metrics and are included in the figure. The performance of the EEHET is lower or on par compared with available data for the original T-220HT. A direct comparison between the two is not strictly valid as the EEHET has a different magnetic field.

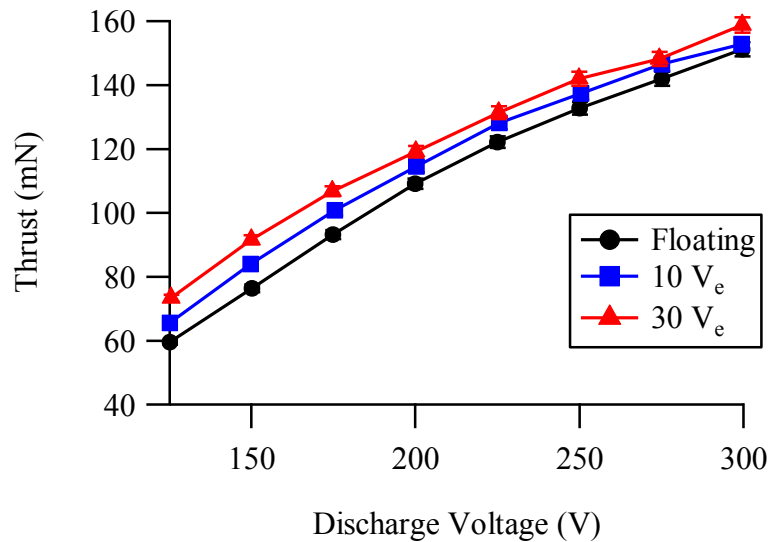


Figure 80. EEHET thrust on xenon at 9 A for the three electrode conditions. Both electrode conditions improve the thrust.

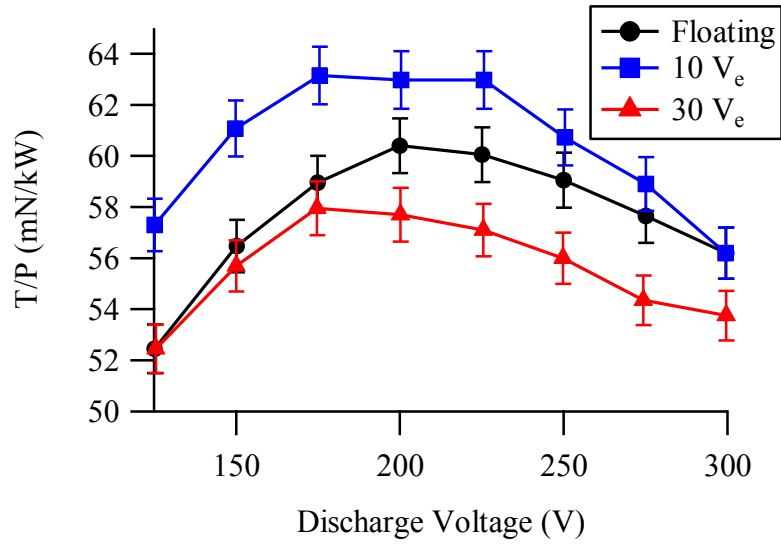


Figure 81. EEHET T/P ratio on xenon at 9 A for the three electrode conditions. The T/P only increases at 10 V_e. The decrease at the higher electrode potential is due to the high current collection offsetting the thrust gains.

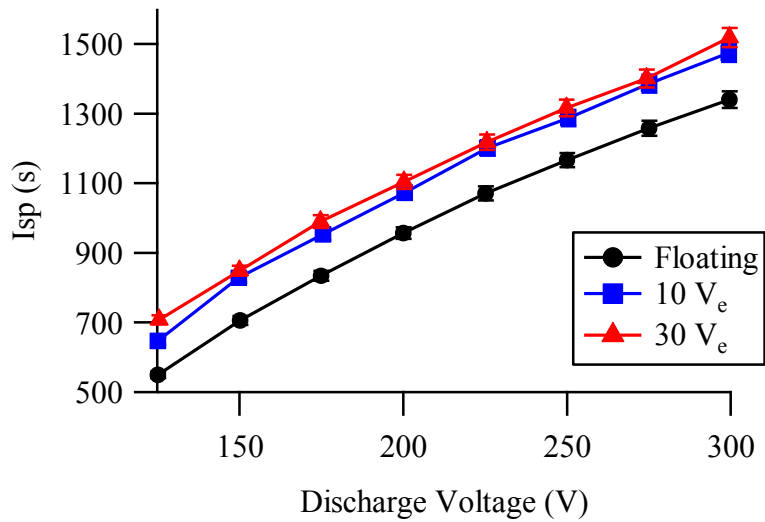


Figure 82. EEHET specific impulse on xenon at 9 A for the three electrode conditions.

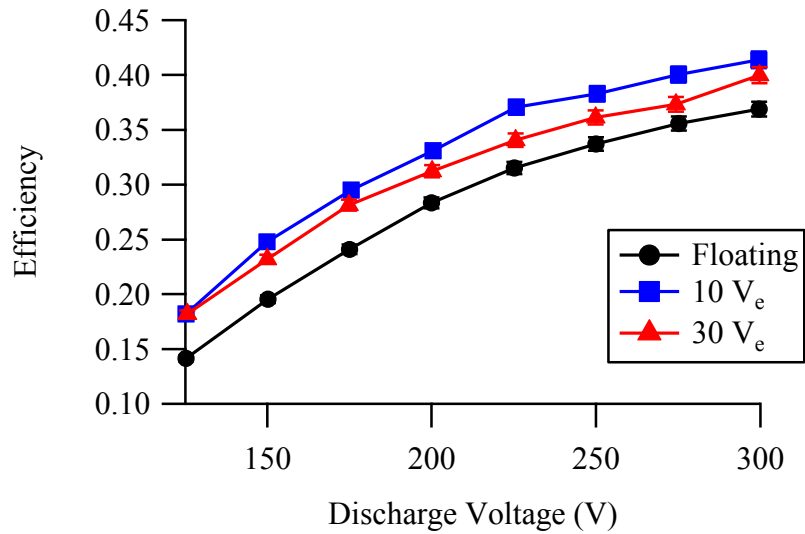


Figure 83. EEHET anode efficiency on xenon at 9 A for the three electrode conditions. Similar to T/P , efficiency incorporates total power, thus the high electrode current at 30 V_e causes a drop in efficiency.

The performance changes are much larger than the measurement uncertainty with the EEHET and clearly shows performance improvements when the electrodes are biased to 10 and 30 V_e. The results show that while 30 V_e generally produced the largest thrust, the extra power drawn by the electrodes resulted in the lowest T/P ratio and efficiency. The improvements are still more prevalent at lower discharge voltages as seen previously with steel electrodes. As expected the thruster performs better on xenon than krypton owing to the lower ionization rate and higher mass of xenon.

Figure 84 shows the current collected by the electrodes. The electrode current is quite different between the two bias levels, 10 and 30 V_e. Since the electrodes are connected to the anode power line, they share current with the main anode. This means at 30 V_e, when the electrodes draw 9 A of current, the anode has very little current. This response is similar to the behavior seen on krypton propellant. The full discharge current on the electrodes may cause the electrodes to act as the primary anode. The anode never

reads zero current however. Some current recycling occurs between the electrode and anode within the circuit as the discharge power supply current is held at 9 A.

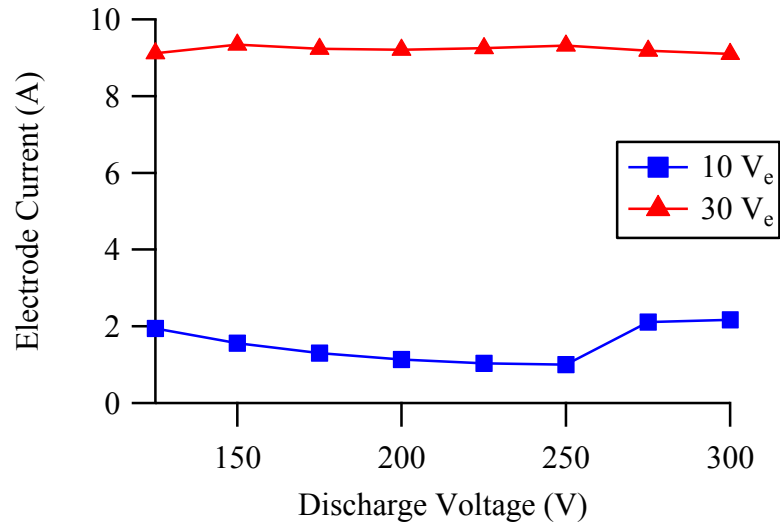


Figure 84. Electrode current at 9 A for 10 V_e and 30 V_e electrode bias. Similar to the krypton tests, the electrodes draw in almost all of the current at 30 V_e.

6.1.2 Faraday Probe

Figure 85 shows the ion current density plots from the Faraday probe for the EEHET on xenon propellant at 9 A. The probe is swept from -100 to 100 degrees with thruster centerline at 0 degrees. The current densities decrease with discharge voltage which results in fewer ions. Decreasing discharge voltage also means lower acceleration and ionization ability. All data are taken at discharge currents between 8.9 – 9.12 A as shown in Table 7 in the Appendix. The constant discharge current means decreased ion current at low voltages causes increased electron current.

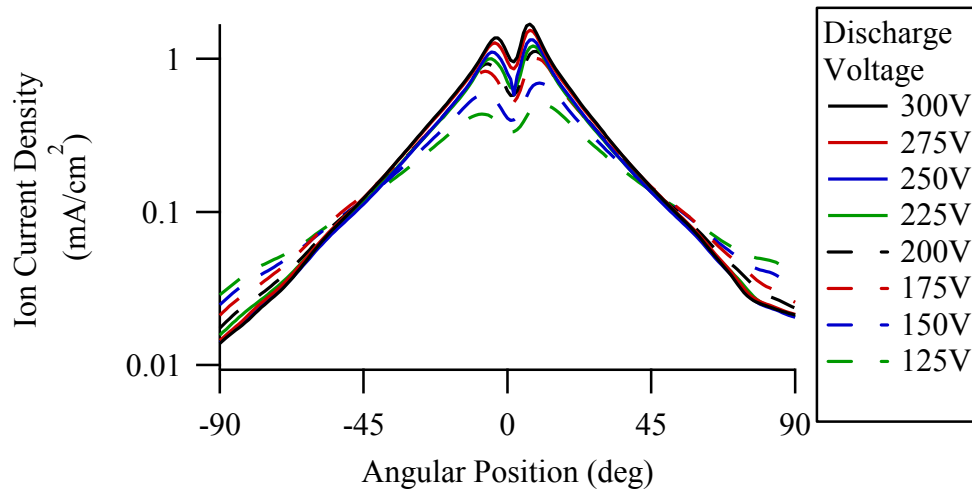


Figure 85. Faraday data for 9 A xenon with floating electrodes.

Figure 86 shows the change in the current density with biased electrodes for 150, 200, 250 and 300 V. The $10 V_e$ case shows a minor change from Floating, but $30 V_e$ creates a more noticeable change in the current density. The current density trends upward as discharge voltage is increased. Increase discharge voltage increases electric field which increases electron energy and thus improves ionization leading to higher ion densities. The current density increases at small angles resulting in larger peaks and decreases at large angles. The increase at small angles without a net upward shift of the profile indicates an increase in the ion density specifically in that region as opposed to everywhere. This is further supported by the decrease at large angles. Figure 87 shows a magnified view of the same data at large angles to the left of centerline. The effect is similar, but smaller on the right side of the profile due to asymmetries. The effect is also smaller at higher discharge voltages, likely for the same reasons as the performance changes.

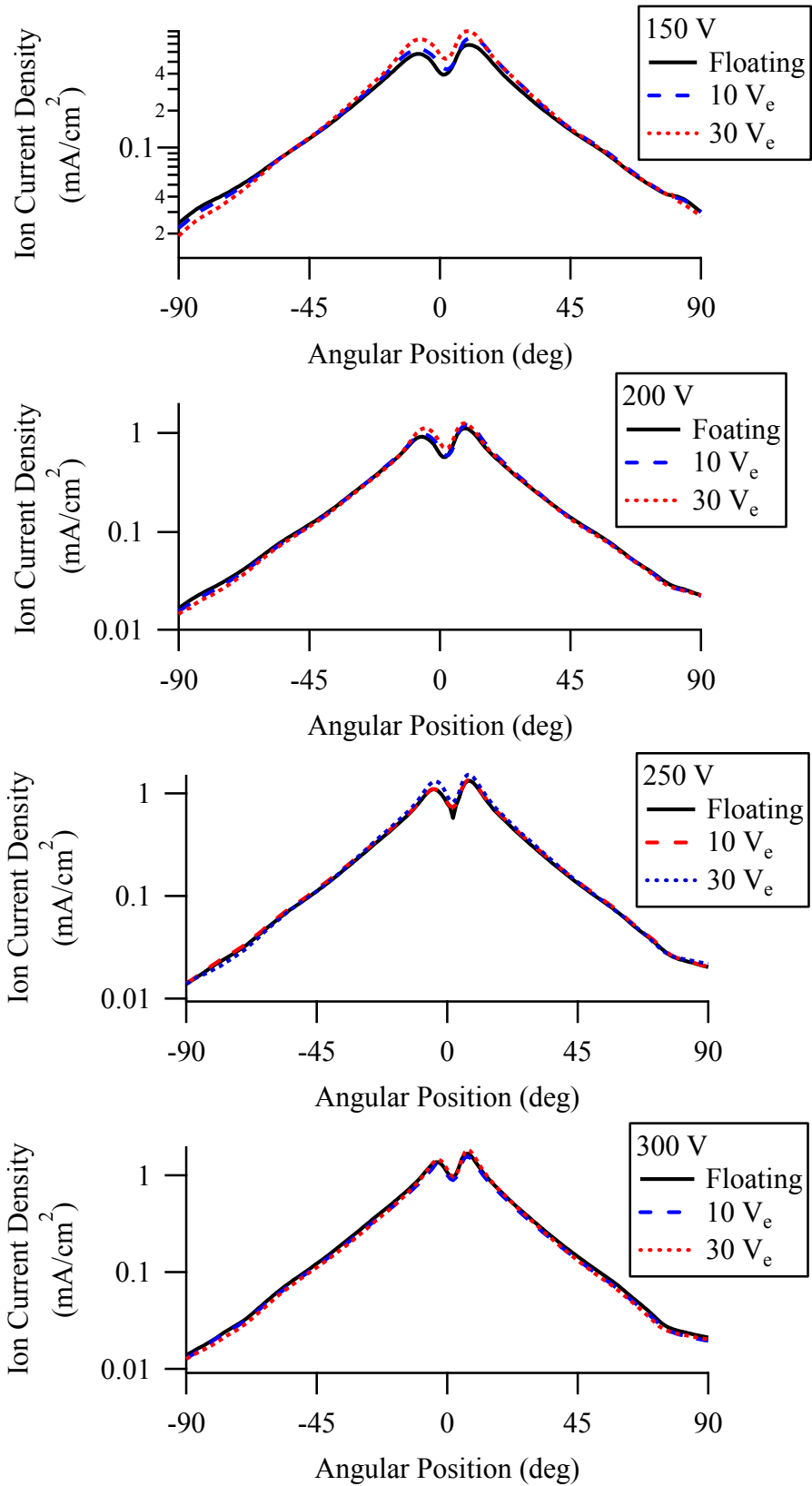


Figure 86. Ion current density profile for discharge voltages of 150, 200, 250, and 300 V for electrode bias configurations floating, 10 V_e, and 30 V_e.

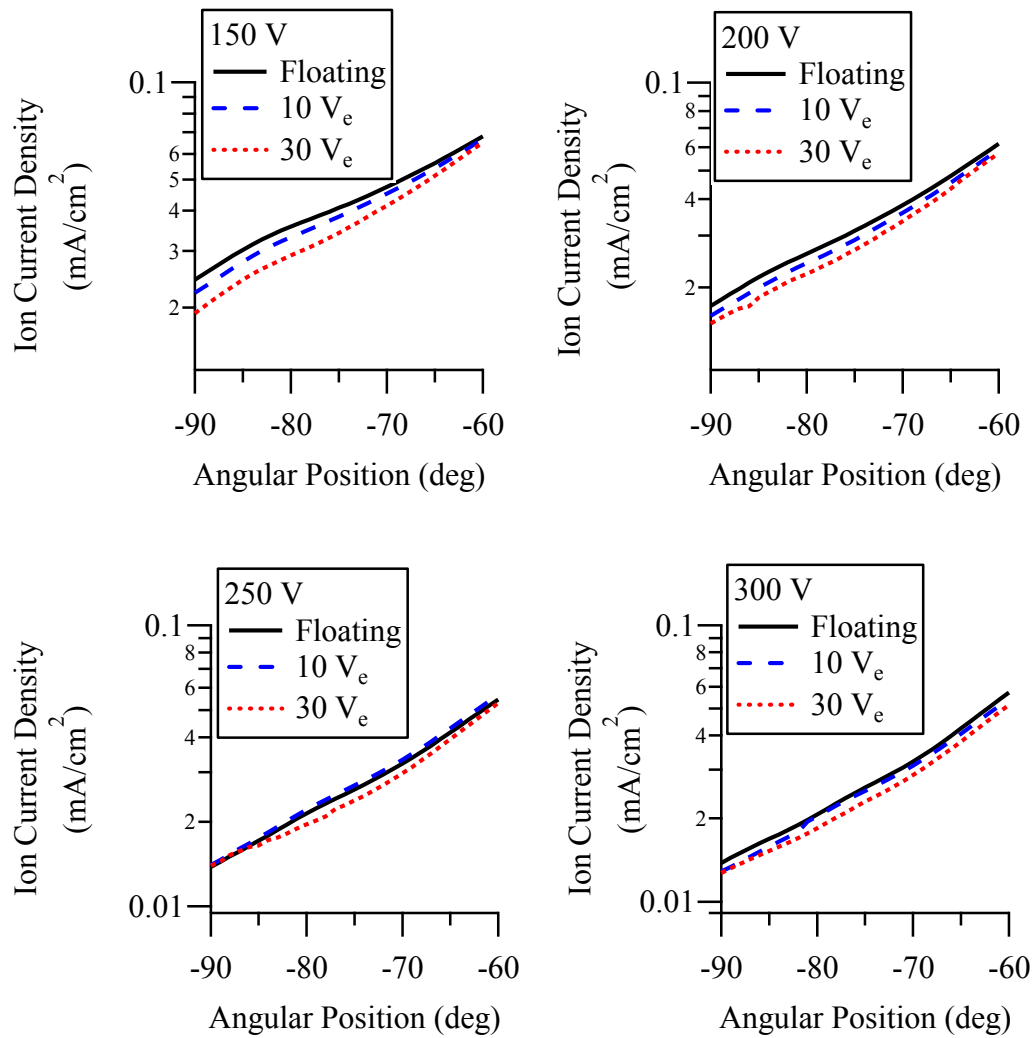


Figure 87. Close up ion current density profiles, from 60 to 100 degrees of chamber centerline.

Figure 88 shows the current fractions for 10 and 30 V_e at different discharge voltages. The current fraction is the ion current density with biased electrodes normalized by their respective Floating current density. The solid black line at 1 is the normalized Floating current density, and the blue and red lines are the normalized 10 and 30 V_e densities. The graphs show more clearly the change in current density near centerline and at large angles. Again the data indicates a shift of ions from large angles to centerline. If it is the case of an overall increase in ions everywhere, then the 10 and 30 V_e lines would

be largely flat and only vertically offset from Floating. This effect is more evident at low V_d , which matches the observed performance improvements. At 300 V_d , the ion current density with electrodes actually drops below the Floating data for the most part. Here the behavior is less consistent. The increases and decreases in current density largely cancel, resulting in very little net ion current change. The chamber pressure varied very little from $5 \times 10^{-6} - 7.7 \times 10^{-6}$ Torr-Xe, thus background CEX collisions are not the cause of the changes.

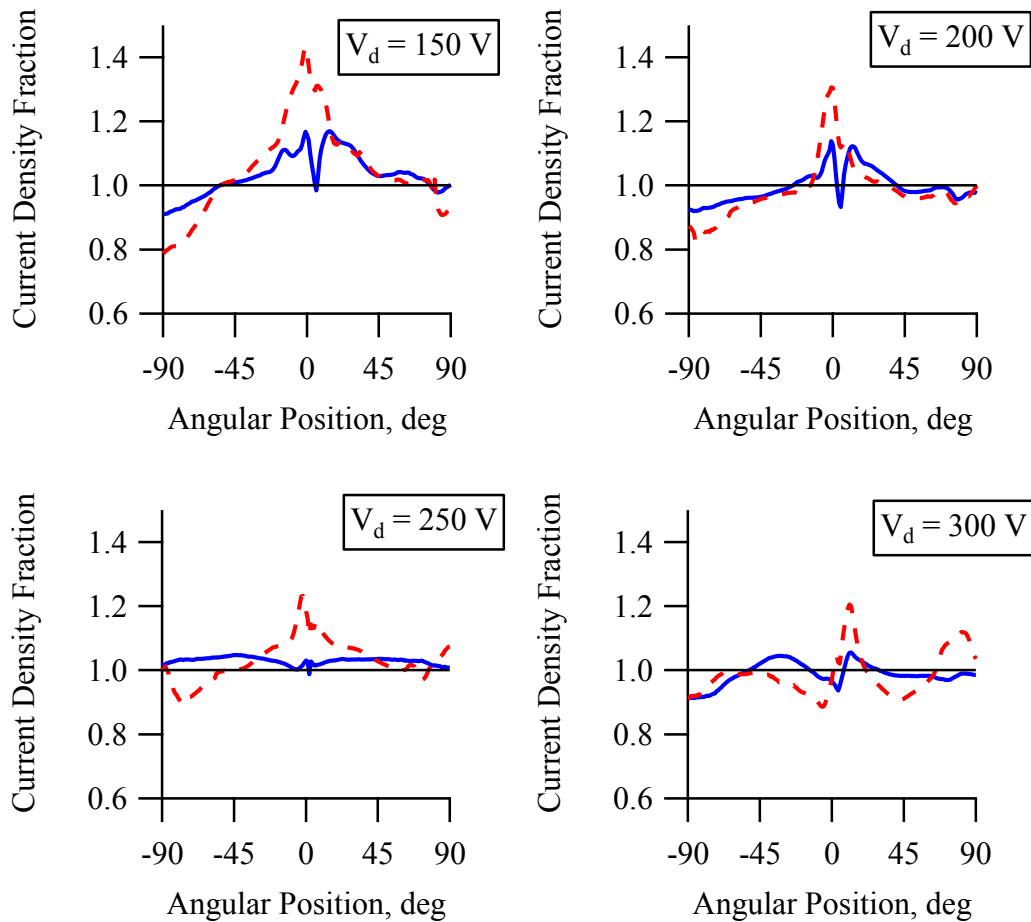


Figure 88. Current fraction (ion current density normalized by the Floating current density) showing Floating normalized (black), $10 V_c / \text{Floating}$ (blue) and $30 V_c / \text{Floating}$ (red).

At any given voltage, the discharge current is kept approximately constant and the magnet settings are the same. The only difference is the electrode power. As electrode

bias increases, so does the current seen by the electrodes. The average electrode current at 10 V_e and 30 V_e are 1.5 and 9.2 A respectively. The increase in the ion flux around centerline and decreases in the wings can be attributed to a narrowing of the ion beam and decreased plume divergence angle. Figure 89 plots the plume divergence angle for all three cases (Floating, 10 and 30 V_e). The plume angle calculations are described in Section 3.3.2.2.

As Figure 89 shows, there is indeed a decrease in the plume divergence angle when the electrodes are biased above anode potential. This divergence angle decrease with electrodes is not unexpected. Previous work done with secondary electrodes in the discharge channel also showed a decreased plume divergence angle.[28, 29] Though in those works the electrodes are placed near the channel exit, downstream of the radial magnetic field peak and no cusp fields are used. At 10 V_e the plume divergence angle reduction is very minor, only noticeable at low voltages below 200 V_d . Above that, the floating and 10 V_e case have nearly identical plume angles. At 30 V_e the angle decreases by up to five degrees at 125 V_d . At high discharge voltages, the electrodes seem to have no significant effect on the plume angle.

The current density profiles increases around the centerline of the thruster and decreases at large angles as electrode bias is increased. This shift of the current density is likely responsible for the observed plume angle changes. This indicates that ions are focuses toward centerline as designed. This conclusion is further affirmed by the increased ion beam current with biased electrodes shown in Figure 90. Ion beam current is the total ion current measured by the Faraday probe after compensation for CEX. The graph shows that the electrodes increase the total beam current. Combined with the

increase density near centerline and decrease in the wings, this strongly indicates a focusing effect. Ions that are normally lost to wall neutralization are now allowed to exit the thruster and be measured.

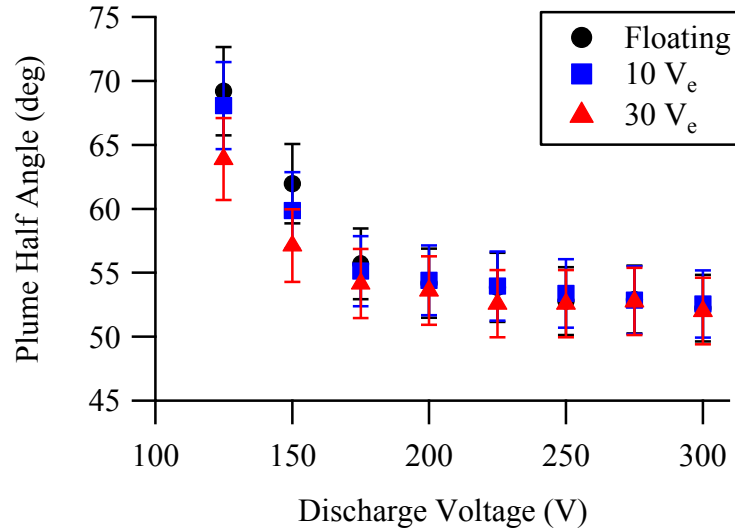


Figure 89. Plume divergence half angle. The error bars are large, but are from systematic errors, thus the results still indicate a net decrease in the plume angle at low voltages.

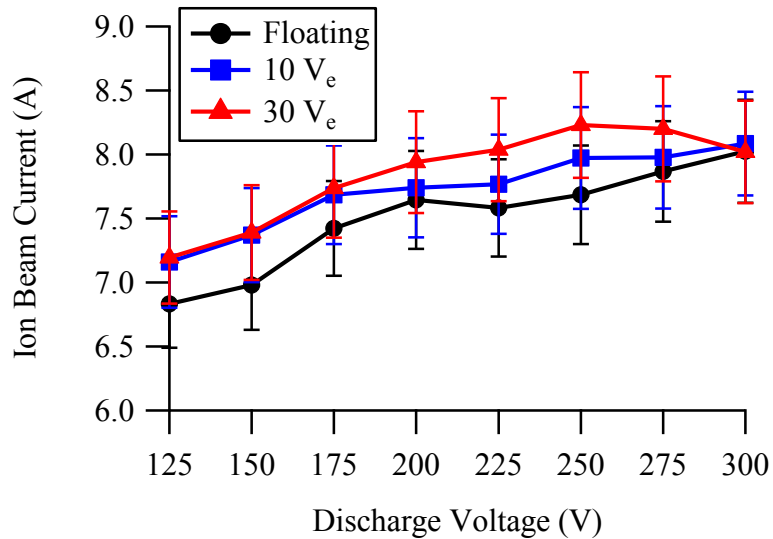


Figure 90. Ion beam current from Faraday measurements shown increased ion beam with biased electrodes.

6.1.3 RPA

Ion energy and plasma potential measurements are taken with the RPA and emissive probe at 10 locations around the plume. From 0 to 30 degrees measurements are taken in 5-degree increments and from 40 to 60 degrees in 10 degree increments.

Figure 91 shows the ion energy distribution function on thruster centerline for xenon at 9 A discharge current. The profile shows that the ion energy distribution function broadens as the discharge voltage increases. This is expected as high voltages result in not only more energetic electrons, but also a broader electron energy distribution. Thus, ions are created with a broader energy distribution as well.

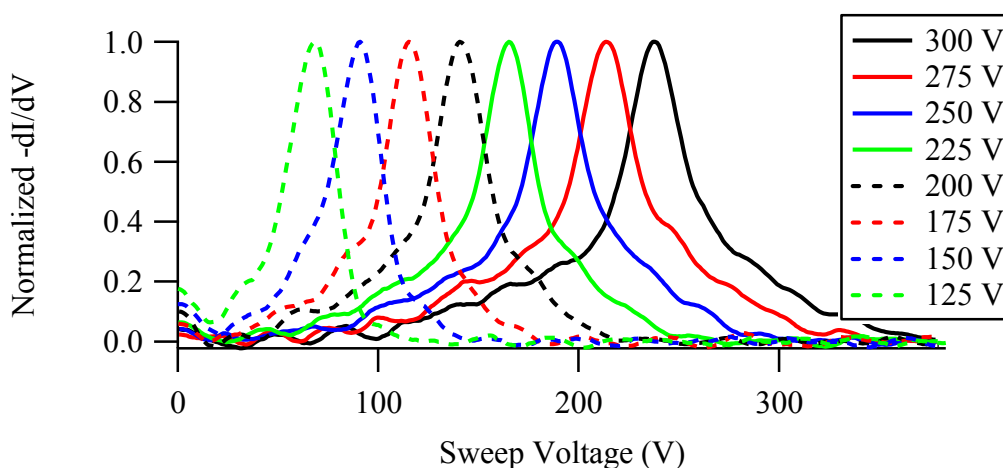


Figure 91. Ion energy distribution function on thruster centerline for floating electrodes at 9 ± 0.1 A.

Figure 92 shows the computed ion energy distribution function when the thruster is operating at 175 V and 9 A for all three electrode cases at four angular locations. The biased electrodes generate a shift in ion energy distribution function to higher voltages. Similar trends are observed for other discharge voltages. For 175 V_d, 10 V_e causes a slight rightward shift of the ion energy distribution, on the order of a few volts. At 30 V_e, the shift is an average of 20 V. Figure 93 shows the centerline ion energy for all the

operating conditions. The same trend in ion energy is observed at all discharge voltage levels.

Figure 94 plots the most probable ion energy for the 175 V operating condition at all measured angles from 0 to 60 degrees. The electrodes behave differently at 10 V_e and 30 V_e , which is evident in the different ion energies.

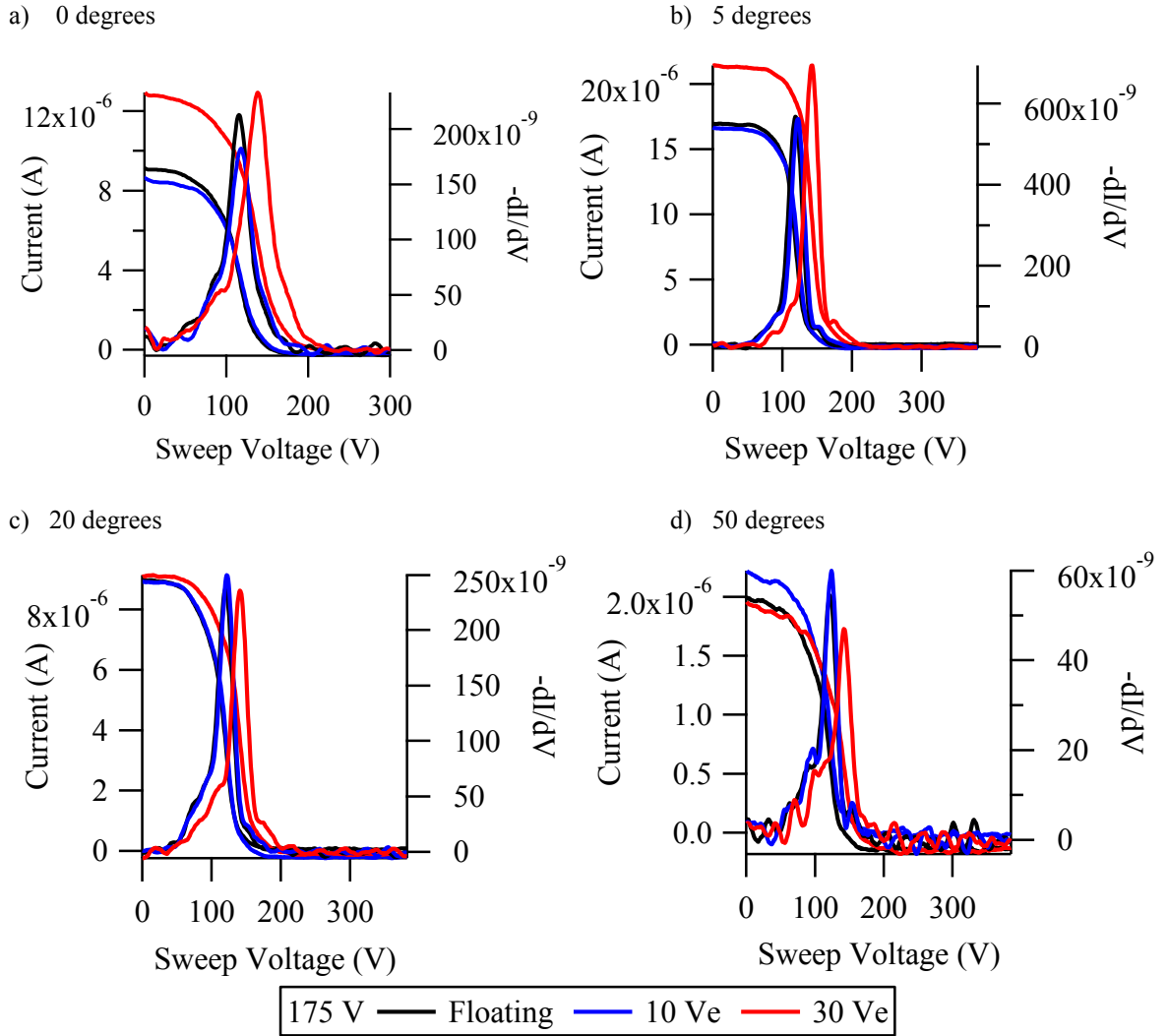


Figure 92. Ion energy distribution function at 175 V discharge at various angular positions.

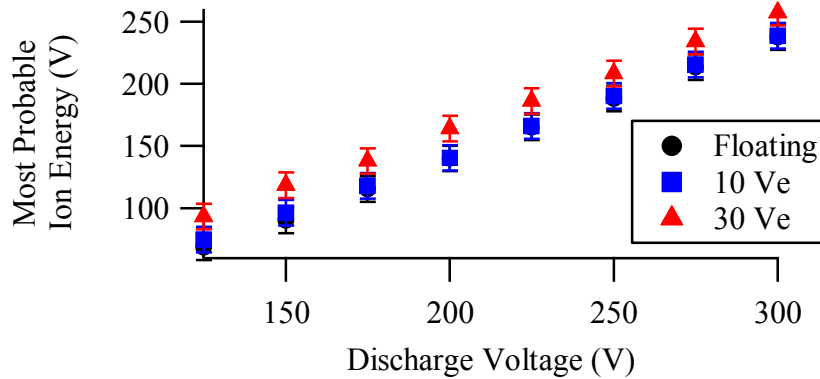


Figure 93. Most probable ion energy for Floating, 10 V_e , and 30 V_e at 9 A. The small change in ion energy at 10 V_e and large change at 30 V_e is present at all voltages tested.

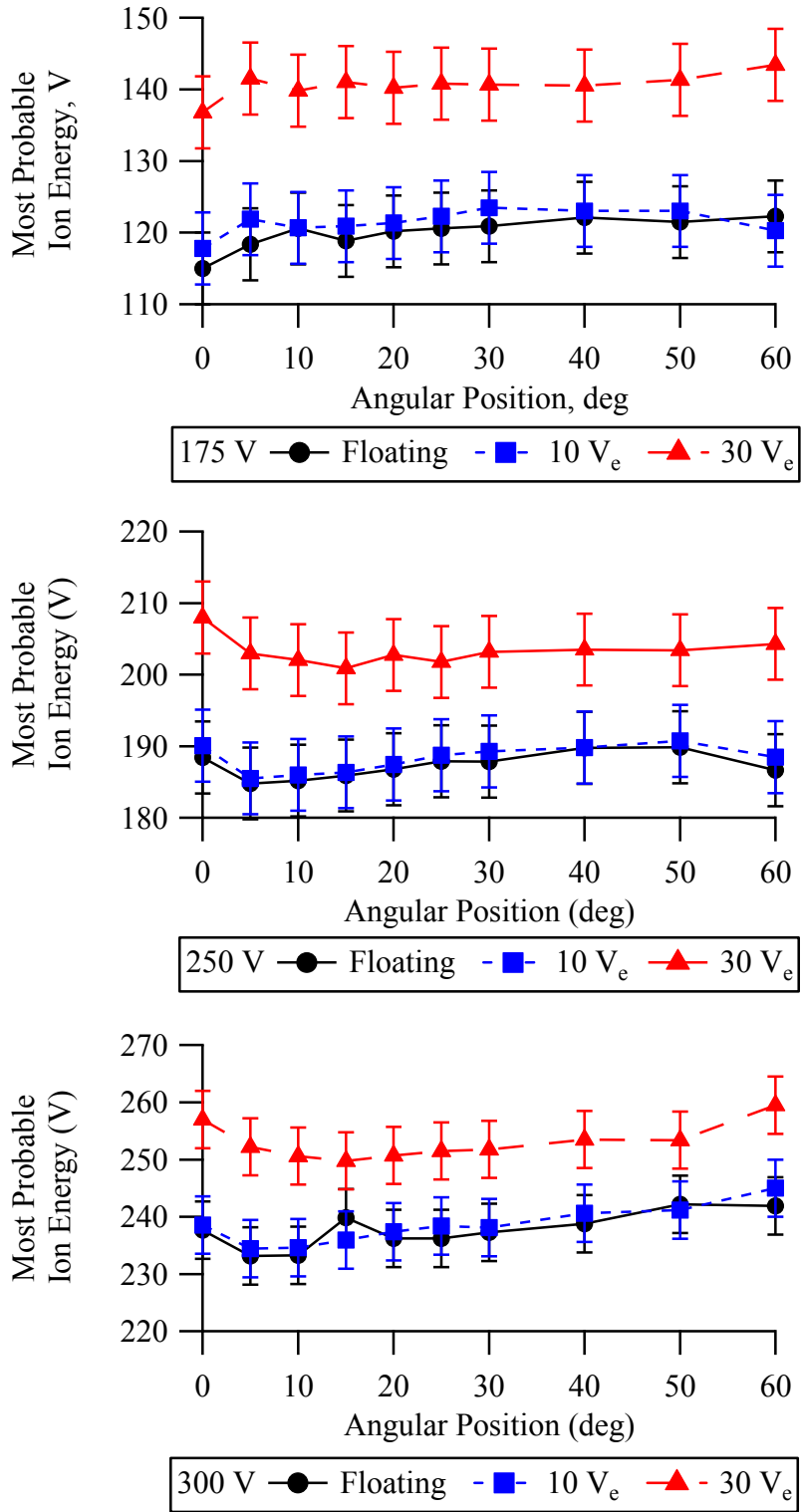


Figure 94. Most probable ion energy for the ion energy distribution function at each measured angle on xenon at 175, 250, and 300 V_d from Floating to 30 V_e. The trend occurs for all discharge voltages.

6.1.4 Far-Field Plasma Potential

The plasma potential measurements taken with the emissive probe are shown in Figure 95 and Figure 96. Figure 95 shows the plasma potential for the Floating condition at all angular positions. The potential is highest around 8 degrees which corresponds to the peak in the ion current density profile. It drops off almost linearly as the angle increases. This decrease in plasma potential at large angles is expected. The plasma potential is an averaged value of the particles at a location. Within the chamber there are background neutral particles that cause the CEX mentioned earlier. Near centerline, the ion density is high as seen in the Faraday results. The ions greatly outnumber the neutrals and CEX are a negligible contribution. At large angles however, the CEX collision rate grows due to decreased ion density. CEX collisions results in slow, low-energy ions that decrease the plasma potential.

Figure 96 shows the plasma potential for all three electrode cases at centerline and 30 degrees. At both angles there is an increase in plasma potential with the electrodes. The increase is more evident at low discharge voltages and small angles. At higher discharge voltages and large angles, the plasma potential of the three different cases shows little change. The increase in potential with electrodes is likely due to increased acceleration. The electrodes are biased above anode potential, thus they provide a larger maximum potential within the channel. This in turn can increase the acceleration electric field providing increased ion energy. The 30 V_e potential shows a large increase than 10 V_e . This fits with the RPA data that shows a more significant increase in ion energy at 30 V_e . The similarity at high voltages can be attributed to the decreasing effectiveness of the electrodes. A 30 V increase is much more significant at 150 V_d than at 300 V_d . Thus, at

high voltages the electrodes may not be having large effects due to the already high potentials.

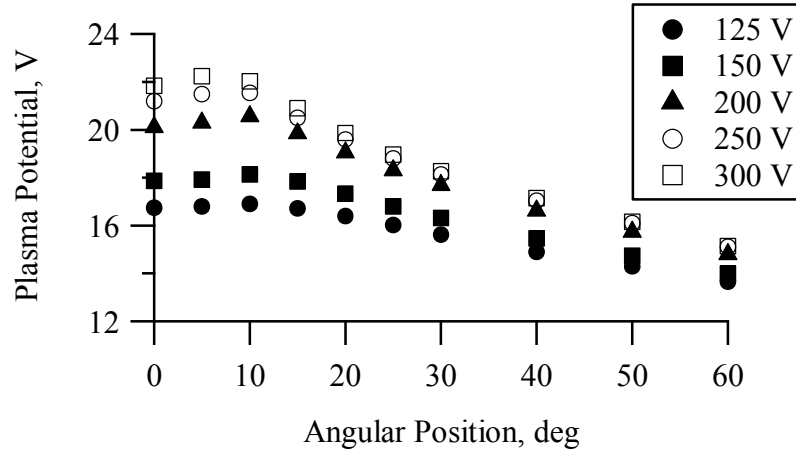


Figure 95. Plume plasma potential throughout the plume for the Floating case.

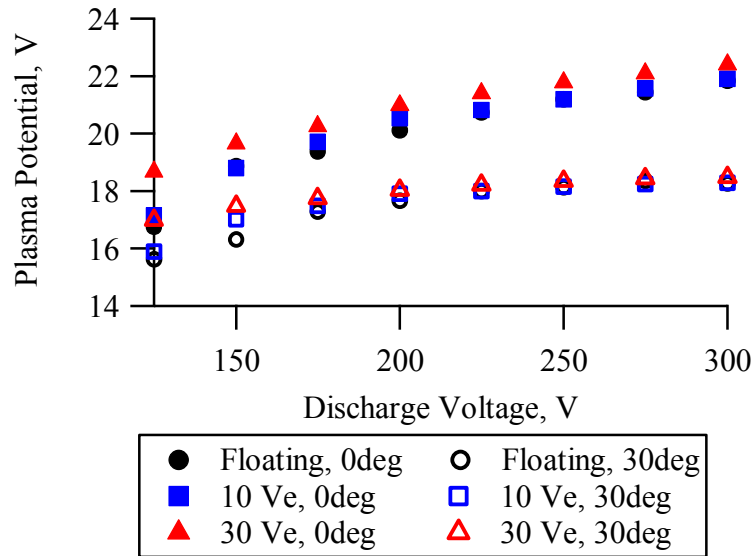


Figure 96. Plume plasma potential for Floating, 10 V_e , and 30 V_e at 0 and 30 degrees.

6.1.5 Internal Plasma Potential

In-channel plasma potential measurements are made using the HARP. The thruster is tested at the same three conditions: Floating, 10 V_e , and 30 V_e . The measurement area is the same as in Chapter 5, namely a 26 x 50 mm area within the

channel. A centerline sweep is also taken that extended into the plume. Figure 97 shows the internal plasma potential results for the three conditions. The Floating condition shows a potential distribution with a high gradient near the channel exit that defines the ionization/acceleration region. The contours are convex and create a slight diverging electric field near the exit. The diverging electric field will give ions increased radial velocities and cause increased plume divergence angle. Near the anode and electrodes, the potential is relatively flat and surrounds the anode. The floating electrodes have no effect on the potential as noted in Chapter 5. The potential ranges from 65 to 130 V.

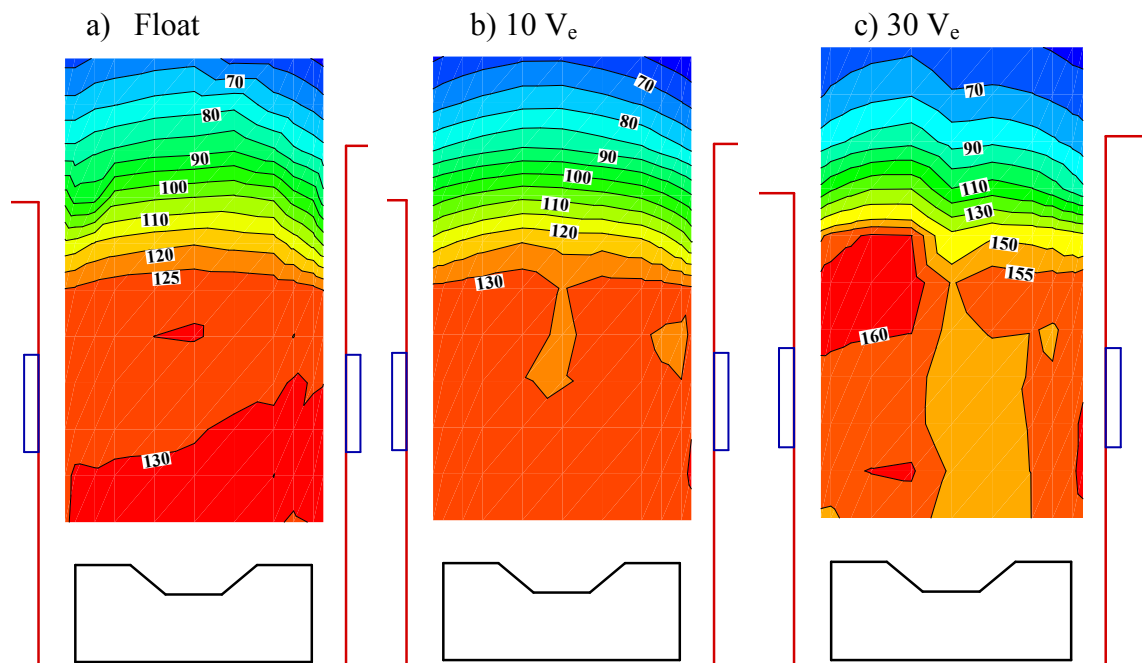


Figure 97. In-channel plasma potential map for 150 V anode discharge with Floating, 10, and 30 V_e electrode conditions.

With powered electrodes, there are two main changes to the potential contours. The first is a division of the high potential regions at the upstream end of the channel near the electrodes. It can be seen clearly at 30 V_e , and somewhat at 10 V_e , that the high potential

region near the anode and electrodes split into two separate areas with a lower potential area between. The pockets of high potential conform to the cusp-shaped magnetic field regions to a first order as shown in Figure 98. This pocketing of the potential will generate electric fields in the back of the channel pointed toward channel centerline. These fields in turn focus ions, and are a possible cause of the observed focusing in the plume data.

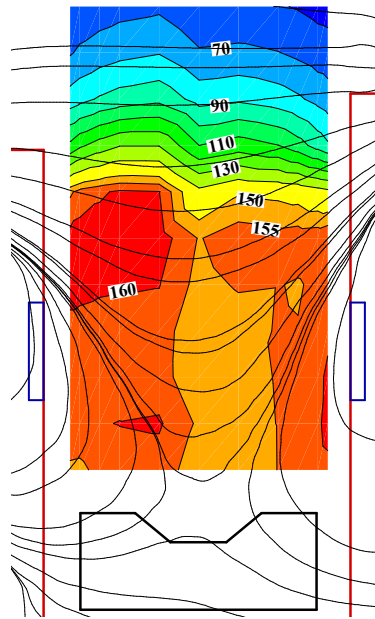


Figure 98. 30 V_e xenon potential contours with overlaid static magnetic field.

The second main change that can be seen in the potential measurements is the increase in potential range. When discharge voltage is increased, the potential contours typically experience a similar increase in maximum potential. This is true in the 30 V_e case, but not so at 10 V_e . At 10 V_e , the maximum potential increased by less than two volts over the Floating case. The high potential region is expanded to cover a larger area though. At 30 V_e , the maximum potential increased by 30 V over the Floating case. This difference in potential increase matches the different ion energy gains seen in the RPA

data. The maximum potential becomes dictated by the electrodes instead of the anode. This further proves the theory that at 30 V_e the electrodes become the primary positive electrical terminal instead of the anode.

6.2 High Current Operation

The majority of the experiments with the EEHET are done at 9 A discharge current. An effort was made to test the thruster at 20 ± 0.2 A current to see the effects of increase current and thus mass flow. The anode mass flow rate varied from Performance measurements were taken from 150 – 300 V in 50 V steps. Plume measurements are not available for 300 V however. The same electrode conditions of Floating, 10 V_e, and 30 V_e were tested and the same suite of performance and plume measurements were taken. In-channel plasma potential measurements were not possible at this operating condition due to rapid burnout of the miniature emissive probe preventing reasonable data acquisition.

6.2.1 Performance

The performance results for 20 A on xenon are shown in Figure 99 – Figure 102. The thrust is more than double the 9 A results as would be expected by the increased ion output. However, the other three metrics, T/P ratio, I_{SP}, and anode efficiency are on par, or lower than the 9 A results. In the low current results, the 10 and 30 V_e data showed clear, consistent improvements over the Floating condition. Here the changes are less clear with the electrode. The two electrode cases do consistently exhibit increased performance over the Floating case. Again this is most evident at low discharge voltages. Chamber pressure was between $1 \times 10^{-5} - 2.1 \times 10^{-5}$ Torr-Xe.

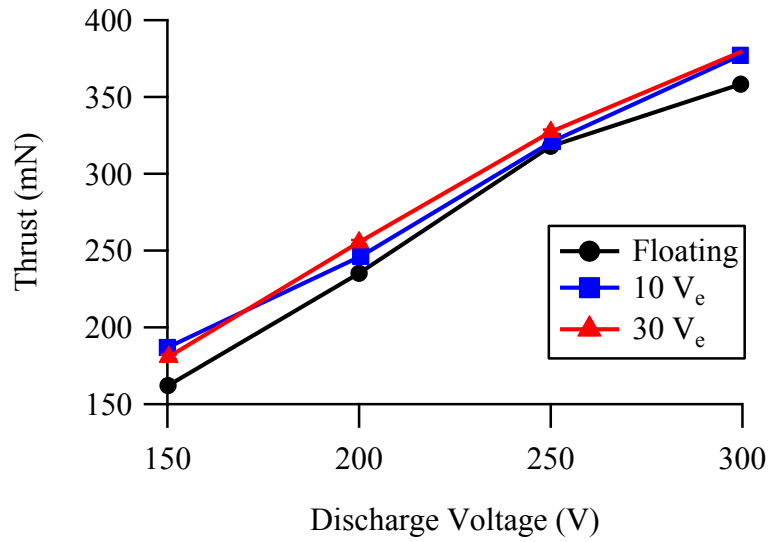


Figure 99. Thrust on xenon at 20 A for various electrode conditions.

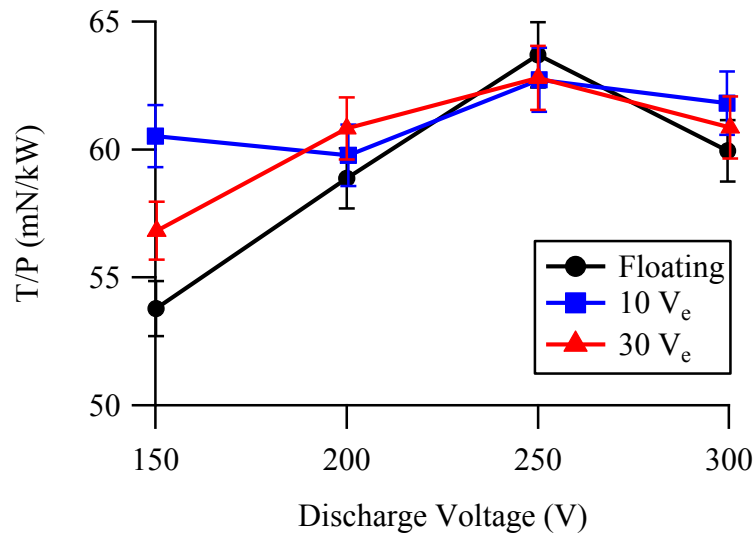


Figure 100. T/P ratio on xenon at 20 A for various electrode conditions.

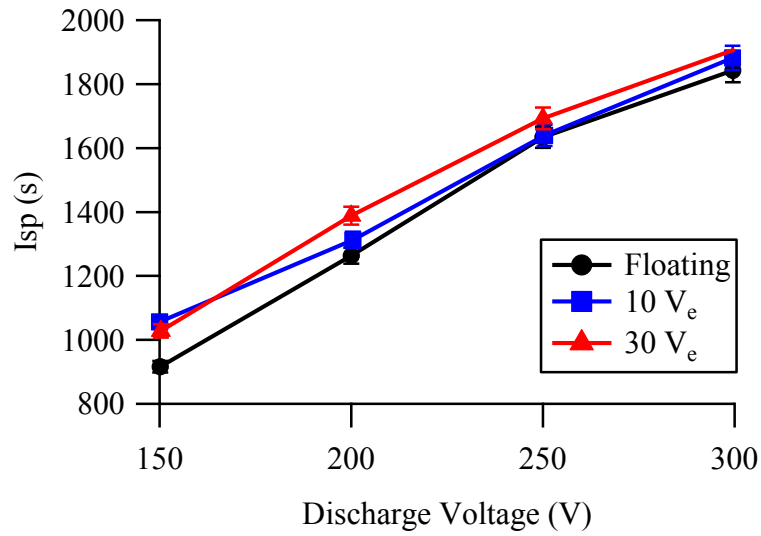


Figure 101. Specific impulse on xenon at 20 A.

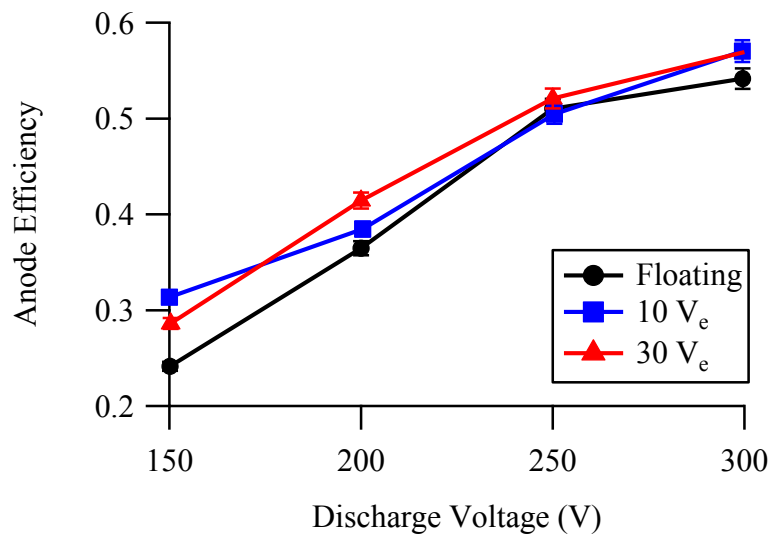


Figure 102. Anode efficiency on xenon at 20 A.

Figure 103 shows the electrode current at 20 A. The electrodes collected a large amount of current during the 20 A operation. The amount is higher at 10 V_e than at 30 V_e , opposite to the low current operation. The current level is also relatively constant across the discharge voltage range. The reversed electrode current response brings interesting questions to the performance. Using the electrode current as a measure of the primary

positive terminal, then the discharge plasma is being affected by both the anode and electrodes. At 9 A, the discharge current shifted completely to the electrodes at 30 V_e and the data showed a corresponding increase in ion energy. Here the increase in energy is relatively constant with the electrode voltage.

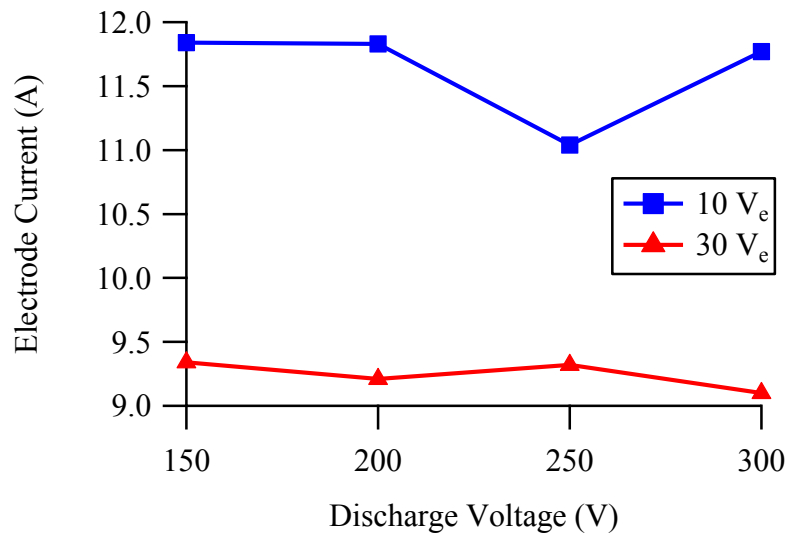


Figure 103. 20 A electrode current.

6.2.2 Faraday Probe

The Faraday measurements of the 20 A discharge setting with floating electrodes is shown in Figure 104. In addition, the 150 and 250 V floating electrode data from the 9 A set are also shown for comparison. At higher discharge currents, the ion density profile maintains a similar shape, but larger magnitude. At 20 A, the plume loses some of the double peak structure. At 250 V, the plume almost exhibits a single peak structure. However at low voltages the double peak is still very much evident, if shallower. This appearance of the centerline dip means the ion density does not decrease at the same rate across the plume. The centerline density drops faster thus the dip is seen at low voltages.

The cause of this can be attributed to increase plume divergence in addition to the decreased overall ion density as the discharge voltage decreases.

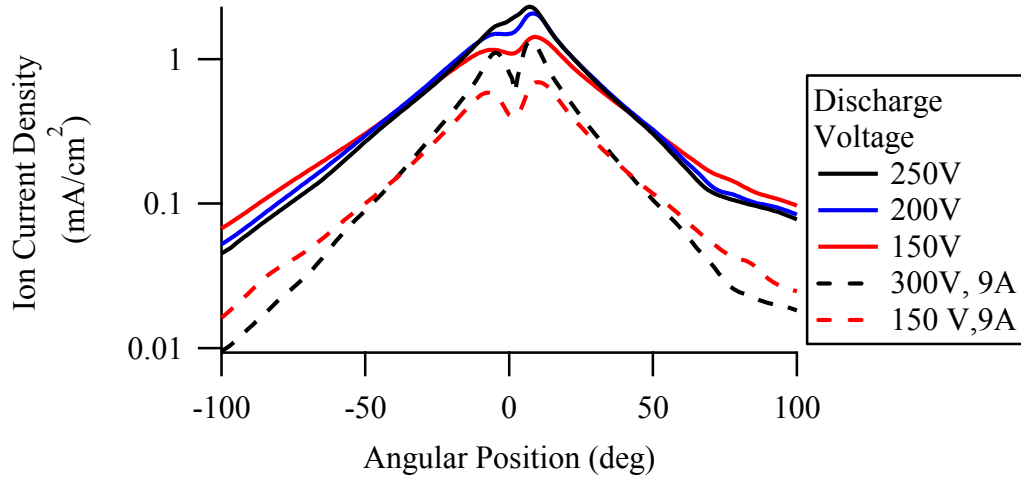


Figure 104. Ion current density profile for floating election on xenon at 20 A with the 300 V, 9 A data for comparison.

Figure 105 shows the ion current density profiles for 150, 200, and 250 V for the Floating, 10 V_e , and 30 V_e electrode conditions. The behavior at 20 A is different for that observed at 9 A. Here the electrodes increase centerline current density, but do not decrease the current density at large angles. In fact, at higher voltages the current density at large angles is slightly increased. Figure 106 shows the plume divergence angle for 20 A on xenon. The plume angle is larger at higher currents. The reason for this is the constant magnetic field that is maintained throughout the research. The optimized magnetic field for a given operating condition reduces the discharge current by reducing the cathode electron leakage current. The field was never optimized during this work. For the lower current tests, the field is strong enough to maintain a near optimized field condition. However at 20 A, the field is likely not close to optimized and thus results in abnormally high current and divergence.

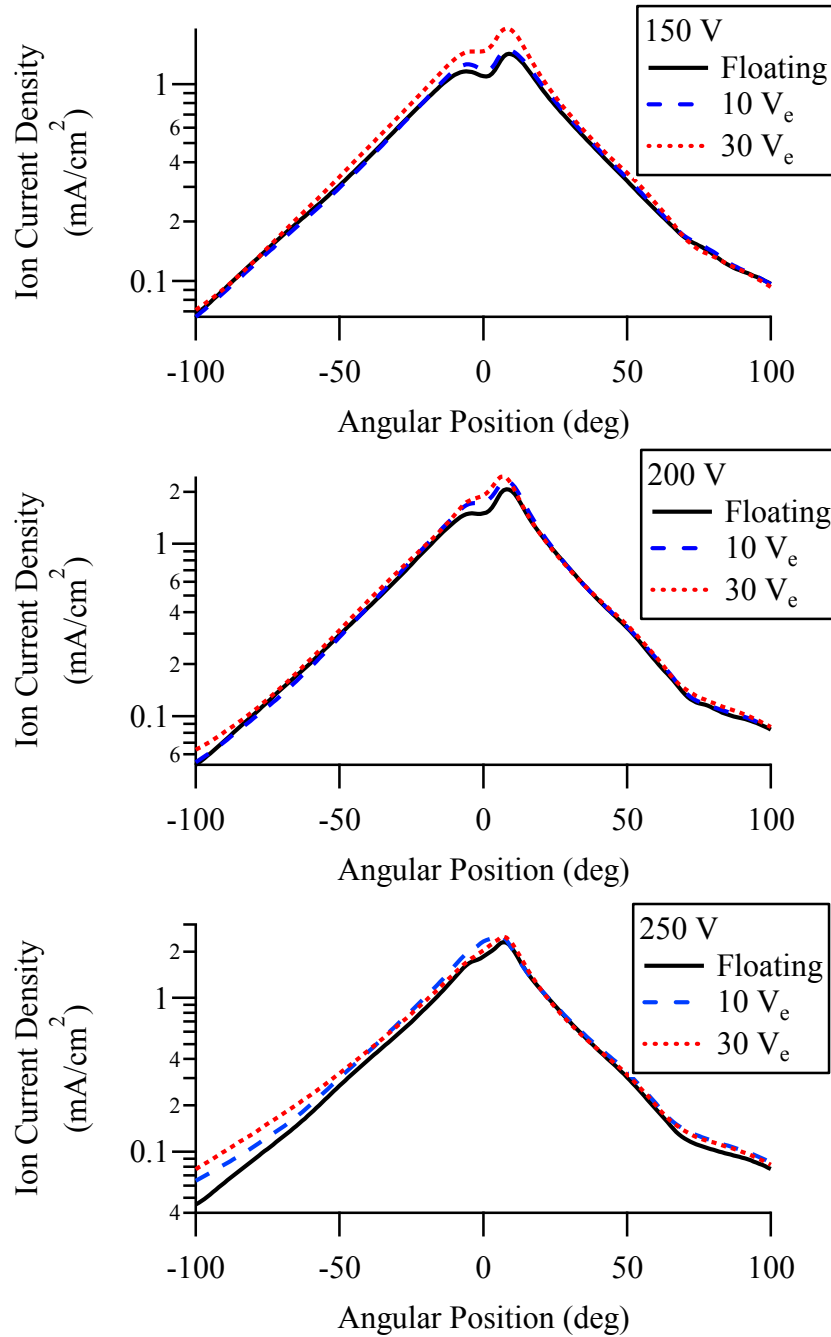


Figure 105. Ion current density for xenon at 20 A across all three electrode conditions (Floating - 30 V_e).

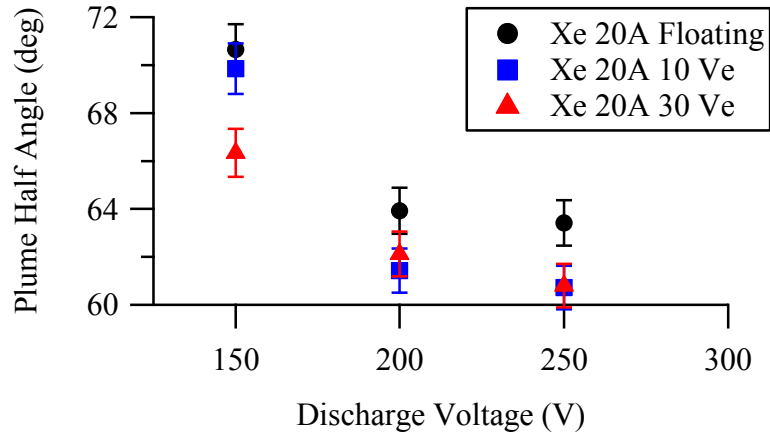


Figure 106. Plume divergence half angle for xenon at 20 A.

6.2.3 RPA

The ion energy distribution for the measurements taken at 20 A are shown in Figure 107 for the Floating condition. The distribution moves toward higher energy and broadens with increasing discharge voltage. This is typical and similar to the behavior at 9 A.

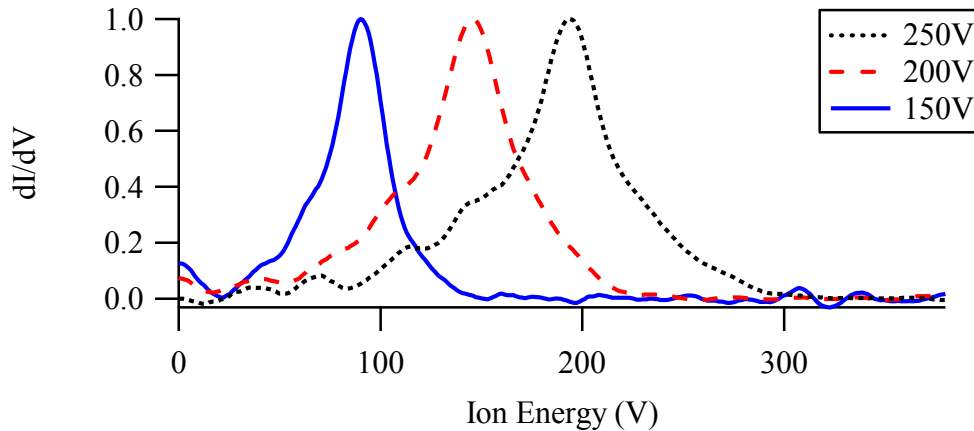


Figure 107. Normalized ion energy distribution function for xenon at 20 A with Floating electrodes at thruster centerline.

Figure 108 compares the energy distributions at each discharge voltage for all three electrode conditions: Floating, 10 V_e , and 30 V_e . As with the low current data, the

electrodes cause an increase in the ion energy. Figure 109 shows the most probable ion energy for all high current cases. Finally, Figure 110 shows the change in ion energy going from Floating to 10 V_e , and Floating to 30 V_e . The energy increase at each electrode step is in line with the additional potential from the electrodes. At 10 V_e the electrodes seem to add more than their full potential to the ion energy. The extra is assumed due to measurement error. At 30 V_e the electrodes contribute 2/3 of their potential to the ion energy, similar to what is seen at low current. At high current, the electrodes only seem to contribute to ion acceleration. The low ion energy gain seen for 9 A at 10 V_e does not occur here. The two mode operation seen at 9 A is not present at 20 A.

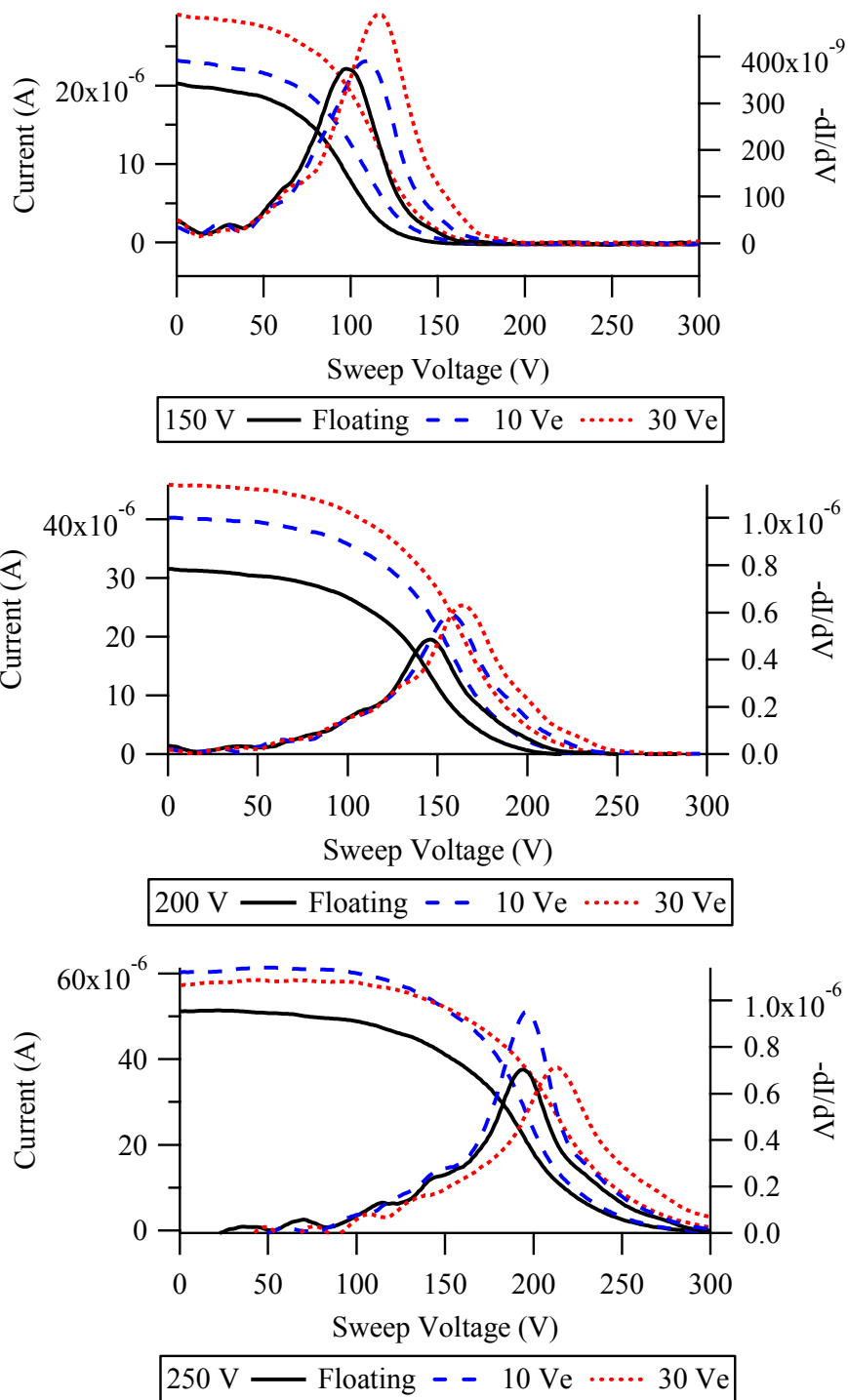


Figure 108. Ion energy distributions for the conditions tested at 20 A showing the three electrode conditions: Floating, 10 Ve, and 30 Ve.

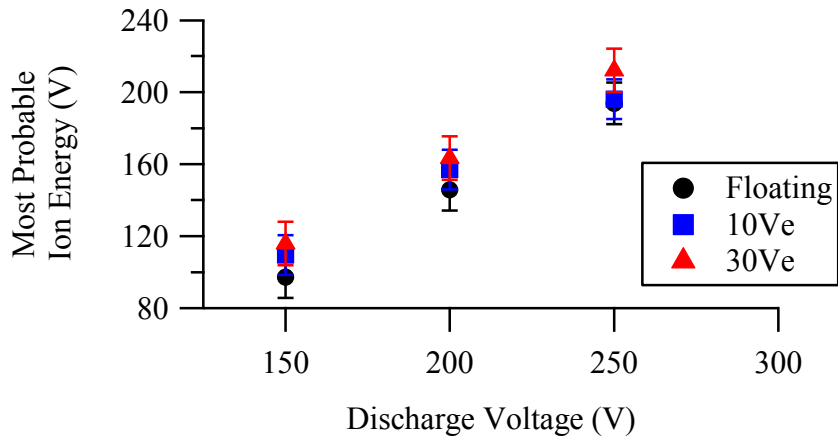


Figure 109. Most probable ion energy for xenon at 20 A. The data is less clear for the 20 A case. There is no definite jump in ion energy as was seen at 9 A.

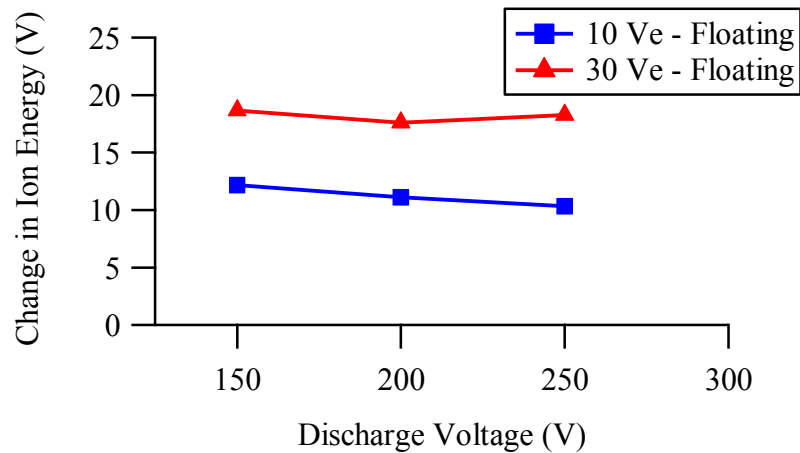


Figure 110. Change in most probable ion energy with the electrodes.

6.2.4 Far-Field Plasma Potential

Plume plasma potential is also measured for the 20 A case and shown in Figure 111. The behavior is the same as seen in the 9 A data. The increase in potential by the electrodes is most prominent at low voltages. The centerline potential is affected more than the plasma at larger angles. The behavior is largely the same as for the 9 A low current data.

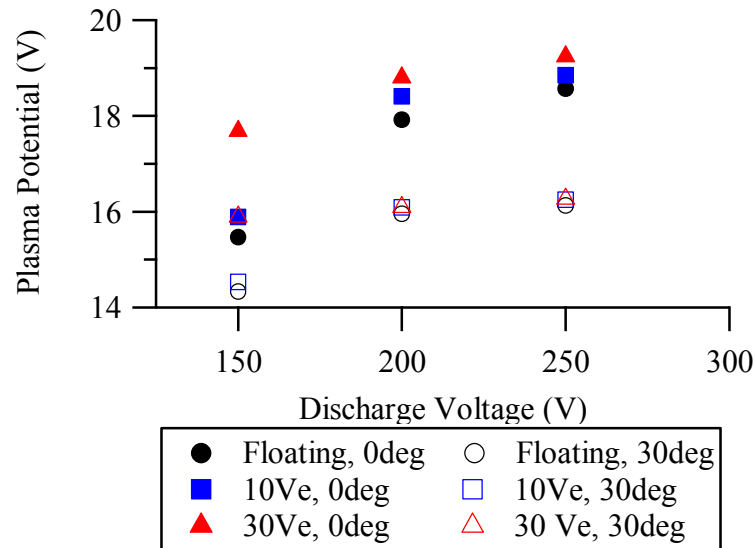


Figure 111. Plume plasma potential for Floating, 10 V_e , and 30 V_e at 0 and 30 degrees.

6.3 Summary

The EEHET has been tested at various conditions at 9 and 20 A discharge current on xenon propellant. The majority of the testing was performed at the lower current of 9 A. Performance measurements at 9 A showed clear improvements to the thruster performance including T/P ratio. The T/P increase is only evident at low electrode potentials. At the higher potential, there is a drop in T/P due to increase power draw by the electrodes. At 10 V_e the electrodes contribute little to ion acceleration, but still demonstrate improvements to performance and plume characteristics. The ion density profile indicates ions are moved from the wings toward centerline. The ion beam current also increases without a corresponding increase in neutral flow rate. Internal plasma potential measurements show little change in the potential range and the acceleration length. The high potential region does expand to cover a larger section of the channel area however. There is a slight pocketing of the high potential regions due to the presence of the electrodes and the cusp magnetic fields.

At 30 V_e there is also a focusing of the ion beam and increased beam current, but the electrodes cause a large increase in ion acceleration. The ion energy increased by an average of 20 V over the Floating case. This extra acceleration must come from the higher voltage electrodes. The closed, domed potential contours around the electrodes are also more defined at 30 V_e. The resultant electric fields due to the domed regions will have a focusing effect. The sudden gain in ion energy at this condition is likely related to a shifting of discharge current from the anode to the electrodes at 30 V_e. At the higher electrode potential, the electrodes collect nearly the entire 9 A discharge current, leaving 1 A or less on the anode.

At 20 A discharge current, there are small performance gains including in *T/P* ratio. However the gains are small relative to the increased current. It was assumed there would be a large increase in the performance gain due to the increased ion density. However due to the magnetic field problem, the thruster likely did not perform as well as could. The plume measurements also show different behaviors than that seen at 9 A. The ion energy results indicate that the electrodes are only contributing to ion acceleration. There may indeed be little to no focusing occurring at these conditions. The electrode current does not experience a sudden jump from 10 to 30 V_e as seen in the 9 A condition.

CHAPTER 7

DISCUSSION OF ELECTRODE EFFECTS

The results with the embedded electrodes produced the expected performance improvements. Other unexpected behaviors were observed as well. This chapter discusses the causes for the performance improvements and the effect of the electrodes on the plasma. The analysis focuses on the 9 A xenon results as those are the most extensive and complete. A short discussion of the 20 A data is also presented.

7.1 Increased Ionization

The plume ion density results from Section 6.1.2 indicated increased beam current, thus increased ion number density with biased electrodes. There are two primary methods to increase ion number: reduce neutralizations, or increase ionization. Ionization will be considered first. To determine the level of ionization, knowledge of the ionization states in the plume is ideally need. However such data is not available, but a qualitative analysis can be done by considering the number of ions per neutral. Figure 112 plots the propellant efficiency which is defined simply as the measure beam current from the Faraday probe divided by the total mass flow rate, shown in Equation 7-1.

$$\eta_p = \frac{I_b}{\dot{m}_{tot}}$$

Equation 7-1

This normalizes the beam current to account for varying flow rates. The thruster exhibits increased propellant efficiency with electrodes which indicates an increase in the number of ions. The three ways ionization can increase the ion number density are

increased neutral density, increased neutral residence time, or increased ionization fraction. The first method, increased neutrals density, can be ruled out by virtue of constant or decreased total mass flow with increased electrode bias. Figure 113 shows the total mass flow, anode plus cathode, for the Floating, 10 V_e , and 30 V_e conditions tested. Table 7 in the appendix lists the individual anode flow rates without the constant cathode flow rate. With a few exceptions, in order to maintain constant discharge current, the mass flow rate decreased or remained constant. This means the ion number density increased without a corresponding increase in propellant neutral density. This rules out increased neutral density as a cause for increased ion density.

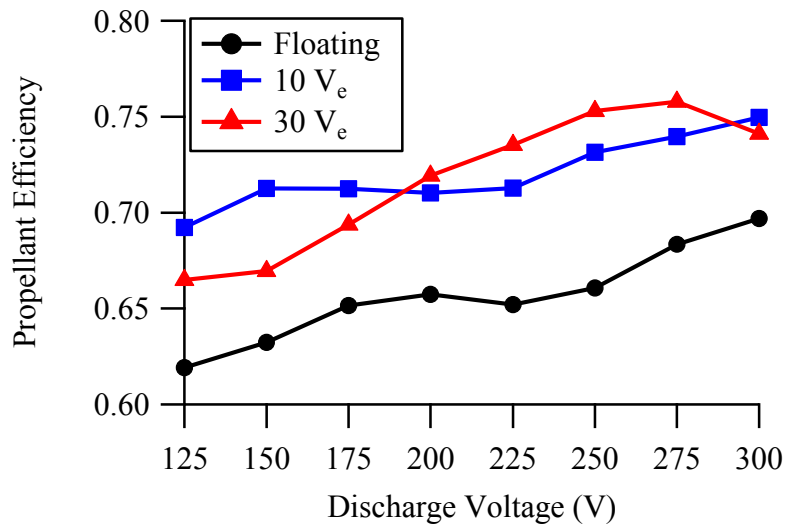


Figure 112. Propellant efficiency defined as beam current/total mass flow rate.

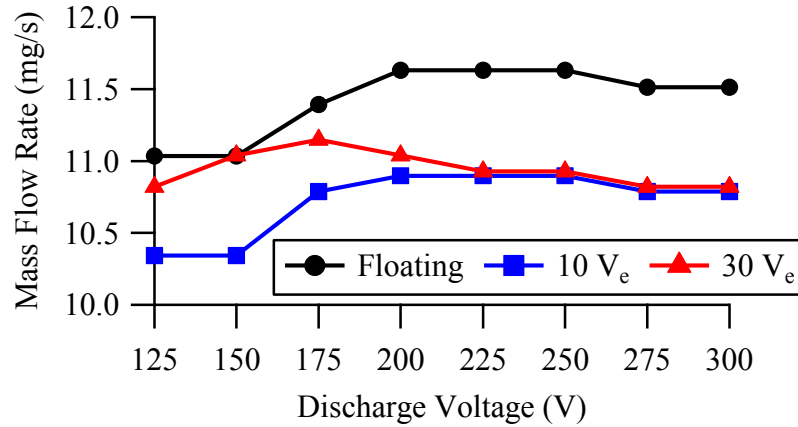


Figure 113. Total mass flow rate including cathode flow. There is an overall decrease in mass flow rate with increased electrode bias.

A second possible cause of increased ionization due to neutrals is increased neutral residence time. The neutral residence time is a measure of how long particles stay in the ionization region and is on the order of the ionization MFP. It is determined by the neutral temperature, which is related to the propellant distributor, or anode temperature. At 30 V_e, the discharge current is primarily on the electrodes, which reduces anode current. By pulling current from the anode, Ohmic heating and thus anode temperature is decreased. In turn the lower temperature reduces the propellant thermal velocity and can cause increased residence time, which can cause increased ionization and beam current.[83] Massey *et. al.* showed that a 50° C decrease in anode temperature is possible with a ~4.5 A decrease in anode current.[84] At 30 V_e there is a shift of ~9 A of current from the anode, which can result in a large temperature drop. However, in all previous experiments with cooling the anode, very little or negative performance changes were seen.[29, 83, 84] The results of the work showed noticeable performance gains beyond the measurement uncertainty at both electrode voltage levels. This suggests increased neutral residence time may play some small part in the increases in propellant efficiency, but may not be a significant effect.

One explanation for the small changes is the assumption that neutral temperature is primarily based on anode temperature. Neutrals from the propellant tank are heated by collisions with hot surfaces, which are the anode and channel walls. The channel wall temperature is nominally correlated to the ion and electron energies. If the electron temperature is constant, the wall temperature should not change much. Thus even if the anode is cooler, the neutrals may still have high temperature due to wall collisions. The last way to increase ion density is through an increased ionization fraction. Normally this effect can be studied using an ExB probe to determine the ionization states and the ionization costs.[80] Unfortunately such data is not available here. An analysis of the effect of ionization fraction can be done by comparing the change in propellant efficiency for the Floating versus the biased electrode cases. Figure 114 compares the change in propellant efficiency for the 25 V increases in discharge voltage in the Floating case, to the 10 and 30 V increases in electrode voltage for the electrode cases. For example, in the Floating case, the change in propellant efficiency when going from 125 – 150 V_d is 0.013, and from 150 – 175 V_d is 0.019. For the electrode cases, the change shown in the figure is between the biased and Floating cases. For example for 125 V_d and 10 V_e , the propellant efficiency increases by 0.062 over the 125 V_d Floating case. At 150 V_d and 30 V_e , the propellant efficiency of the biased electrode case is greater than the Floating case by 0.058. Table 2 lists more examples.

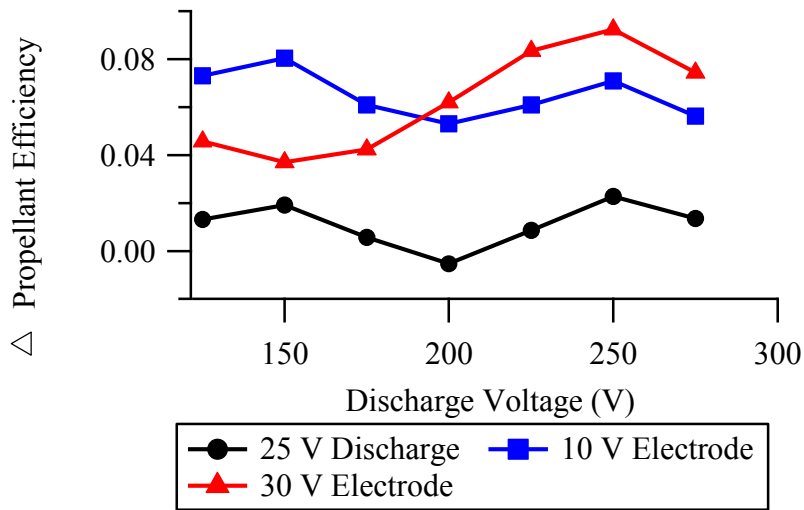


Figure 114. Change in propellant efficiency comparing 25 V discharge increase from floating to 10 and 30 V_e electrode increase.

Table 2. Select data points from Figure 114. The Anode (25 V) column shows the increase in propellant efficiency for a 25 V increase in anode potential from the Floating data. E.g. for a 25 V increase from 125 – 150 V_a , there is a 0.019 increase in propellant efficiency, but a 0.062 increase with 10 V increase on electrodes.

V_d	Anode (25 V)	10 V_e	30 V_e
125	0.019	0.062	0.058
150	0.040	0.049	0.044
200	0.0078	0.029	0.047
250	0.0017	0.019	0.057

This data shows that a 10 or 30 V increase in electrode potential causes a larger increase in propellant efficiency than a 25 V increase in anode potential. Increased anode potential increases the electron temperature, which increases the ionization rate. These results suggest that increasing the electrode potential by 10 or 30 V over the anode potential has effects other than increased ionization rate. There is a secondary effect causing the increased ion number density with biased electrode, which is believed to be ion-wall repulsion, or ion focusing, that increases ion number density by reducing the

amount of ions lost to wall neutralizations. This is more likely to be true for 10 V_e as improvements are seen in performance and propellant efficiency without large changes in ion energy or plasma potential. For the 30 V_e case, the plasma potential increased significantly, possibly causing an increased ionization rate.

7.2 Thruster Acceleration Region

The increased potential range within the discharge channel is largely due to increased maximum potential. At the downstream end of the measured region, the minimum potential is relatively constant around 70 V. Likewise in the far-field the plasma potential is very similar between the three electrode conditions as can be seen in Figure 96. The largest increase is 0.78 V from Floating to 30 V_e . The increase in maximum potential near the anode without a similar increase in minimum potential results in an increased potential drop and slope. Figure 115 shows the centerline plasma potential measured with the miniature emissive probe from the near anode region to multiple channel lengths downstream. The Floating and 10 V_e cases have nearly identical potential profiles while the 30 V_e profile shows increased maximum potential, but similar far-field potential. This creates a steeper potential profile slope.

One effect of the sharper potential drop at 30 V_e is a shorter acceleration region. The acceleration region is the axial length where the majority of the potential drop occurs and ions are accelerated by the electric field. The acceleration region can be determined from the plasma potential or electric field. Looking at the centerline plasma potential shown in Figure 115, the acceleration region is taken to be between 90 % and 10 % of the total potential drop. From the electric field profile shown in Figure 116, which is simply

the derivative of the potential, the acceleration region is taken to be between $0.15 E_{\max}$ on either side of the peak. The same analysis has been used by Linnell [73] and Reid [51].

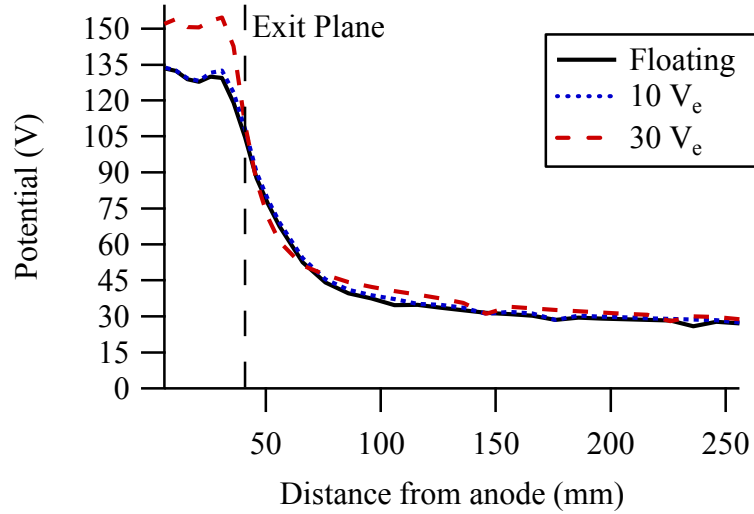


Figure 115. Centerline plasma potential for Floating, 10, and 30 V_e on xenon at 150 V_d .

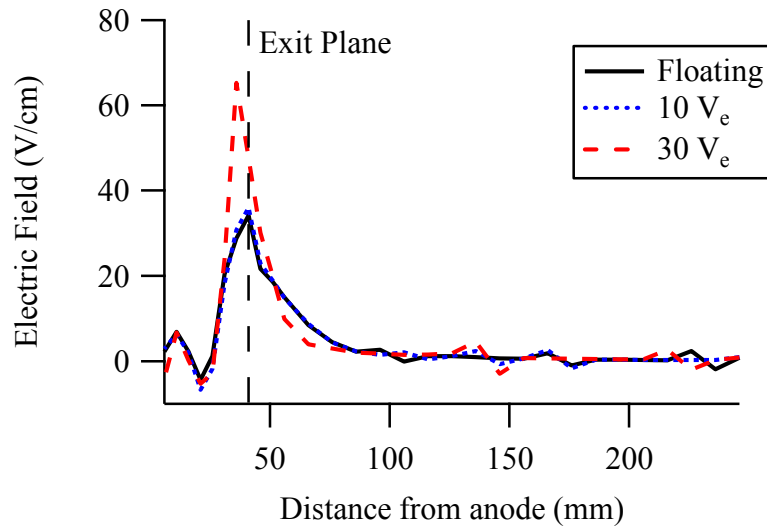


Figure 116. Centerline electric field for Floating, 10, and 30 V_e .

The acceleration region length calculated with the two methods is shown in Table 3. Both methods largely agree on the start and end of the acceleration regions for the Floating and 10 V_e cases. The electric field method gives a longer acceleration region. At

30 V_e though, the two methods give very different values for the acceleration length. The electric field method predicts a much shorter acceleration region. This is due to the high maximum electric field at 30 V_e which causes the 0.15 E_{max} value to be larger and results in a smaller range. If we use the 0.15 E_{max} value from 10 V_e , the acceleration length at 30 V_e becomes 41 mm, which is closer to the potential calculated length of 44.46 mm.

Table 3. Acceleration region locations as distance from the anode measured along channel centerline for Floating, 10 and 30 V_e .

	Floating	10 V_e	30 V_e
Potential			
Accel Start (mm)	34.01	35.87	36.38
Accel End (mm)	82.59	83.83	80.84
Accel Length (mm)	48.59	47.96	44.46
Electric Field			
Accel Start (mm)	32.03	32.81	33.37
Accel End (mm)	84.30	83.78	66.17
Accel Length (mm)	52.26	50.98	32.80

Whichever method is used, the acceleration region shrinks with increased electrode potential especially at the higher electrode voltage. In theory, the length of the acceleration region should not affect the ion acceleration mechanism. However in reality there are a number of factors that can interfere with ion acceleration. The downstream potential contours are the same for all three cases, thus the electric fields are similar. The electric fields diverge downstream of the channel exit, and can cause plume divergence. A long acceleration region will cause more divergence as ions follow the electric field further out and gain more radial velocity. A long acceleration region also increases the chances of ion collisions with other particles that can cause charge exchange or neutralization. Overall, a shorter acceleration region results in better performance.

7.3 Electron Temperature

The electron temperature is obtained from the floating and plasma potential according to Equation 3-17. The calculated electron temperature contours for the three electrode conditions are shown in Figure 117. The contours are not perfectly symmetric with respect to the centerline due to uncertainty in the measurement and due to the fact the HET cannot be truly 2D symmetric due to the annular configuration. For example, the magnetic flux density will be larger at the inner wall than outer wall because of the smaller inner wall area. The electron temperature is highest near the channel exit where the radial magnetic field peak is located. The area of highest temperature is typically associated with the Hall current and the ionization region. The maximum electron temperature increased with electrode bias. From Floating to 10 V_e the temperature increased by only 1 eV from 20 to 21 eV. This small increase in temperature and thus electron energy indicates very little change in the electron population. The observed improvements in thrust and ion number density at 10 V_e are thus not due to more energetic electrons significantly improving the ionization rate, further confirming the propellant efficiency results from Section 7.1.

At 30 V_e the maximum electron temperature is 28 eV, an increase of 8 eV over the Floating case. Using the same calculation for ionization rate from Section 4.4.1, a temperature of 20 eV gives an ionization rate constant of $1.69 \times 10^{23} \text{ m}^{-3}\text{s}^{-1}$, and $2.39 \times 10^{23} \text{ m}^{-3}\text{s}^{-1}$ for 28 eV. This is a 40% increase in the ionization rate constant. As suggested previously, at 30 V_e increased ionization is a very likely the cause of the increased ion number density.

A second possible effect of the increased electron temperature is increased electron gyroradius along magnetic field lines. The electron temperature near the

electrodes also increases noticeably from Floating to $30 V_e$. This causes an increase in the electron thermal velocity. For a constant magnetic field, as done in this work, the increased velocity will increase the Larmor, or gyroradius according to Equation 1-5. An increased gyroradius means the electrons are not as well magnetized and trapped by the magnetic field lines, thus an increase in the cross-field mobility and electron current is possible. Comparing the gyroradius near the electrodes for a 7 eV electron (Floating) to 10 eV ($30 V_e$), the gyroradius increases from 0.25 to 0.3 mm assuming a 250 G magnetic field. This increase is small, but may play a minor role in the high electron current seen at high electron bias.

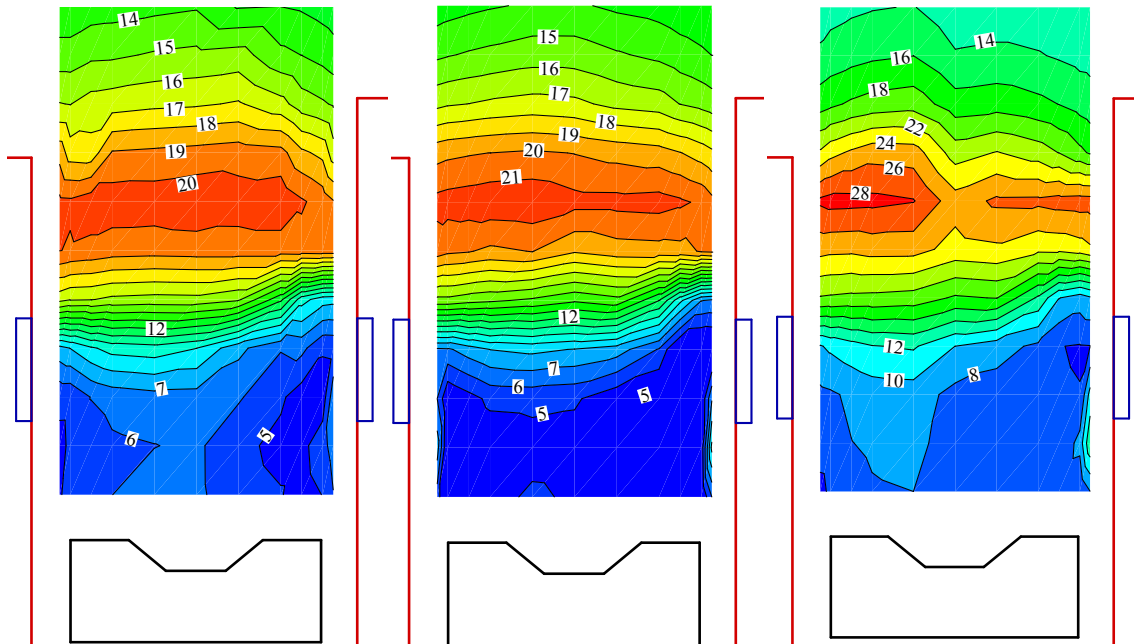


Figure 117. Electron temperature in the discharge channel for Floating, 10, and $30 V_e$.

7.4 Behavioral Differences with Electrodes

The analysis of the data has indicated two different modes of interaction between the electrodes and plasma. At $10 V_e$, the electrodes increase ion density through focusing.

At 30 V_e the electrodes contribute to ion acceleration and electron temperature. The causes for these different behaviors can be traced to the electrode current reproduced below in Figure 118. The current is quite different between the two bias levels. Since the electrodes are connected to the anode power line, they share current with the main anode. This means at 30 V_e , when the electrodes draws 9 A of current, the anode has very little current. This response is similar to the behavior seen on krypton propellant. The full discharge current on the electrodes may cause the electrodes to act as the primary anode. The anode never reads zero current however. Some current recycling occurs between the electrode and anode within the circuit as the discharge power supply current is held at 9 A.

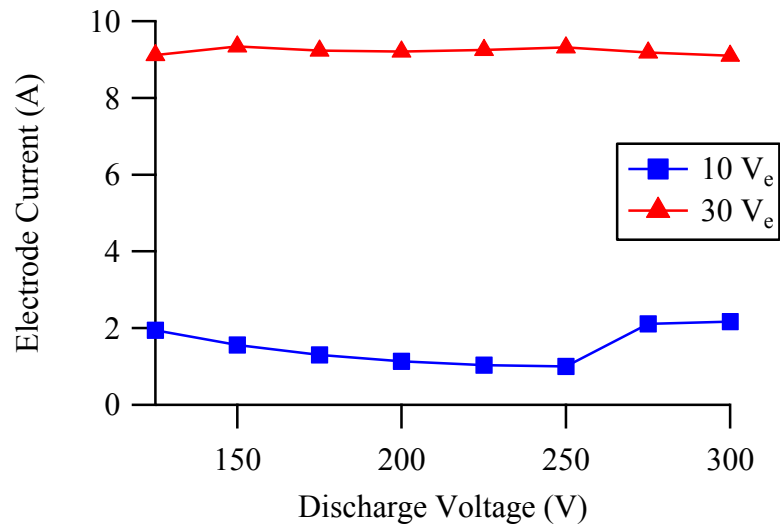


Figure 118. Electrode current at 9 A for 10 V_e and 30 V_e electrode bias. Similar to the krypton tests, the electrodes draw in almost all of the current at 30 V_e .

It has been shown that the ion energy distribution functions increases as the electrode bias increases. Figure 93 showed the most probable ion energy for the various test conditions. At 10 V_e , the increase in ion energy is small, a maximum of 6.3 V for the 125 V_d case, but at 30 V_e the increase ranges from 19 to 25 V. Though the increase in ion

energy is small at $10 V_e$, combined with the decrease in divergence angle it results in a significant increase in thrust and T/P ratio over the floating case (up to 7.6 mN and 4.2 mN/kW improvement). At $30 V_e$ the thrust increases even more (up to 13.7 mN), however the marked increase in collected current leads to a reduction in the T/P ratio (loss of 1-3 mN/kW). Thus the shifting of the current, thus the primary positive terminal is the causes of the different behavior between 10 and $30 V_e$.

7.5 Near-Wall Sheath Behavior

An area of interest of this work with the electrodes and the shielding cusp fields is the interaction of the magnetic field with the near-wall plasma sheath. The plasma sheath is a thin region of plasma the surrounds any surface exposed to the plasma whether it be insulating or conducting. For an insulating surface, the sheath exists due to the different velocities of electrons and ions as discussed previously. As the insulating surface will float to a potential less than the plasma potential, an electron repelling sheath, or potential drop, forms to maintain a monotonic sheath potential drop from plasma potential to wall potential.

For a conducting surface, such as the biased electrode configurations, the sheath around the electrode becomes controlled by the need to balance the electron current into the electrodes. For the case here, a positively biased electrode, the sheath formed is typically still an electron repelling sheath. In most cases, the electron flux is higher than necessary for the discharge, thus an electron repelling sheath develops to reduce the flux. A larger disparity requires a thicker and stronger sheath. It is also possible to have an electron attracting sheath if the thermal flux is insufficient to maintain the discharge current. This situation occurs in cases with electrodes too small for sufficient flux.[85,

86] Between the two sheath types is a no-sheath regime where the flux equals the discharge electron current.

Another method to control the electron flux to electrodes is with magnetic fields, specifically fields parallel or at small angles to the electrodes. The cusp fields that surround the wall electrodes in this work are one such example. The presence of strong magnetic fields can magnetize electrons, reducing their mobility and flux toward the electrode. This in effect performs the function of an electron repelling sheath, and can reduce or remove the sheath thickness. Magnetization of electrons occurs if the electron Hall parameter, Ω_e , is much larger than unity.

$$\Omega_e^2 = \frac{\omega_e^2}{\nu_e^2} \gg 1$$

Equation 7-2

Here ω_e is the electron gyro frequency, and ν_e is the electron collision frequency. The gyro frequency and collision frequency are:

$$\omega_e = \frac{qB}{m}$$

Equation 7-3

$$\nu_e = 2.91 \times 10^{-6} n_e A T_e^{-3/2}$$

Equation 7-4

where q is the particle charge, B is the magnetic field in Tesla, m is the electron mass, n_e is electron density in cm^3 , A is the Coulomb logarithm taken as 10 for this first order analysis, and T_e is the electron temperature in eV. The magnet field strength of the cusps 3 mm from the surface, approximately where the closest probe data is taken, is ~ 250 G.

The channel electron density can be calculated from Equation 4-7. For the 150 V_d case, this yields an electron density between 1.76 and 1.82 x 10¹⁷ m⁻³.

The average electron temperature near the electrodes is 10 eV. The resulting electron Hall parameter squared is 164, which means the electrons are magnetized. The electron temperatures are similar for the other electrode cases tested, thus electron magnetization would occur for all cases, BN to 30 V_e. This leads to the conclusion that the sheath should be strongly affected by the cusp magnetic field.

The magnetization of the electrons causes a reduction of electron flux to the electrodes. This can be seen from a plot of cusp magnet current versus the electrode current as shown in Figure 119 for 175 V_d and 10 V_e electrodes.

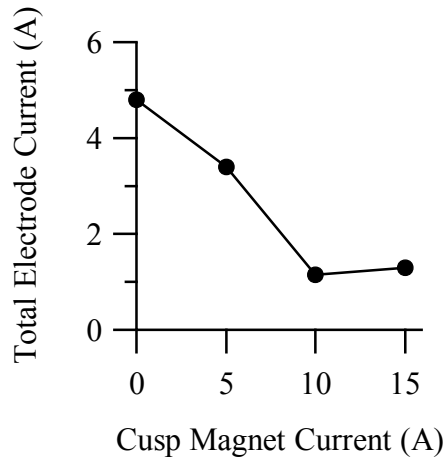


Figure 119. Electrode current for increasing cusp-magnet currents for 9 A on xenon at 175 V_d, 10 V_e. Higher magnetic current results in stronger cusp fields, which reduces electron flux to the electrodes.

The decreased electrode current means there is a decrease flux of electrons. This behavior suggests that the sheath shrinks in size as the electron flux to the electrodes is reduced by the magnetic fields. It was also observed that an increase in one cusp magnet, the inner or outer, caused a drop in the associated electrode current, and increase in the other. For example, an increase in the inner cusp magnet strength decreases the inner

electrode current but increases the outer electrode current. However, the total electrode current remained nominally constant. The mass flow and discharge voltage were held constant, thus the shifting of currents is due to changing magnetization of electrons around one electrode, causing the other electrode to draw more current to maintain the discharge. This would mean the inner and outer electrode sheaths grow and shrink in a dependent fashion, which is logical given they are both tied into the same electric circuit. These results show that cusp-fields can strongly influence the near-wall sheath and may be used as a controller for electron fluxes to surfaces.

7.6 Performance Improvements

The theoretical analysis of ionization, electron-ion recombination, and ion-wall neutralizations in Section 4.4 showed that 13% of the ions are lost to wall neutralizations, for the conditions of this thruster. Electron-ion recombinations are a negligible contribution to ion losses in the thruster, accounting for only 2×10^{-15} A of ion current. This means reducing ion-wall losses can increase thruster performance. The propellant efficiency (ions per unit propellant) at 10 and 30 V_e increased over the Floating case by 2.7% and 14%. These values are on par with the predicted ion loss from wall neutralization, though there is some contribution from an increased ionization rate as discussed previously, which cannot be separated out given available data.

The performance results have shown that the electrodes are able to increase the performance, especially the T/P ratio with only a minor power draw at 10 V_e . The increase in T/P ratio over the Floating case is 4.6 mN/kW, which is an 8.1% improvement. The same 10 V_e condition had gains in thrust (10%), I_{SP} (17.4%), and efficiency (27%). An increase in thrust can generally be attributed to either increased exit

velocity (ion energy), or increased mass flow (number density). The plume measurements show there is an increase in the ion beam current with electrodes, thus an increase in the ion number density that exits the thruster. RPA data also shows increased ion energy, especially at 30 V_e . An analysis of these two sources will determine their thrust contributions.

The measured beam current can be converted into an ion mass as each ion carries a charge of 1.6×10^{-19} C, and xenon ions have a mass of 2.18×10^{-25} kg. The ion velocity is calculated from the acceleration voltage obtained from the centerline potential profile. Table 4 shows the velocity and mass values for the 150 V_d case with all three electrode conditions along with the thrust caused by the changing velocity and mass. The thrust due to increased velocity is determined by multiplying the difference in exit velocities at 10 and 30 V_e by the Floating ion mass. The thrust from increased ion number density is determined by multiplying the increase in mass at 10 and 30 V_e by the Floating ion velocity.

Table 4. Comparison of thrust improvements from increase ion number (mass) and increase ion energy (velocity) for the EEHET at 150 V_d , 9 A on xenon.

	Floating	10 V_e	30 V_e
Acceleration voltage (V)	102.6	102	118
Exit velocity (m/s)	12269	12238	13261
Ion mass exiting (kg)	9.51E-06	1.004E-05	1.007E-05
Measured thrust (mN)	76.3	83.99	91.6
Δ velocity from Floating (m/s)		-31	992
Δ ion mass over Floating (kg)		5.339E-07	5.605E-07
Thrust from Δ velocity (mN)		-0.31	8.48
Thrust from Δ mass (mN)		6.55	6.88

The results show that at 10 V_e , all of the additional thrust is from increased ion number density. At 30 V_e , about 45% is from ion number density, the rest is due to

increased acceleration. The 30 V_e condition had overall very little additional increase in the ion number density compared to 10 V_e . This suggests that the electrode presence causes the increased number density as the increase in number density is similar at both bias levels. The increase in thrust from 10 to 30 V_e is thus due to increased acceleration as the electrodes become the main positive terminal.

7.7 High Current Discussion

The high current operation of the EEHET showed many of the same trends and behaviors as low current operation. The performance changes due to the electrodes are smaller, and at times inconsistent. This is attributed to the constant magnetic field used in this work. The magnetic field is kept the same at the 9 A case to maintain the designed field topology. Unfortunately this results in an underpowered field. The magnetic fields are unable to perform as well at 20 A compared to 9 A. It is likely there is less focusing or wall repulsion occurring at this operating condition.

The decrease in focusing can be seen from the change in ion energy shown in Figure 110. Both the 10 and 30 V_e measurements show large increases in ion energy at all discharge voltages. In the low current case, there is only a small increase in ion energy at 10 V_e , the rest of the energy being used for focusing. There is also an observed increase in ion energy from high to low voltages at 9 A. The 20 A data shows a nearly flat ion energy increase for both electrode bias levels. More extensive testing is needed to determine the electrode effectiveness at high currents.

7.8 Summary

The analysis of the data shows that the electrodes have two different behaviors depending on the bias and collected current. At 10 V_e where increased T/P was seen,

there was little contribution to ion acceleration from the electrodes. At this condition, the increased ion number density provided all of the thrust improvements measured. At $30 V_e$, the electrodes collected the majority of the discharge current and became the dominant electrode. The subsequent thrust improvement is caused by both increased ion number density and increased ion acceleration. The increase in ion number density in both cases is very similar. However the $30 V_e$ case showed marked increase in electron temperature, which can cause the ion number density increase. The increase in ion number density varies from 1 – 8%, less than the 13% loss to wall neutralization predicted by the equations, but it is not realistic to expect full prevention of wall losses.

The cusp-fields also play an important role in this work as they influence the near-wall plasma sheath, and the interactions may play a part in the behavior of the electrodes and plasma. The electron flux to the electrodes can be reduced with stronger fields due to magnetization of electrons, which causes shrinkage of the sheath.

CHAPTER 8

CONCLUDING REMARKS

This dissertation studied the feasibility of using in-channel electrodes to increase the T/P ratio in HETs through ion focusing and reduced ion-wall neutralizations. This work contributed a new modification to HETs that has been shown to increase the performance, and insight into the interaction between wall electrodes and the plasma. The magnetic field is redesigned to provide shielding for the electrodes. The major conclusions of this research are summarized in the following sections, and suggestions for future work are presented.

8.1 Electrode Behavior and Effects

The electrodes were added with the goal of ion repulsion through strategic electric field placement. The results show there are likely two different modes of electrode behavior. At $10 V_e$, the increased performance is due to increased ion number density, not increased acceleration. Measurements of the channel potential profile showed little change in the acceleration region of the thruster, thus little increase in ion energy. The increase in density is not attributed to increased ionization because the electron temperatures at $10 V_e$ are only 1 eV higher than the Floating condition, which adds very little to the ionization rate. Plume profiles also show that ions are focused towards the centerline. The data supports the theory of ion focusing and reduced ion wall losses at $10 V_e$.

At $30 V_e$, there is also an increase in ion density. However the electron temperature is noticeably higher, by 8 eV, thus increased ionization likely plays some

part in the increased density. The higher temperature could also increase electron mobility through increased gyroradius, however for these temperatures the changes to gyroradius are small. Ion acceleration also increased at this condition, and contributed significantly to the increased performance. Analysis of the acceleration region showed increased acceleration potential and shortened region length. The potential contours also changed significantly at 30 V_e with the creation of high potential domed regions around the electrodes. The regions correspond to the cusp-magnetic fields, and create focusing electric fields which likely are the cause of the observed decreased plume angle. The domed regions only occur with biased electrodes. In the Floating case, the cusp-magnetic fields do not appear to affect the potential contours to any degree. A possible cause of this behavior is the interaction of the cusp-field with the near-wall plasma sheath which can cause electrons to become trapped on the cusp fields as they attempt to reach the electrodes. With biased electrodes drawing a larger electron current, the cusp magnetic fields may segregate the electrons based on energy, thus forming the contours.

8.2 Increase in Thrust-to-Power Ratio

The analysis of ionization and ion loss showed that 13% of the ions are lost to wall neutralizations while electron-ion recombinations are a negligible contribution. The propellant efficiency (ions per unit propellant) exhibited an increase over the Floating case of 12.7 % at 10 V_e and 14 % at 30 V_e . The performance results have shown that the electrodes are able to increase the performance, especially the T/P ratio with only a minor power draw at 10 V_e . The increase in T/P ratio over the Floating case is 4.6 mN/kW, which is an 8.1% improvement. The same 10 V_e condition had gains in thrust (10%), I_{SP} (17.4%), and efficiency (27%). The thruster did not perform as well at 30 V_e . At the

higher electrode voltage, more thrust is seen, however a large increase in power draw resulted in an overall drop in T/P ratio. The results from high current operations also showed T/P ratio improvements, but the gains are lower than expected, likely due to the constant magnetic field being underpowered. The performance results prove the use of positively biased electrodes have a beneficial effect on the performance of HETs.

The demonstrate performance improvements with biased electrodes are a large fraction of the baseline Floating case. However the baseline performance is only moderate compared to the current state-of-the-art HETs. This can be due to factors such as the changed magnetic field. The question then becomes is this technique applicable to any thruster. If the same percent improvements can be applied to modern high performance thrusters, then this technique can have a large impact on HET performance and allow for faster high thrust orbit maneuvers.

8.3 Future Work

The research presented in this thesis showed that the addition of in-channel embedded electrodes can improve the thruster performance. There are still many questions unanswered as a result of this work.

8.3.1 Magnetic Field Considerations

The cusp magnetic fields are a change to the standard HET field design. They were added to reduce electrode current, and appear to be responsible for the creation of the high potential dome contours near the electrodes. However, the divergence from the standard field design may also cause lower overall performance. The behavior of the electrodes without the cusp field would be an interesting study. This would determine

how critical the cusp-fields are to the generation of the focusing electric field, and allow cross analysis of the plasma sheath behavior with and without a near wall magnetic field.

A second area of investigation related to the magnetic field design is to operate the EEHET as it currently exists with an optimized magnetic field. As noted in the high current results, not optimizing the magnetic field likely caused lower performance due to inadequate electron magnetization. However optimizing the field, by changing magnet currents, can cause unshielding of the electrodes. This would cause the electrode current to increase, however this may not necessarily cause a performance loss. This would also help answer the previous questions of how necessary are the cusp fields to the observed effects.

8.3.2 Electrode Placement

A third area of study is the placement of the electrodes. As discussed, the wall ion density is highest near $0.15 L_C$ and drops to zero around $0.5 L_C$. Even though the electrodes in this work were placed at $0.5 L_C$, upstream of the high density zone, noticeable changes to thruster behavior were still observed. By moving the electrodes further downstream, it may be possible to increase the performance gain due to the high ion density near the wall that can be repelled, thus further reducing ion-wall losses. There is the issue of interference with the Hall current and plasma lens, being near the region of high density should further reduce the ion-wall losses. This would contribute to the understanding and effectiveness of ion-wall repulsion.

8.3.3 Plasma Sheath

A topic regrettably not studied in this thesis is the near-wall plasma sheath around the electrodes. The sheath exists in order to balance the electron current into the

electrodes. In the standard case, the sheath is electron repelling because the thermal flux of electrons is greater than the current needed. The presence of the cusp-magnetic field complicates the issue. The magnetic fields magnetize electrons, thus contributing to the reduction of electron flux to the electrode. This may cause the sheath to become thinner or have lower repulsion potential. At high enough electrode current, it may be possible to have an electron attracting sheath. In this case, the sheath potential is now above plasma potential and increases the electron flux to the surface in order to meet the current requirements. This transition from repelling to attracting sheath is of interest to the plasma propulsion field as it affects all thrusters. This area would benefit from both experimental and theoretical analysis of sheath behavior. Similarly, the sheath behavior at the transition between the insulating wall material and the conducting electrodes warrants investigation. Not only is the method of sheath creation different for these two areas, but the different SEE may also play a part in the sheath behavior.

Lastly, the results seen here open the door for a potential new HET design scheme using staggered wall electrodes and cusp fields. The separation of the high potential regions at $30 V_e$ suggests the possibility of creating cusp shaped contours throughout the discharge channel. Using wall electrodes underneath the cusps, the potential contours may be shaped to provide a highly focused ion beam for high performance HETs.

APPENDIX

Table 5. Operating conditions and data for the initial stainless steel electrode design. The mass flow rate does not include a constant cathode flow rate of 1.11 mg/s.

Discharge Voltage	Electrode Voltage	V_{CG} , V	Anode Mass Flow, mg/s	I_d , A	I_e , A	Thrust, mN	T/P ratio, mN/kW	I_{SP} , s	η_A	P_c , Torr-Kr
300	Floating	-20.3	5.07	9	1	0	27.63	1499	0.203	2.39E-05
275	Floating	-21.3	5.27	9	1.3	0	30.10	1442	0.213	2.28E-05
250	Floating	-22.1	5.47	9.1	1.5	0	32.60	1378	0.220	2.23E-05
225	Floating	-23.2	5.52	9	1.7	0	39.59	1482	0.288	2.28E-05
200	Floating	-23.6	5.62	8.9	1.9	0	41.69	1352	0.276	2.33E-05
175	Floating	-23.7	5.87	9	2.3	0	44.37	1214	0.264	2.33E-05
150	Floating	-23.7	6.12	9	2.4	0	43.52	978	0.209	2.39E-05
125	Floating	-22.3	6.47	8.8	2.6	0	40.33	700	0.138	2.54E-05
125	10	-22.5	6.47	9.2	3.8	0	41.11	767	0.155	2.34E-05
300	10	-20.9	5.07	9	1.3	0	28.33	1545	0.215	2.44E-05
275	10	-20.5	5.27	9	1.6	0	30.39	1464	0.218	2.39E-05
250	10	-22.8	5.47	9	1.9	0	32.93	1389	0.224	1.93E-05
225	10	-23.2	5.52	9	2.3	0	39.14	1482	0.284	1.93E-05
200	10	-23.8	5.62	9	2.7	0	41.58	1383	0.282	1.98E-05
175	10	-23.7	5.87	9.2	3.2	0	43.63	1244	0.266	1.98E-05
150	10	-23.5	6.12	9.2	3.7	0	44.56	1050	0.229	2.24E-05
125	20	-22.8	6.47	9.5	5.7	0	40.95	835	0.168	2.49E-05
300	20	-20.3	5.07	9	1.7	0	28.76	1580	0.223	2.44E-05
275	20	-21.6	5.27	9	2	0	30.07	1464	0.216	2.39E-05
250	20	-22.8	5.47	9	2.4	0	32.52	1389	0.221	1.93E-05
225	20	-23.1	5.52	9.1	2.8	0	38.67	1503	0.285	1.93E-05
200	20	-23.6	5.62	9	3.2	0	41.37	1404	0.285	1.98E-05
175	20	-23.6	5.87	9.3	4.8	0	43.26	1294	0.274	1.93E-05
150	20	-23.6	6.12	9.3	4.9	0	43.27	1074	0.228	2.24E-05
125	30	-23	6.47	9.5	6.6	0	39.52	858	0.166	2.49E-05
300	30	-20.3	5.07	9	2.1	0	28.56	1585	0.222	2.44E-05
275	30	-21.6	5.27	9	2.4	0	27.93	1486	0.203	2.39E-05
250	30	-21	5.47	9	2.9	0	32.60	1416	0.226	1.93E-05
225	30	-23.1	5.52	9.1	3.3	0	37.90	1503	0.279	1.93E-05
200	30	-23.8	5.62	9	4.7	0	40.03	1414	0.278	1.98E-05
175	30	-23.9	5.87	9.3	6	0	41.56	1304	0.266	1.93E-05
150	30	-23.7	6.12	9.3	5.9	0	42.37	1107	0.230	2.24E-05

Table 6. Operating conditions for 9 A EEHET on krypton. The mass flow does not include a constant cathode flow rate of 0.93 mg/s for BN and 1.02 mg/s for rest.

Discharge Voltage, V	Electrode Voltage, V	V_{CG} , V	Anode Mass Flow, mg/s	I_d , A	I_e , A	Thrust, mN	T/P ratio, mN/kW	I_{SP} , s	η_A	P_c , Torr-Kr
300	BN	-25.2	7.36	9.05	0	114.4	42.15	1407	0.291	7.73E-06
275	BN	-24.8	7.44	9.05	0	108.4	43.56	1321	0.282	7.73E-06
250	BN	-24.3	7.44	8.97	0	99.4	44.30	1211	0.263	7.73E-06
225	BN	-23.6	7.51	8.97	0	90.3	44.76	1092	0.240	7.73E-06
200	BN	-22.8	7.65	9.02	0	81.3	45.05	966	0.213	8.77E-06
175	BN	-21.9	7.72	9.02	0	69.3	43.81	816	0.175	8.77E-06
150	BN	-20.4	8.01	9.07	0	57.2	42.20	653	0.135	8.77E-06
125	BN	-19.3	9.00	9.05	0	48.2	42.42	495	0.103	9.28E-06
300	Floating	-23.3	7.24	9.01	0	112.5	41.63	1583	0.323	8.77E-06
275	Floating	-23.0	7.31	9.00	0	107.2	43.26	1494	0.317	8.77E-06
250	Floating	-23.0	7.42	9.00	0	99.6	44.32	1369	0.298	8.85E-06
225	Floating	-22.4	7.53	8.99	0	89.5	44.29	1213	0.263	9.28E-06
200	Floating	-21.7	7.63	9.02	0	79.2	43.95	1059	0.228	1.29E-05
175	Floating	-20.6	7.74	9.04	0	69.8	44.13	920	0.199	1.41E-05
150	Floating	-19.3	8.02	9.00	0	58.9	43.59	749	0.160	1.60E-05
125	Floating	-18.3	9.36	9.01	0	47.5	42.38	518	0.108	2.47E-05
300	10	-21.8	7.28	9.04	0.37	113.2	41.75	1586	0.325	8.77E-06
275	10	-22.0	7.31	8.98	0.44	108.7	43.89	1515	0.326	8.77E-06
250	10	-22.0	7.42	9.03	0.44	102.6	45.38	1411	0.314	8.85E-06
225	10	-21.7	7.49	9.03	0.46	93.6	45.96	1274	0.287	9.10E-06
200	10	-21.0	7.53	8.99	0.47	84.5	46.91	1145	0.263	9.28E-06
175	10	-20.0	7.60	8.96	0.47	73.2	46.57	983	0.224	9.32E-06
150	10	-19.0	7.77	8.96	0.59	63.4	46.77	832	0.191	1.60E-05
125	10	-17.9	8.44	9.04	0.72	50.6	44.36	611	0.133	2.02E-05
300	30	-22.7	7.21	8.95	6.54	112.8	39.19	1597	0.307	8.63E-06
275	30	-22.7	7.28	8.96	6.34	107.2	40.39	1502	0.297	8.78E-06
250	30	-22.5	7.35	8.96	6.54	102.7	42.11	1424	0.294	8.81E-06
225	30	-22.2	7.45	9.05	6.75	94.3	42.15	1290	0.267	9.02E-06
200	30	-21.9	7.53	8.98	7.39	86.8	43.04	1176	0.248	9.28E-06
175	30	-21.4	7.67	9.03	7.77	75.5	41.70	1004	0.205	1.36E-05
150	30	-20.4	7.77	9.04	7.96	66.4	41.57	871	0.178	1.60E-05
125	30	-19.3	8.09	9.01	7.94	52.8	38.54	666	0.126	1.63E-05

Table 7. Operating conditions for 9 A EEHET xenon data presented. Mass flow includes a constant cathode flow rate of 0.97 mg/s.

Discharge Voltage, V	Electrode Voltage, V	V _{CG} , V	Total Mass Flow, mg/s	I _d , A	I _c , A	Thrust, mN	T/P ratio, mN/kW	I _{SP} , s	η _A	P _c , Torr-Xe
300	Floating	-22.7	11.51	9.12	0	151.1	56.19	1339	0.369	5.93E-06
275	Floating	-22.5	11.51	9.03	0	142.0	57.66	1258	0.356	5.93E-06
250	Floating	-21.9	11.63	8.97	0	132.8	59.05	1165	0.337	5.93E-06
225	Floating	-21.3	11.63	8.92	0	122.2	60.04	1071	0.315	6.28E-06
200	Floating	-20.5	11.63	8.93	0	109.2	60.39	957	0.283	7.70E-06
175	Floating	-19.0	11.39	8.98	0	93.2	58.95	834	0.241	7.70E-06
150	Floating	-18.7	11.04	8.90	0	76.3	56.48	705	0.195	6.28E-06
125	Floating	-16.3	11.04	8.93	0	59.5	52.45	550	0.142	7.10E-06
300	10	-22.4	10.79	9.00	2.17	152.7	56.2	1473	0.414	5.93E-06
275	10	-22.3	10.79	8.97	2.11	146.6	58.91	1386	0.400	5.93E-06
250	10	-21.9	10.90	9.10	1.00	142.0	62.74	1329	0.409	5.58E-06
225	10	-21.1	10.90	9.00	1.03	128.3	62.97	1200	0.371	6.28E-06
200	10	-20.0	10.90	9.02	1.13	114.5	62.97	1072	0.331	7.70E-06
175	10	-19.4	10.79	9.02	1.30	100.8	63.15	953	0.295	7.60E-06
150	10	-18.7	10.34	9.08	1.56	83.99	61.08	828	0.248	5.93E-06
125	10	-16.8	10.34	9.00	1.94	65.7	57.29	647	0.182	5.23E-06
300	30	-21.5	10.68	8.98	9.10	158.8	53.74	1517	0.400	5.23E-06
275	30	-21.5	10.79	8.97	9.18	148.1	54.36	1400	0.373	5.23E-06
250	30	-21.5	11.01	9.03	9.32	142.0	56.00	1316	0.361	5.93E-06
225	30	-21.2	11.01	8.98	9.25	131.3	57.09	1217	0.341	5.93E-06
200	30	-20.9	11.01	8.90	9.21	119.1	57.71	1103	0.312	5.58E-06
175	30	-20.1	11.01	8.98	9.23	106.9	57.94	990	0.281	6.28E-06
150	30	-19.0	11.01	8.93	9.34	91.6	55.69	849	0.232	5.93E-06
125	30	-17.8	10.56	8.90	9.12	73.3	52.44	707	0.182	5.23E-06

Table 8. Operating conditions for 20 A EEHET xenon data presented. Mass flow includes a constant cathode flow rate of 1.85 mg/s.

Discharge Voltage, V	Electrode Voltage, V	V_{CG} , V	Total Mass Flow, mg/s	I_d , A	I_e , A	Thrust, mN	T/P ratio, mN/kW	I_{SP} , s	η_A	P_c , Torr-Xe
300	Floating	-21.2	21.69	19.95	0	358.3	59.95	1843	0.542	1.5E-05
250	Floating	-21.4	21.69	19.96	0	317.8	63.70	1634	0.511	1.5E-05
200	Floating	-19.9	20.85	19.98	0	235.3	58.87	1263	0.365	1.4E-05
150	Floating	-17.8	19.90	20.06	0	162.0	53.78	916	0.241	1.2E-05
300	10	-21.7	22.28	20.13	7.07	377.0	61.81	1882	0.570	1.7E-05
250	10	-21.6	21.81	20.09	7.75	320.9	62.73	1640	0.505	1.5E-05
200	10	-20.0	20.97	20.08	8.63	246.2	59.77	1313	0.385	1.4E-05
150	10	-17.9	19.90	19.93	9.30	186.9	60.53	1056	0.314	1.2E-05
300	30	-21.1	22.16	20.13	9.45	380.2	60.86	1909	0.570	1.7E-05
250	30	-20.6	21.57	20.09	9.96	327.2	62.80	1693	0.521	1.4E-05
200	30	-19.5	20.62	20.08	10.15	255.5	60.83	1389	0.414	1.4E-05
150	30	-17.3	19.78	19.98	10.23	180.7	56.83	1028	0.286	1.1E-05

BIBLIOGRAPHY

- [1] Choueiri, E. Y. "A Critical History of Electric Propulsion: The First 50 Years (1906-1965)," *Journal of Propulsion and Power* Vol. 20, No. 2, 2004, pp. 193-203.
- [2] Hofer, R. R., Walker, M. L. R., and Gallimore, A. D. "A Comparison of Nude and Collimated Faraday Probes for Use with Hall Thrusters," *27th International Electric Propulsion Conference*. IEPC-01-020, Pasadena, CA, 2001.
- [3] Mason, L. S., and Jankovsky, R. S. "1000 Hour of Testing on a 10 Kilowatt Hall Effect Thruster," *37th AIAA Joint Propulsion Conference*. AIAA 2001-3773, Salt Lake City, UT, 2001.
- [4] Byers, D. C., and Dankanich, J. W. "Geosynchronous-Earth-Orbit Communication Satellite Deliveries with Integrated Electric Propulsion," *Journal of Propulsion and Power* Vol. 24, No. 6, 2008, pp. 1369-1375. doi: 10.2514/1.35322
- [5] Chen, F. F. *Introduction to Plasma Physics and Controlled Fusion, Vol 1: Plasma Physics*. New York: Springer, 2006.
- [6] Fruchtmann, A., Fisch, N. J., and Raitses, Y. "Control of the Electric-Field Profile in the Hall Thruster," *Physics of Plasmas* Vol. 8, No. 3, 2001, pp. 1048-1056. doi: 10.1053/1.1343508
- [7] Martin, R. H., Farnel, C. C., and Williams, J. D. "Direct and Remote Measurements of Plasma Properties Nearby Hollow Cathodes," *29th International Electric Propulsion Conference*. Princeton, NJ, 2005.
- [8] King, L. B. "Transport-Property and Mass Spectral Measurements in the Plasma Exhaust Plume of a Hall-Effect Space Propulsion System," *Aerospace Engineering*. Ph.D. Dissertation, University of Michigan, Ann Arbor, MI, 1998.
- [9] Rovey, J. L. "2009: The Year in Review," *Aerospace America*. 47, AIAA, Reston, VA, 2009, p. 44.
- [10] Brown, D. L. "Investigation of Low Discharge Voltage Hall Thruster Characteristics and Evaluation of Loss Mechanism," *Aerospace Engineering* Ph.D. Dissertation, University of Michigan, Ann Arbor, MI, 2009.
- [11] Haas, J. M. "Low-Perturbation Interrogation of the Internal and Near-Field Plasma Structure of a Hall Thruster Using a High-Speed Probe Positioning System," *Aerospace Engineering*. Ph.D. Dissertation, University of Michigan, Ann Arbor, MI, 2001.
- [12] Manzella, D. H., Jacobson, D. T., and Jankovsky, R. S. "High Voltage SPT Performance," *37th AIAA Joint Propulsion Conference*. AIAA 2001-3774, Salt Lake City, UT, 2001.
- [13] Mikellides, I. G., Katz, I., Hofer, R. R., and Goebel, D. M. "Magnetic Shielding of the Acceleration Channel Walls in a Long-Life Hall Thruster," *46th AIAA Joint Propulsion Conference*. AIAA-2010-6942, Nashville, TN, 2010.

- [14] Tverdokhlebov, S. O. "Study of Double-Stage Anode Layer Thruster Using Inert Gases," *26th International Electric Propulsion Conference*. IEPC-93-232, 1993.
- [15] Butler, G. W., Yuen, J. L., Tverdokhlebov, S. O., Semekin, A. V., and Jankovsky, R. S. "Multimode, High Specific Impulse Hall Thruster Technology," *36th AIAA Joint Propulsion Conference*. AIAA 2000-3254, Huntsville, AL, 2000.
- [16] Jacobson, D. T., Jankovsky, R. S., and Rawlin, V. K. "High Voltage TAL Performance," *37th AIAA Joint Propulsion Conference*. AIAA 2001-3777, Salt Lake City, UT, 2001.
- [17] Hutchinson, I. H. *Principles of Plasma Diagnostics*. Cambridge: Cambridge University Press, 1987.
- [18] Olsen, J., and Moskowitz, W. P. "Optical Measurement of Acoustic Resonance Frequencies in HID Lamps," *IEEE Industrial Applications Society Annual Meeting*. New Orleans, LA, 1997.
- [19] de Grys, K., Rayburn, C., Wilson, F., Fisher, J., Werthman, L., and Khayms, V. "Multi-Mode 4.5 kW BPT-4000 Hall Thruster Qualification Status," *39th AIAA Joint Propulsion Conference*. AIAA 2003-4554, Huntsville, AL, 2003.
- [20] Hofer, R. R. "Development and Characterization of High-Efficiency, High-Specific Impulse Xenon Hall Thrusters," *Aerospace Engineering*. Ph.D. Dissertation, University of Michigan, Ann Arbor, MI, 2004.
- [21] Manzella, D. H., and Sankovic, J. M. "Hall Thrusters Ion Beam Characterization," *31th AIAA Joint Propulsion Conference*. AIAA 95-2927, San Diego, CA, 1995.
- [22] Fisch, N. J., Raitses, Y., Dorf, L. A., and Litvak, A. A. "Variable Operation of Hall Thruster with Multiple Segmented Electrodes," *Journal of Applied Physics* Vol. 89, 2001, pp. 2040-2046. doi: 10.1063/1.1337919
- [23] Fruchtmann, A., Fisch, N. J., and Raitses, Y. "Hall Thruster with Absorbing Electrodes," *36th Joint Propulsion Conference*. AIAA 2000-3659, Huntsville, AL, 2000.
- [24] Hofer, R. R., Peterson, P. Y., and Gallimore, A. D. "A High Specific Impulse Two-Stage Hall Thruster with Plasma Lens Focusing," *27th International Electric Propulsion Conference*. IEPC-01-036, Pasadena, CA, 2001.
- [25] Pote, B., and Tedrake, R. "Performance of a High Specific Impulse Hall Thruster," *27th International Electric Propulsion Conference*. IEPC-01-35, Pasadena, CA, 2001.
- [26] Jacobson, D. T., and Jankovsky, R. S. "Performance Evaluation of a 50 kW Hall Thruster," *37th AIAA Aerospace Sciences Meeting and Exhibit*. AIAA-1999-0457, Reno, NV, 1999.
- [27] Fisch, N. J., and Raitses, Y. "Design and Operation of a Hall Thruster with Segmented Electrodes," *35th AIAA Joint Propulsion Conference*. AIAA 99-2572, Los Angeles, CA, 1999.
- [28] Raitses, Y., Dorf, L. A., Litvak, A. A., and Fisch, N. J. "Plume Reduction in Segmented Electrode Hall Thruster," *Journal of Applied Physics* Vol. 88, No. 3, 2000, pp. 1263-1270.
- [29] Kieckhafer, A. W. "The Effect of Segmented Anodes on the Performance and Plume of a Hall Thruster," *Mechanical Engineering*. Ph.D. Dissertation, Michigan Technological University, Houghton, MI, 2007.

- [30] Manzella, D. H., Jankovsky, R. S., and Hofer, R. R. "Laboratory Model 50 kW Hall Thruster," *38th AIAA Joint Propulsion Conference*. AIAA-2002-3676, Indianapolis, IN, 2002.
- [31] Sommer, A. *McGraw-Hill Encyclopedia of Physics*. New York: McGraw-Hill, 1983.
- [32] Choueiri, E. Y. "Fundamental Difference Between the Two Hall Thruster Variants," *Physics of Plasmas* Vol. 8, No. 11, 2001, pp. 5025-5034. doi: 10.1063-1.1409344
- [33] Goebel, D. M., and Katz, I. *Fundamentals of Electric Propulsion: Ion and Hall Thrusters*. Pasadena: Jet Propulsion Laboratory, 2008.
- [34] Gascon, N., Dudeck, M., and Barral, S. "Wall Material Effects in Stationary Plasma Thrusters: 1. Parametric Studies of an SPT-100," *Physics of Plasmas* Vol. 10, 2003, pp. 4123-4136.
- [35] Fife, J. M., Martinez-Sanchez, M., and Szabo, J. "A Numerical Study of Low-Frequency Discharge Oscillations in Hall Thrusters," *33rd Joint Propulsion Conference*. AIAA 97-3052, Seattle, WA, 1997.
- [36] J.P., B., and Koppel, C. "Development of a Second Generation of SPT," *24th International Electric Propulsion Conference*. IPEC 95-035, Moscow, Russian, 1995.
- [37] Stephan, K., and Mark, T. D. "Absolute Partial Electron Impact Ionization Cross Sections of Xe from Threshold up to 180 eV," *Journal of Chemical Physics* Vol. 81, No. 7, 1984, pp. 3116-3117.
- [38] Raitsev, Y., Kaganovich, I. D., Khrabrov, A., Sydorenko, D., Fisch, N. J., and Smolyakov, A. "Effect of Secondary Electron Emission on Electron Cross-Field Current in ExB Discharges," *IEEE Transactions of Plasma Science* Vol. 39, No. 4, 2011, pp. 995-1006.
- [39] Raitsev, Y., and Fisch, N. J. "Parametric Investigations of a Nonconventional Hall Thruster," *Physics of Plasmas* Vol. 8, No. 5, 2001, pp. 2579-2586. doi: 10.1063/1.1355318
- [40] Smirnov, A., and Raitsev, Y. "Plasma Measurements in a 100 W Cylindrical Hall Thruster," *Journal of Applied Physics* Vol. 95, No. 5, 2004, pp. 2283-2292.
- [41] Kramer, J. "Pulsed-Laser Optogalvanic spectroscopy in a High-Pressure Hg Discharge," *Journal of Applied Physics* Vol. 64, No. 4, 1988, pp. 1758-1766.
- [42] Kramer, J. "Laser Spectroscopy of Ground-State Scandium Ions in a High-Pressure Metal Halide Discharge II. Optogalvanic Spectroscopy," *Journal of Applied Physics* Vol. 70, No. 2, 1991, pp. 636-641.
- [43] Courtney, D. G., Lozano, P., and Martinez-Sanchez, M. "Continued Investigation of Diverging Cusped Field Thruster," *44th AIAA Joint Propulsion Conference*. AIAA 2008-4631, Hartford, CT, 2008.
- [44] Morozov, A. I., Esipchuk, Y. V., Tilinin, G. N., Trofimov, A. V., Sharov, Y. A., and Shchepkin, G. Y. "Plasma Accelerator With Closed Electron Drift and Extended Acceleration Zone," *Soviet Physics Journal* Vol. 17, No. 1, 1972, pp. 38-45.
- [45] Morozov, A. I., Esipchuk, Y. V., Kapulkin, A. M., Nevrovskii, V. A., and Smirnov, V. A. "Effect of The Magnetic Field on a Closed-Electron-Drift Accelerator," *Soviet Physics Journal* Vol. 17, No. 3, 1972, pp. 482-487.

- [46] Kim, V., Grdlichko, D., Kozlov, V., Lazourenko, A., Popov, G., and Shkrylnikov, A. "Local Plasma Parameter Measurements by Nearwall Probes Inside the SPT Accelerating Channel Under Thruster Operation With Kr," *38th AIAA Joint Propulsion Conference*. AIAA 2002-4108, Indianapolis, IN, 2002.
- [47] King, D. Q., De Grys, K., and Jankovsky, R. S. "Multi-mode Hall Thruster Development," *37th AIAA Joint Propulsion Conference*. AIAA 2001-3778, Salt Lake City, UT, 2001.
- [48] Garrigues, L., Boniface, C., Hagelaar, G. J. M., and Boeuf, J. P. "Performance Modeling of a Thrust Vectoring Device for Hall Effect Thrusters," *Journal of Propulsion and Power* Vol. 25, No. 5, 2009, pp. 1003-1012. doi: 10.2514/1.39680
- [49] Day, M., Kim, V., Kozlov, V., Lazourenko, A., Popov, G., and Skrylnikov, A. "Investigation of the Possibility to Reduce SPT Plume Divergence By Optimization of The Magnetic Field Topology in The Accelerating Channel," *25th International Electric Propulsion Conference*. IEPC-97-154, Cleveland, OH, 1997.
- [50] Haas, J. M., and Gallimore, A. "Characterization of the Internal Plasma Structure of a 5 kW Hall Thruster," *26th International Electric Propulsion Conference*. IEPC-99-78, Kitakyushu, Japan, 1999.
- [51] Reid, B. M. "The Influence of Neutral Flow Rate in the Operation of Hall Thrusters," *Aerospace Engineering*. Ph.D., University of Michigan, 2009.
- [52] Raitses, Y., Staack, D., Dorf, L. A., and Fisch, N. J. "Experimental Study of Acceleration Region in a 2kW Hall Thruster," *39th AIAA Joint Propulsion Conference*. AIAA 2003-5153, Huntsville, AL, 2003.
- [53] McVey, J. B., Britt, E. J., Engelman, S. F., Gulczinski, F. S., Beiting, E. J., and Pollard, J. E. "Characteristics of the T-220HT Hall-Effect Thruster," *39th Joint Propulsion Conference*. AIAA 2003-5158, Huntsville, AL, 2003.
- [54] Xu, K. G., and Walker, M. L. R. "High-Power, Null-Type, Inverted Pendulum Thrust Stand," *Review of Scientific Instruments* Vol. 80, 2009. doi: 10.1063/1.3125626
- [55] Curry, J. J., Sakai, M., and Lawler, J. E. "Measurement of the Hg Distribution in a High-Pressure Arc Lamp by X-ray Absorption," *Journal of Applied Physics* Vol. 84, No. 6, 1998.
- [56] Olsen, J., and Moskowitz, W. P. "Detrimental Effect of a Small Amount of Ripple in a Metal Halide System," *IEEE Industrial Applications Conference*. 2005.
- [57] Schafer, R., and stormber, H.-P. "Investigations on the Fundamental Longitudinal Acoustic Resonance of High Pressure Discharge Lamps," *Journal of Applied Physics* Vol. 53, No. 5, 1982. doi: 10.1063/1.331167
- [58] Kramer, J. "Saturated Laser-Induced Fluorescence in a High-Pressure Metal Halide Discharge," *Journal of Applied Physics* Vol. 87, No. 5, 1990, pp. 2289-2297.
- [59] Shastry, R. "Experimental Characterization of the Near-Wall Region in Hall Thrusters and its Implications on Performance and Lifetime," *Aerospace Engineering*. Ph.D., University of Michigan, 2011.
- [60] Hagstrum, H. D. "Auger Ejection of Electrons From Tungsten by Noble Gas Ions," *Physical Review* Vol. 96, No. 2, 1954, pp. 325-335.

- [61] Brown, D. L., and Gallimore, A. "Evaluation of Ion Collection Area in Faraday Probes," *Review of Scientific Instruments* Vol. 81, No. 063504, 2010. doi: 10.1063/1.3449541
- [62] Brown, D. L., and Gallimore, A. D. "Evaluation of Facility Effects on Ion Migration in a Hall Thruster Plume," *Journal of Propulsion and Power* Vol. 27, No. 3, 2011, pp. 573-585. doi: 10.2514/1.B34068
- [63] Azziz, Y., and Martinez-Sanchez, M. "Determination of In-Orbit Plume Characteristics from Laboratory Measurements," *42nd AIAA Joint Propulsion Conference*. AIAA 2006-4484, Sacramento, CA, 2006.
- [64] Curry, J. J., Sansonetti, C. J., and Wang, J. "Temperature Profiles and Thermal Losses in 150 W High-Intensity Discharge Lamps," *Journal of Physics D, Applied Physics* Vol. 38, No. 17, 2005.
- [65] Curry, J. J., and Lafitte, B. "X-Ray Absorption Imaging of High-Intensity Discharge Lamps Using an X-Ray Tube Source," *IEEE Transactions on Plasma Science* Vol. 36, No. 1, 2008. doi: 10.1109/TPS.2007.911464
- [66] Gulczinski, F. S., and Gallimore, A. D. "Near-Field Ion Energy and Species Measurements of a 5-kW Hall Thruster," *Journal of Propulsion and Power* Vol. 17, No. 2, 2001, pp. 418-427.
- [67] Linnell, J. A., and Gallimore, A. D. "Internal Plasma Structure Measurements of a Hall Thruster Using Plasma Lens Focusing," *41st AIAA Joint Propulsion Conference*. AIAA 2005-4402, Tucson, AZ, 2005.
- [68] Kemp, R. F., and Sellen, J. M. J. "Plasma Potential Measurements by Electron Emissive Probes," *Review of Scientific Instruments* Vol. 37, No. 4, 1966, p. 455.
- [69] Chen, F. F. "Electric Probes," *Plasma Diagnostic Techniques*. Academic Press New York, 1965.
- [70] Hershkowitz, N., and Cho, M. "Measurement of Plasma Potential Using Collecting and Emitting Probes," *Journal of Vacuum Science & Technology* Vol. 6, No. 3, 1988.
- [71] Belikov, M. B., Gorshkov, O. A., Rizakhanov, R. N., and Shagayda, A. A. "Hall-Type Low-and-Mean-Power Thrusters Output Parameters," *35th Joint Propulsion Conference*. AIAA 99-2571, Los Angeles, CA, 1999.
- [72] Zhurin, V. V., Kaufman, H. R., and Robinson, R. S. "Physics of Closed Drift Thrusters," *Plasma Sources Science and Technology* Vol. 8, No. 1, 1999, pp. R1-R20.
- [73] Linnell, J. A. "An Evaluation of Krypton Propellant in Hall Thrusters," *Aerospace Engineering*. Ph.D., University of Michigan, 2007.
- [74] Hofer, R. R., Mikellides, I. G., Katz, I., and Goebel, D. M. "Wall Sheath and Electron Mobility Modeling in Hybrid-PIC Hall Thruster Simulations," *43rd AIAA Joint Propulsion Conference*. AIAA-2007-5267, Cincinnati, OH, 2007.
- [75] Allis, M. K., Gascon, N., Vialard-Goudou, C., and Cappelli, M. A. "A Comparison of s-D Hybrid Hall Thruster Model to Experimental Measurements," *40th AIAA Joint Propulsion Conference*. AIAA-2004-3951, Fort Lauderdale, FL, 2004.
- [76] Huang, W., and Gallimore, A. "Neutral Flow Evolution in a Six-Kilowatt Hall Thruster," *Journal of Propulsion and Power* Vol. 27, No. 3, 2011, pp. 553-563.

- [77] Mitchner, M., and Kruger, C. H. J. *Partially Ionized Gases*: John Wiley & Sons Inc, 1973.
- [78] Anders, A., Anders, S., and Brown, I. G. "Effect of Duct Bias on Transport of Vacuum Arc Plasmas Through Curved Magnetic Filters," *Journal of Applied Physics* Vol. 75, No. 10, 1994, pp. 4900-4905.
- [79] Keidar, M., and Beilis, I. I. "Plasma-Wall Sheath in a Positive Biased Duct of the Vacuum Arc Magnetic Macroparticle Filter," *Applied Physics Letters* Vol. 73, No. 3, 1998, pp. 306-308.
- [80] Brown, D. L., Larson, W., and Beal, B. E. "Methodology and Historical Perspective of a Hall Thruster Efficiency Analysis," *Journal of Propulsion and Power* Vol. 25, No. 6, 2009, pp. 1163-1177. doi: 10.2514/1.38092
- [81] Raitses, Y., Staack, D., and Fisch, N. J. "Plasma Characterization of Hall Thruster with Active and Passive Segmented Electrodes," *38th AIAA Joint Propulsion Conference*. AIAA 2002-3954, Indianapolis, IN, 2002.
- [82] Barral, S., Zurbach, S., and Dudeck, M. "Experimental Investigation of a Layered Graphite/BN Channel for Hall Thruster," *32nd International Electric Propulsion Conference*. IEPC-2011-192, Wiesbaden, Germany, 2011.
- [83] Book, C. F., and Walker, M. L. R. "Effect of Anode Temperature on Hall Thruster Performance," *Journal of Propulsion and Power* Vol. 26, No. 5, 2010, pp. 1036-1044. doi: 10.2514/1.48028
- [84] Massey, D., Kieckhafer, A. W., Sommerville, J., and King, L. B. "Development of a Vaporizing Liquid Bismuth Anode for Hall Thrusters," *40th AIAA Joint Propulsion Conference*. AIAA 2004-3768, Fort Lauderdale, FL, 2004.
- [85] Dorf, L., Raitses, Y., and Fisch, N. J. "Experimental Studies of Anode Sheath Phenomena in a Hall Thruster Discharge," *Journal of Applied Physics* Vol. 97, 2005.
- [86] Anders, A., and Anders, S. "The Working Principle of the Hollow-Anode Plasma Source," *Plasma Sources Science and Technology* Vol. 4, 1995, pp. 571-575.